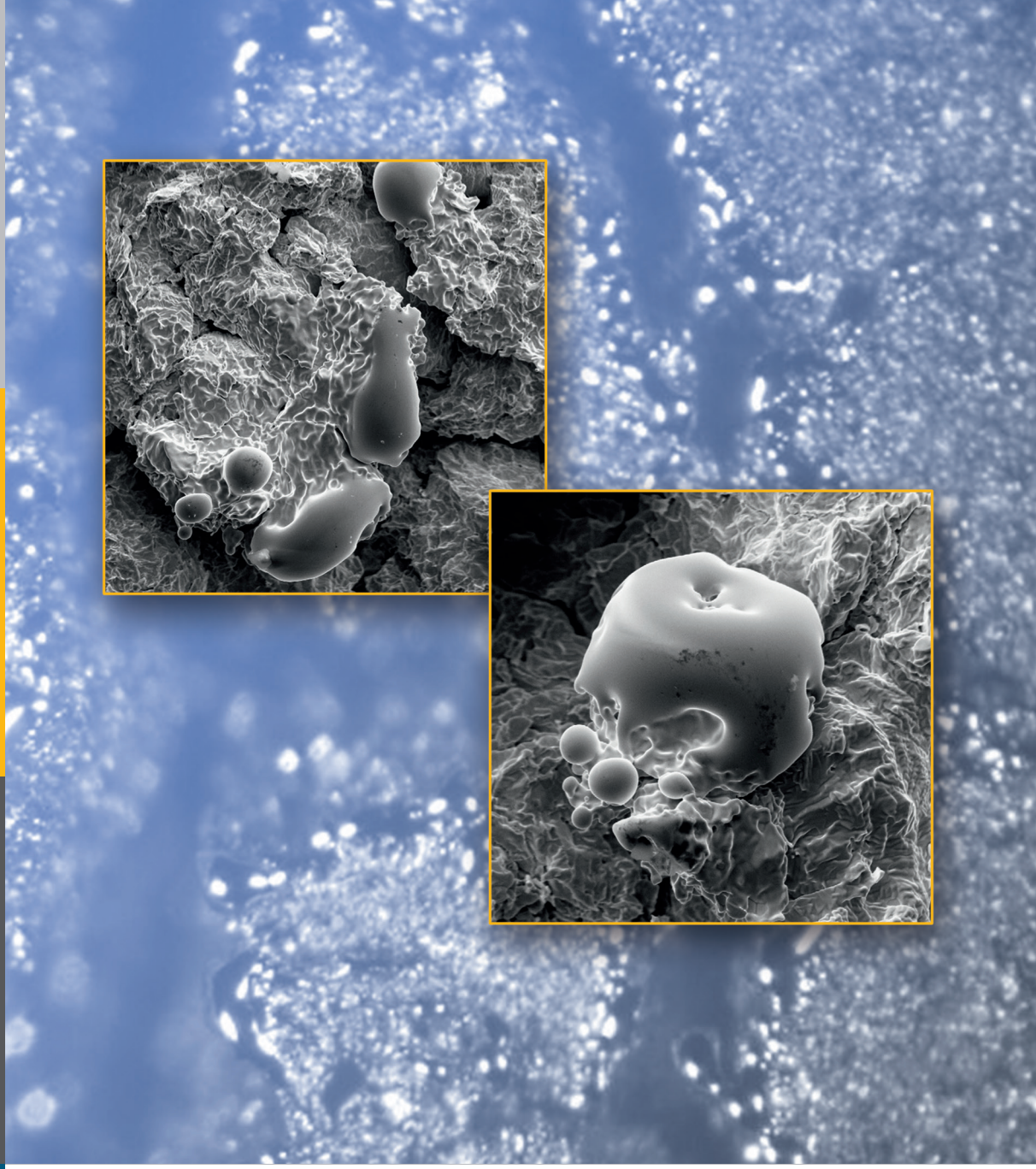

Combined Steady State and High Cycle Transient Heat Load Simulation with the Electron Beam Facility JUDITH 2

Thorsten Werner Loewenhoff

JÜLICH
FORSCHUNGSZENTRUM

Member of the Helmholtz Association

Schriften des Forschungszentrums Jülich
Reihe Energie & Umwelt / Energy & Environment Band / Volume 173

Forschungszentrum Jülich GmbH
Institute of Energy and Climate Research (IEK)
Microstructure and Properties of Materials (IEK-2)

Combined Steady State and High Cycle Transient Heat Load Simulation with the Electron Beam Facility JUDITH 2

Thorsten Werner Loewenhoff

Schriften des Forschungszentrums Jülich
Reihe Energie & Umwelt / Energy & Environment Band / Volume 173

ISSN 1866-1793 ISBN 978-3-89336-869-3

Bibliographic information published by the Deutsche Nationalbibliothek.
The Deutsche Nationalbibliothek lists this publication in the Deutsche Nationalbibliografie; detailed bibliographic data are available in the Internet at http://dnb.d-nb.de.

Publisher and Distributor: Forschungszentrum Jülich GmbH
Zentralbibliothek
52425 Jülich
Tel: +49 2461 61-5368
Fax: +49 2461 61-6103
Email: zb-publikation@fz-juelich.de
www.fz-juelich.de/zb

Cover Design: Grafische Medien, Forschungszentrum Jülich GmbH

Printer: Grafische Medien, Forschungszentrum Jülich GmbH

Schriften des Forschungszentrums Jülich
Reihe Energie & Umwelt / Energy & Environment, Band / Volume 173

D 82 (Diss., RWTH Aachen University, 2012)

ISSN 1866-1793
ISBN 978-3-89336-869-3

The complete volume is freely available on the Internet on the Jülicher Open Access Server (JUWEL) at www.fz-juelich.de/zb/juwel

List of publications

Parts of the results presented in this work have already been published in the following articles:

Th. Loewenhoff, J. Linke, G. Pintsuk; Simulation of repeated short transient heat loads with the electron beam facility JUDITH 2; Jahrestagung Kerntechnik 2010 Compact No. 802 (2010)

Th. Loewenhoff, T. Hirai, S. Keusemann, J. Linke, G. Pintsuk, A. Schmidt; Experimental simulation of Edge Localised Modes using focused electron beams – features of a circular load pattern; *Journal of Nuclear Materials* 415 51 – 54 (2011);
doi: 10.1016/j.jnucmat.2010.08.065

J. Linke, Th. Loewenhoff, V. Massaut, G. Pintsuk, G. Ritz, M. Rödig, A. Schmidt, C. Thomser, I. Uytdenhouwen, V. Vasechko, M. Wirtz; Performance of different tungsten grades under transient thermal loads; *Nuclear Fusion* 51 073017 (2011);
doi: 10.1088/0029-5515/51/7/073017

Th. Loewenhoff, A. Bürger, J. Linke, G. Pintsuk, A. Schmidt, L. Singheiser, C. Thomser; Evolution of tungsten degradation under combined high cycle ELM and steady state heat loads; *Physica Scripta* T145 014057 (2011);
doi: 10.1088/0031-8949/2011/T145/014057

Th. Loewenhoff, J. Linke, G. Pintsuk, C. Thomser; Tungsten and CFC degradation under combined high cycle transient and steady state heat loads; *Fusion Engineering and Design* (2012);
doi: 10.1016/j.fusengdes.2012.02.106 (in press, corrected proof)

This work, supported by the European Communities under the contract of Association between EURATOM/Forschungszentrum Jülich GmbH, was carried out within the framework of the European Fusion Development Agreement. The views and opinions expressed herein do not necessarily reflect those of the European Commission.

List of symbols and abbreviations

Symbols

$\overline{W_{cr}}$	Average crack width	[m]
σ	Gaussian beam width	[m]
σ_{SB}	Stefan-Boltzmann constant ($5.670373 \cdot 10^{-8}$)	[$Wm^{-2}K^{-4}$]
ΔT	Temperature rise	[°C]
Δt	Pulse duration	[s]
$\epsilon_W/\epsilon_{CFC}$	Emissivity of tungsten/CFC	[-]
λ	Wavelength	[m]
λ_{max}	Peak wavelength (following from Wien's displacement law)	[m]
p	Fraction by which $L(r_p)$ is smaller than L_0	[-]
A	Area	[m^2]
d	Distance	[m]
f_x, f_y	Frequency in x/y direction	[Hz]
F_{HF}	Factor of heat flux	[$Wm^{-2}s^{0.5}$]
H(x,y)	Incident energy density	[Jm^{-2}]
H_0	Incident energy density in the beam centre H(0,0)	[Jm^{-2}]
H_{abs}(x,y)	Absorbed energy density	[Jm^{-2}]
L(x,y)	Incident power density	[Wm^{-2}]
L_0	Incident power density in the beam centre L(0,0)	[Wm^{-2}]
L_{abs}(x,y)	Absorbed power density	[Wm^{-2}]
P	Power	[W]

p_{av}	Average vacuum pressure (as defined in [1])	[bar]
$p_{chamber}$	Main chamber vacuum pressure	[bar]
R_a	Mean roughness of a surface as defined in2.2	[-]
R_C	Electron reflection coefficient (of carbon)	[-]
r_p	(Radial) distance from beam centre at which $L(r_p) = L_0 \cdot (1\text{-}p)$	[m]
R_W	Electron reflection coefficient (of tungsten)	[-]
t	Time	[s]
T_{peak}	Peak temperature (during a transient heat load)	[°C]
T_{surf}	Surface temperature	[°C]
U_a^{J1}/U_a^{J2}	Acceleration voltage in JUDITH 1/JUDITH 2	[V]

Abbreviations

BSE	Backscattered Electron (image)
CFC	Carbon Fibre Composite
CTE	Coefficient of Thermal Expansion
dpa	Displacement per atom
DW	Double forged (pure) tungsten
EBSD	Electron Backscatter Diffraction
ELM	Edge Localized Mode
FEM	Finite Element Method
FWHM	Full width at half maximum
IFMIF	International Fusion Materials Irradiation Facility
JET	Joint European Torus
JUDITH	Jülich Divertor Test Facility in Hot Cells
LM	Light microscope
LOI	Line of interest
PFC	Plasma facing component

PFM	Plasma facing material
POI	Point of interest
ROI	Region of interest
SE	Secondary Electron (image)
SEM	Scanning Electron Microscopy/Microscope
SSHL	Steady state heat load
THL	Transient heat load
VDE	Vertical Displacement Event

Kurzfassung

Der steigende Weltenergiebedarf führt zur Zeit zu großen Anstrengungen bei Forschung und Entwicklung mit dem Ziel neue Energieressourcen zu erschließen. Eine mögliche Option zur Energiegewinnung in Großkraftwerken ist die Nutzung der nuklearen Fusion, die Wärme produziert welche mit konventioneller Dampfturbinentechnologie in Strom umgewandelt werden kann. Die praktische Umsetzung stellt jedoch eine große wissenschaftliche und technologische Herausforderung dar. Die entstehenden Wärmeflüsse, die die innere Wand einer Fusionsanlage und besonders den am stärksten belasteten Teil, den Divertor, treffen, sind eines der Themen die zur Zeit erforscht werden. Dabei wird zwischen statischem Hitzefluss (steady state heat load, SSHL), der während des Betriebs kontinuierlich wirkt, und transienten Wärmelasten (transient heat loads, THL), die dem SSHL überlagerte kurzzeitige Ereignisse darstellen, unterschieden. Die potentiell gefährlichsten THL während des normalen Betriebs sind Typ I Edge Localised Modes (ELMs). Sie werden im zukünftigen Fusionsexperiment ITER voraussichtlich Leistungsdichten von 1 – 10 GWm^{-2} bei Pulsdauern von 0.2 – 0.5 ms erreichen. Aufgrund der hohen Wiederholrate werden mehr als 10^6 ELM–Ereignisse im Laufe der für die Divertorkomponenten vorgesehenen Lebensdauer erwartet. Es existieren jedoch nur Daten über das Verhalten von Materialien bei niedrigen Pulszahlen (typischerweise 100 – 1000).

Die vorliegende Arbeit beschreibt die Entwicklung eines Verfahrens zur Simulation hochfrequenter THL mit Hilfe einer Elektronenstrahlanlage und die an Wolfram und kohlenstoffbasierten Materialien (carbon fibre composite, CFC) durchgeführten Experimente. Das Verfahren arbeitet mit einer Wiederholrate von 25 Hz, daher mussten aktiv gekühlte Komponenten entworfen und verwendet werden. Eine neue Art der Strahlführung, kreisförmige Belastungsmethode genannt, war ebenfalls ein Ergebnis des Entwicklungsprozesses. Sie wurde für alle nachfolgenden Tests benutzt, da Schwankungen von Parametern (z. B. der Kammerdruck) bei diesem Verfahren nur einen geringen Einfluss auf die aufgebrachte Leistungsdichte haben. Die Elektronenstrahlführung ist außerdem flexibel genug um zusätzlich zur THL eine SSHL zwischen zwei aufeinander folgenden THL aufzubringen. Das ermöglicht es die Grundtemperatur der Probenoberfläche zu beeinflussen.

Die Materialtests wurden mit Pulszahlen von 10^2 – 10^6 und absorbierten Leistungsdichten von bis zu 0.55 GWm^{-2} auf Wolfram beziehungsweise 0.68 GWm^{-2} auf CFC durchgeführt. Die Oberflächengrundtemperatur wurde mit Hilfe der Finite-

Element-Methode zuvor berechnet und während der Versuche mit Pyrometern überprüft. Die Schädigungsgrenze von Wolfram liegt unter 0.27 GWm^{-2}, die von CFC unter 0.68 GWm^{-2}. Bei geringeren Leistungsdichten ließen sich keinerlei Schädigungen bei bis zu 10^6 (Wolfram) bzw. 10^5 (CFC) Pulsen feststellen. Im Gegensatz zu CFC kommt es bei Wolfram zu einer langfristigen Materialermüdung. Die Materialdegradation trat bei höherer Temperatur früher auf, obwohl ursprünglich erwartet wurde, dass Wolfram bei höheren Temperaturen aufgrund der höheren Duktilität widerstandsfähiger sei. Die naheliegende Erklärung hierfür ist, dass erhöhte Duktilität zu stärkerer Schädigung in Folge von Materialermüdung führt.

Abstract

The increasing world energy needs lead to strong efforts in today's energy R&D trying to open up new energy resources. One possible option to access energy in large scale power plants is to use the process of nuclear fusion to generate heat and, from that, electricity with conventional steam turbine technology. However, the realisation is technologically and scientifically very challenging. The heat fluxes that load the inner walls of a fusion device, especially the most severely loaded part, the divertor, are one of the issues currently being under investigation. A distinction is made between steady state heat loads (SSHLs) that are continuously active during operation and transient heat loads (THLs) that are superimposed short-time events. The potentially most harmful THLs during normal operation are type I Edge Localised Modes (ELMs). They are estimated to have a power density of 1 – 10 GWm^{-2} for 0.2 – 0.5 ms duration in the upcoming next step fusion experiment ITER. Because of high pulse repetition frequency more than 10^6 ELM events are expected during the foreseen lifetime of divertor components. However, only data regarding behaviour of materials for a low number of pulses (typically 100 – 1000) exists.

This work describes the development of a procedure to simulate THLs at high repetition frequency using an electron beam facility and the tests done on tungsten and carbon-based (carbon fibre composite, CFC) plasma facing materials. The developed procedure uses a pulse frequency of 25 Hz, hence actively cooled components are necessary and were designed. A novel electron beam guidance procedure, called circular loading method, was a result of the developmental process. It was used for all later tests because it provides a stabilisation of the applied power density against test parameter fluctuations (e.g. vacuum quality). The electron beam guidance is flexible enough to provide a SSHL pattern during the interpulse time (between two successive THLs) additionally to the THL pulses. This allowed to influence the base temperature of the sample surface.

The material tests were done with pulse numbers of 10^2 – 10^6 and absorbed power densities of up to 0.55 GWm^{-2} and 0.68 GWm^{-2} per pulse for tungsten and CFC materials respectively. The surface base temperature was predicted by finite element analyses and monitored by pyrometer measurements. Damage thresholds of the investigated tungsten and CFC were found to be < 0.27 GWm^{-2} and < 0.68 GWm^{-2} respectively. Below these power densities no damage/degradation was found for

pulse numbers up to 10^6 (tungsten) or 10^5 (CFC). Tungsten showed long term fatigue, which did not occur in CFC. Although it was expected that tungsten would be more resistant at higher base temperatures due to higher ductility, it was found to show earlier degradation at higher temperatures. It is proposed that an increased ductility leads to stronger fatigue damage.

Contents

1 Introduction

1.1 Nuclear fusion

The physical process of nuclear fusion describes the coalescence of at least two atomic nuclei to form a single heavier nucleus. It is accompanied by the release or absorption of energy, depending on the binding energy per nucleon before and after fusion. Nuclei of lower mass than ^{62}Ni release energy in fusion whereas heavier nuclei absorb energy, since ^{62}Ni has the highest binding energy per nucleon of all elements (fig. 1.1) [2]. A high kinetic energy is necessary to overcome the Coulomb repulsion

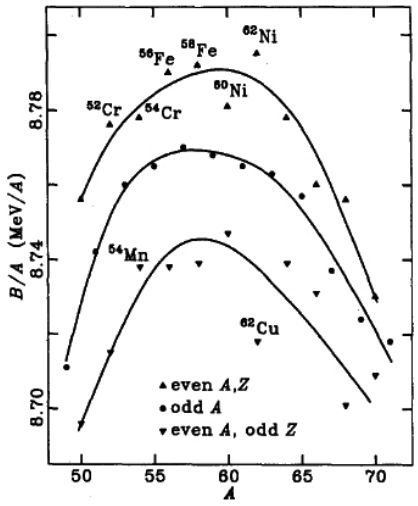

Figure 1.1: Average binding energy per nucleon against mass number of the strongest bound nucleons [2].

of the positively charged nuclei. This force dominates at long distances, whereas the attractive short ranged nuclear force dominates at distances of a few nucleon radii. Although the effect of quantum tunnelling facilitates the reaction, an average kinetic energy of the order of 10 keV is necessary to enable fusion reactions in a deuterium–tritium plasma. The deuterium–tritium fusion reaction (D–T reaction) shows the

lowest necessary temperature/average kinetic energy for starting fusion reactions (fig. 1.2). It generates a helium nucleus, a free neutron and releases 17.6 MeV

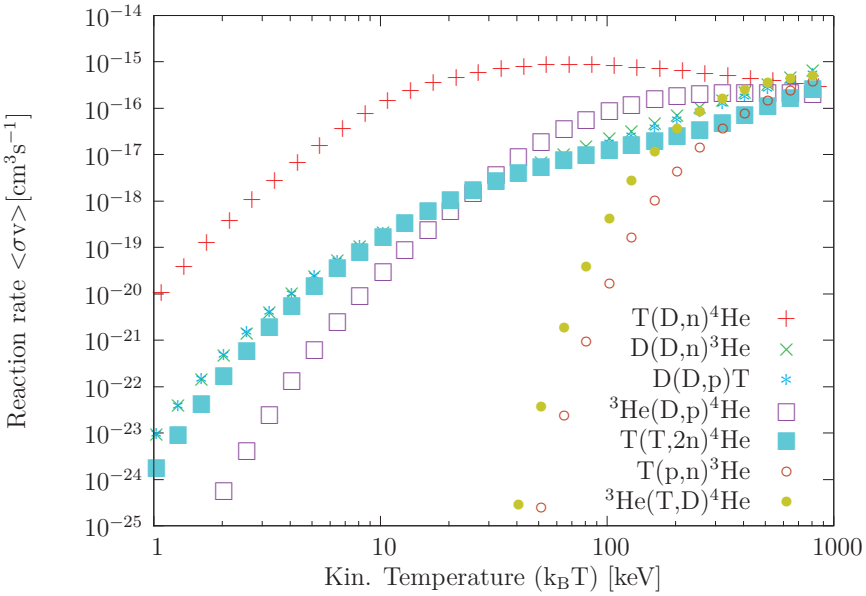

Figure 1.2: Fusion reaction rates for several light nuclei against average kinetic particle energy. The deuterium-tritium reaction has the highest reaction rate up to a few hundred keV. The plotted data were generated by the analytic expressions provided by [3].

binding energy, distributed among the end products of the reaction according to the mass ratio (fig. 1.3):

$$\mathrm{D} + \mathrm{T} \rightarrow {}^4\mathrm{He}\ (3.5\ \mathrm{MeV}) + \mathrm{n}\ (14.1\ \mathrm{MeV}) \tag{1.1}$$

Some other possible reactions for controlled fusion are:

$$\mathrm{D} + \mathrm{D} \rightarrow {}^3\mathrm{He}\ (0.82\ \mathrm{MeV}) + \mathrm{n}\ (2.45\ \mathrm{MeV}) \tag{1.2}$$

$$\mathrm{D} + \mathrm{D} \rightarrow \mathrm{T}\ (1.01\ \mathrm{MeV}) + \mathrm{H}\ (3.02\ \mathrm{MeV}) \tag{1.3}$$

$$\mathrm{D} + {}^3\mathrm{He} \rightarrow {}^4\mathrm{He}\ (3.6\ \mathrm{MeV}) + \mathrm{H}\ (14.7\ \mathrm{MeV}) \tag{1.4}$$

The large amount of released energy per fusion reaction and the sun as a model in nature led to the idea of using controlled fusion for a power plant. D-T fusion is the preferred reaction for future first generation fusion reactors, because of the high energy yield and the relatively low temperature needed to get a reasonable reaction

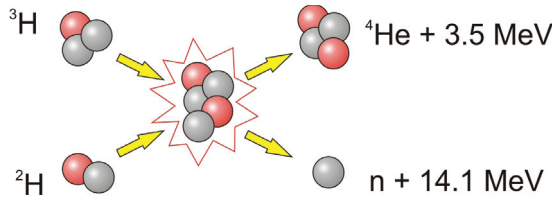

Figure 1.3: Deuterium-tritium fusion: Deuterium and tritium form an intermediate state ^{5}He with a decay width of 0.6 MeV (half life time $\approx 5.5 \cdot 10^{-22}$ s) [4]. It decays into a stable ^{4}He nucleus and a free neutron with kinetic energies of 3.5 MeV and 14.1 MeV respectively.

rate (fig. 1.2). Also deuterium can easily be extracted from sea water and tritium can be bred by bombarding a lithium blanket with neutrons from the D-T reaction itself:

$$^6\mathrm{Li} + \mathrm{n} \rightarrow {}^4\mathrm{He}\ (2.05\ \mathrm{MeV}) + \mathrm{T}\ (2.73\ \mathrm{MeV}) \tag{1.5}$$

$$^7\mathrm{Li} + \mathrm{n} \rightarrow {}^4\mathrm{He} + \mathrm{T} + \mathrm{n} - 2.47\ \mathrm{MeV} \tag{1.6}$$

Since several decades scientists are working on the realisation of controlled fusion. As it is necessary to heat up the fusion reactants to extremely high temperatures, all electrons are stripped off of the nuclei (for light elements), forming a hot plasma. The problem arises how to prevent the plasma from touching any cold matter (e.g.

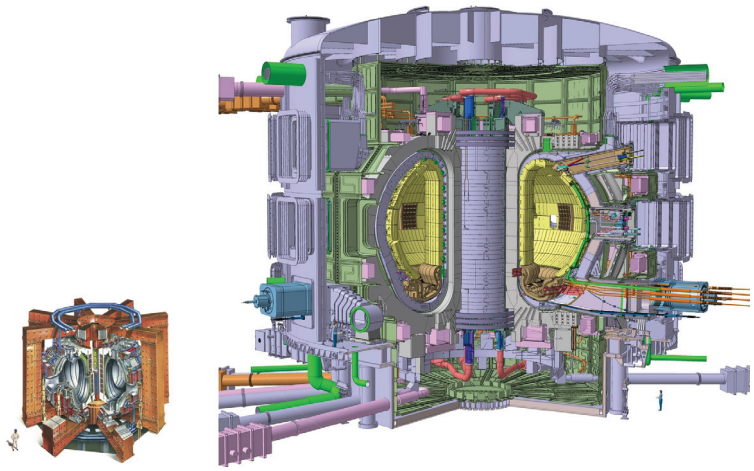

Figure 1.4: Tokamak devices JET (Joint European Torus, left) **and ITER** (Latin for "the way"): JET was constructed between 1977 and 1983. It is the biggest tokamak device in the world up to now. The construction of ITER, a next generation tokamak, started January 2007. The first plasma is scheduled to be ignited in 2019 [5, 6].

the inner walls of a containment device), possibly damaging the wall and eventually loosing its kinetic energy. Possible solutions are magnetic or inertial confinement devices. At the moment magnetic confinement in so called tokamak devices is the most developed method. Tokamaks are devices of toroidal shape that produce a strong magnetic field via (superconducting) magnets, in which the plasma is heated, confined and compressed (fig. 1.4). The biggest fusion experiment up to now, JET (Joint European Torus), has already reached a peak fusion power of 16.1 MW in 1997 [7]. For detailed information on related topics like the comparison of fusion energy to other energy sources, world energy need, safety & economic aspects see [8].

The next step fusion device ITER, currently under construction in Cadarache, France, is an experiment built to prove the viability of fusion as an energy source and to collect experience, data and technologies for future fusion power plants. The machine shall achieve a fusion power of 500 MW at a heating power of $\leq$50 MW ($Q \geq 10$) and continuous discharges for at least 400 seconds [5, 6, 9, 10].

1.2 Plasma facing materials and components

As previously mentioned, magnetic field confinement prevents the hot plasma from touching the wall of the vacuum vessel. This confinement is not perfect, on the contrary, a certain particle loss is necessary to remove the helium (exhaust). This results in particle and energy fluxes loading the wall. Therefore special components protect the structural parts of the device, so called plasma facing components (PFC). These PFCs consist of an actively cooled heat sink, often made of copper based material and a plasma facing material (PFM) like beryllium (Be), carbon fibre composite (CFC) or tungsten (W) [11, 12]. Figure 1.5 shows the vacuum vessel of ITER with the first wall that faces the hot plasma and the divertor, a special part of the wall that has to withstand the highest heat and particle fluxes. PFMs have to meet several requirements:

High thermal conductivity and high melting/sublimation point
In order to absorb the incoming heat flux an outstanding thermal conductivity is often considered as most important. It should also not decrease much with temperature. Additionally a high melting/sublimation point helps to prevent melting due to local overheating and early evaporation at high temperatures due to low vapour pressure. Be, CFC and W have thermal conductivities of around 190 $Wm^{-1}K^{-1}$, < 500 $Wm^{-1}K^{-1}$ and 170 $Wm^{-1}K^{-1}$ at RT and melting/sublimation points of 1560 K, 3000 – 4500 K and 3700 K, respectively [13–17].

Plasma compatibility
Atoms of the PFM contaminate the plasma and can lead to poor plasma performance. Especially atoms with a high atomic number (Z), which are not completely ionised, convert kinetic energy of fuel nuclei into radiation (by electron excitation and

deexcitation) which escapes the magnetic confinement. This is an effective plasma cooling mechanism and can even lead to a complete termination of the plasma pulse. Thus maximum allowed concentration limits must be observed. The use of high-Z materials like tungsten requires more care and plasma control to ensure a low core concentration of atoms of PFMs (e.g. $<$ few 10^{-5} for tungsten). High-Z wall materials also limit the operational space compared to low-Z materials [17–19].

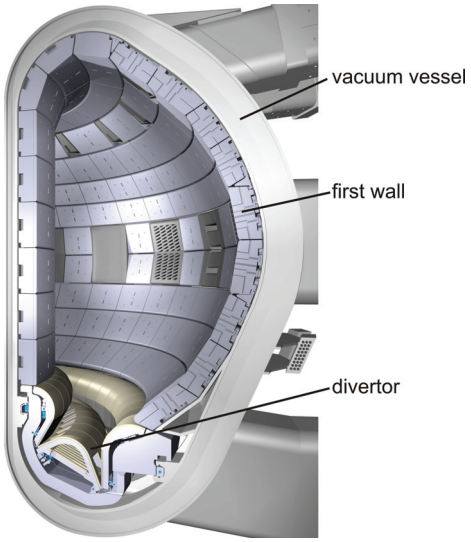

Figure 1.5: ITER vacuum vessel cross section: Beryllium is planned as PFM for the first wall, while CFC and tungsten will be used for the first configuration of the divertor. In later stages of operation a full tungsten divertor will be used [5]. Most recently the idea came up to directly start with a full tungsten divertor in order to save the costs for the second one. However, this divertor would have to sustain twice as long as planned before.

Sputtering resistance

High resistance against physical and chemical sputtering is of importance to lower the erosion rate of a PFM [20]. The aforementioned plasma contamination is also influenced by the thresholds and yields of these processes. Chemical sputtering can lead to the formation of undesirable phases and has influence on the Tritium inventory in the machine.

Neutron irradiation resistance

Volumetric neutron irradiation is a serious problem for future plasma facing and structural materials because the properties of the materials are often drastically changed by the irradiation. The thermal conductivity of CFC is a good example:

as shown in [15] it is reduced by a factor of up to 5 for a neutron damage of 0.2 dpa (1 dpa[1]/0.6 dpa is the expected dose for the ITER first wall/divertor [21], > 150 dpa for future commercial reactors [22]). Further investigations of material behaviour under application relevant neutron irradiation conditions are necessary to evaluate the property changes and other effects like swelling and embrittlement. An overview of the existing database is given in [23].

Neutron activation/transmutation resistance
Activation by neutrons is an important concern with respect to radioactive waste generation and change of material properties due to transmutation and possible subsequent formation of phases in the PFM. Materials in a fusion device or reactor that are exposed to neutron irradiation have to be carefully chosen in order to avoid long term radioactive waste [24].

Tritium uptake
The uptake of tritium is a criterion mainly because of the limitation of radioactive inventory of the machine. More tritium retained in the walls means less tritium that is available for the fusion reaction. At the moment a maximum of 700 g of tritium is the designated (administrative) limit for the ITER machine [25, 26].

Additionally PFMs have to operate at a broad temperature range from coolant inlet temperature up to 2000 or even 3000 K during transients. No known material meets all these requirements at a time, but the above mentioned materials meet most of them. Table 1.1 shows their advantages and disadvantages.

[1] 1 dpa $\hat{\approx}10^{25}$ neutrons/m^2 for low Z materials

Table 1.1: Advantages and disadvantages of most common PFM candidates: Beryllium is only suitable for the first wall and will be used in ITER. Tungsten and (maybe) CFC will be used in the ITER divertor. At the moment beryllium and tungsten PFCs are tested within the framework of the ITER like wall project in the JET experiment [27, 28].

Material	Advantages	Disadvantages
W	+ high thermal conductivity ≈ 170 $Wm^{-1}K^{-1}$ + thermal conductivity hardly influenced by temperature and neutron irradiation + extremely high melting point (≈ 3700 K) + low erosion (sputtering) rate + good thermal shock resistance + low tritium inventory	– high Z $\Rightarrow$ plasma contamination already at low concentration – rather poor mechanical properties $\Rightarrow$ poor workability – brittleness increases further by neutron irradiation – recrystallisation at high temperatures $\Rightarrow$ decrease of mechanical strength
CFC	+ excellent thermal conductivity (up to ≈ 500 $Wm^{-1}K^{-1}$ at RT) + no melting point at all (sublimation starts at ≈ 3800 K) + high thermal shock resistance + low Z $\Rightarrow$ high concentration allowed in the plasma	– thermal conductivity decreases significantly with temperature and neutron irradiation – high erosion rate – high tritium inventory, formation of hydrocarbons
Be	+ high thermal conductivity ≈ 190 $Wm^{-1}K^{-1}$ + low Z $\Rightarrow$ high concentration allowed in the plasma + oxygen getter $\Rightarrow$ improves vacuum conditions	– low melting point (1560 K) – thermal conductivity decreases with temperature – toxic (carcinogenic dust)

1.3 Steady state & transient (heat) loads

The first wall in ITER will face (apart from particle flux) a continuous heat flux in the order of 1 MWm^{-2} in normal (quasi-stationary) plasma operation mode, while the divertor will be exposed to power densities of approximately ≤ 10 MWm^{-2} (with occasional slow transients of ≤ 20 MWm^{-2} for ≤ 10 s). These steady state heat loads (SSHLs) may vary spatially and temporally and therefore result in surface temperatures that depend on time and the position of the PFCs. Additionally, the SSHL is superimposed by transient heat loads in the form of Edge Localised Modes (ELMs) during normal operation [9,29–33]. ELMs are classified into three types [34]:

Type I ELMs:
These events are short (0.2 – 0.5 ms) but intense outbursts that release 2 – 6 % of the plasma stored energy. They repeat with a frequency of several Hz and are also called "giant" ELMs. The repetition frequency increases with increasing plasma heating power. The power density of ELMs in ITER is estimated to be between several tenth up to several ten GWm^{-2} [30, 35–38].

Type II ELMs:
These ELMs are weaker than type I ELMs and have a higher frequency up to several thousand Hz. They are also called "grassy" ELMs [36].

Type III ELMs:
The outbursts are weak and frequent. As the repetition frequency decreases with increasing plasma heating power, these ELMs disappear at some point. They are also called "small" ELMs [36].

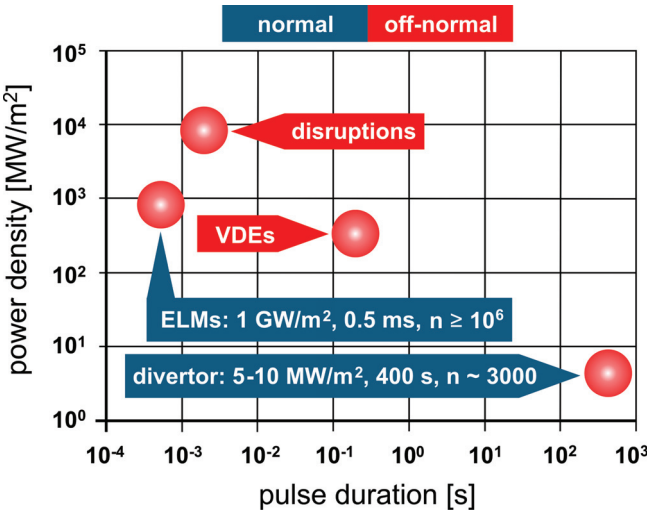

Figure 1.6: Thermal loads on the divertor expected in ITER [30, 31].

In the frame of this work type I ELMs are of interest because they pose the biggest danger for the PFMs. A frequency of several Hz for the occurrence of these ELMs was predicted for ITER. However mitigation techniques are necessary and topic of current research. They may lead to reduced intensity and increased frequency of several ten Hz or even a complete suppression of ELMs [12, 33, 39].

Apart from loads under normal operation conditions, a loss of plasma control can lead to disruptions and vertical displacement events (VDEs) or plasma contamination causes an early termination of the discharge (disruption). Both off-normal events are transients and deploy a large amount of energy on the wall/divertor PFMs. Tests already showed that they have to be avoided (preferably completely) as they are too severe for any material to withstand without degradation [11]. VDEs and disruptions are estimated to occur only in < 1 % and < 10 % of the ITER discharges, respectively [40].

Figure 1.6 depicts the different loads in a time vs. power density diagram. It is planned to replace the ITER divertor after 3000 discharges. Each discharge lasts for approximately 400 seconds, thus it has to withstand 3000 thermal fatigue cycles with at least 400 ELMs each. This results in $> 10^6$ ELMs during the lifetime of PFCs.

Table 1.2: Thermal loads expected for the ITER divertor/first wall [9, 17, 30–33, 40]

	Steady state	ELMs	VDEs	disruptions
Power density ($\mathrm{GWm^{-2}}$)	$(5 - 20) \cdot 10^{-3}$	1 – 10	0.2 – 0.6	> 10
Duration (s)	400	$(0.1 - 0.5) \cdot 10^{-3}$	0.1 – 0.3	$(0.1 - 5) \cdot 10^{-3}$
Energy density ($\mathrm{MJm^{-2}}$)	—	0.2 – 5	≈ 60	> 30
Frequency	continuous	$> 1 - 10$ Hz	< 1 %	< 10 %

1.4 Simulating thermal loads outside fusion devices

Several machines are used in order to investigate material behaviour under different irradiation conditions namely neutral or ion beam facilities, laser facilities, electron beam devices, infra-red heaters and arc discharge facilities. These machines differ in many aspects, like the kind of energy input, pulse duration and intensity, maximum irradiation area and penetration depth. The thermal loading scenarios can be divided into two categories:

Thermal shock tests
These tests simulate the impact of events like ELMs, VDEs and disruptions. They have high intensities (tenth to several GWm^{-2}, table 1.2) that have to be reached within a very short time period (sub-millisecond to tenth of a second). Simulation devices have to provide a high power density as well as a strong power rise and decrease. A heater can be used to preheat the samples in order to get results for different base temperatures. Depending on pulse frequency and since the effects of thermal shock tests are limited to the surface of the PFM, an active cooling system is not mandatory. If the influence of neutrons should be studied the machine must be located in a hot cell.

Thermal fatigue and screening tests
Fatigue tests investigate the behaviour of a complete PFC during thermal cycling under SSHL. This comprises the heat dissipation capability, the strength and thermal fatigue resistance of the joint between PFM and heat sink, possibly also before and after neutron irradiation. The required power densities are typically 3 magnitudes smaller (1 – 20 MWm^{-2}, table 1.2) than for thermal shock tests. The tested components and loaded areas can be very large, so high power machines are as well necessary, but the power density of the beam spot must not be high (or a fast beam scanning should be used) to avoid local overheating. Fast power rise and decrease, like for thermal shock tests, are not of great importance. A powerful cooling system is used to dissipate the generated heat. This system can be a standard low pressure water cooling circuit or it can be more sophisticated, providing high pressure, variable coolant temperature or using advanced cooling e.g. with helium.

Neutral or ion beam devices are able to provide particle fluxes and hence effects like physical and chemical sputtering/erosion and vapour shielding can be investigated. These machines need some time (seconds to minutes) to recover after a discharge (e.g. recharge capacitors). Electron beam or laser machines usually achieve higher power densities, have higher flexibility and higher repetition rates. They are therefore often used for thermal shock tests.

1.5 Thermally induced material damage

The interaction of plasma and neutrons with the PFMs leads to several effects, some of which were described in 1.2 and 1.3. The thermal loads can lead to roughening, swelling, cracking, erosion and melting/sublimation, depending on material, temperature, load intensity etc. Most of the effects are caused by thermally induced mechanical stress. In a fusion device degradation by heat loads mainly occurs in a surface layer and the joint. Test facilities (section 1.4) do not always deposit energy on the surface only, but have a penetration depth and hence the loading is partially volumetric. For electron beam facilities the beam penetration depth depends on the

electron energy which is determined by the acceleration voltage (U_e, see 2.1.1 and 2.1.2) and the material (mainly its density).

The thermal response of CFC and tungsten differs: Both materials crack, but CFC shows mainly erosion by brittle destruction [41] while tungsten starts to deform plastically to compensate high stresses. In the case of transient loads on tungsten the heated surface material is often surrounded by cooler (unloaded) material. This leads to compressive stress as the loaded material is expanding thermally, but is constrained by the rigid cool material. In case of exceeding the yield strength, irreversible plastic deformation of the hot region is the subsequent step, releasing part of the stress. After the transient event the material cools down and shrinks back, but the remaining deformation (strain) prevents it from returning back to the initial state, thus tensile stresses occur. When they exceed the tensile strength of the material cracking occurs, preferably at weak locations like grain boundaries. As cracks follow the grain boundaries it is possible that grains are eroded by an encompassing crack. Hence material degradation can be different for the same conditions depending on the microstructure of the material.

Depositing even higher intensity loads can lead to melting and melt layer formation. Melt droplets and layers are highly unwanted as they start to move (e.g. due to electromagnetic forces) and resolidify, thus transporting the armour material away from the most severely loaded areas or bridging castellations. A melt layer loss of 0.07 µm/pulse found in plasma gun experiments [42] with 0.5 ms pulses of 1.5 MJm^{-2} would result in 70 mm total loss after 10^6 ELM loads (about ten times the tile thickness). Splashes of molten tungsten may also contaminate the plasma and initiate plasma disruptions.

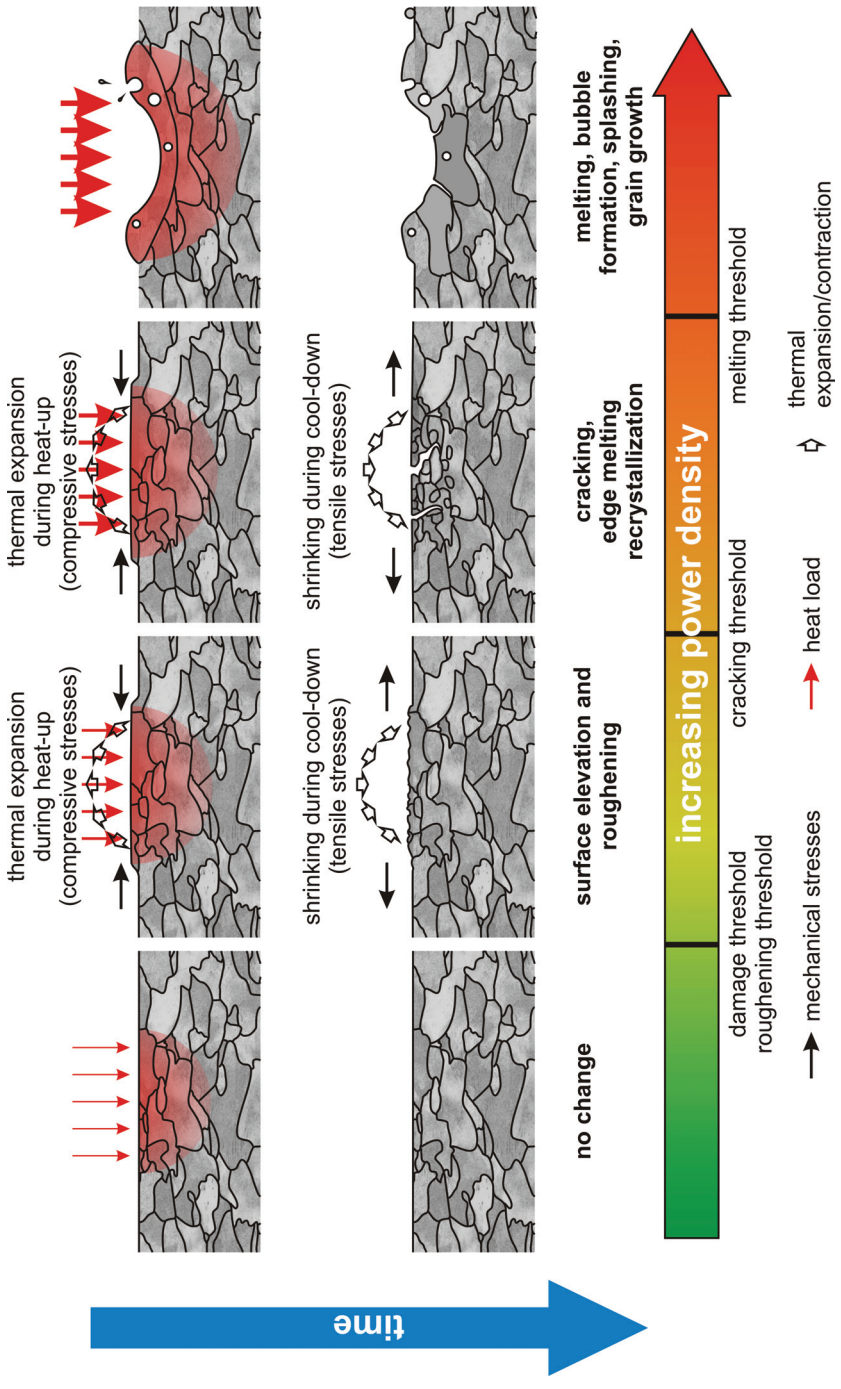

Figure 1.7: Tungsten damage depending on power density of THLs. Different thresholds are defined to characterise material performance.

1.6 Scope of work

In about ten years the international experimental fusion reactor ITER will go into operation. The divertor and the first wall of this machine will be subjected to transient and steady state heat loads. Investigations of different materials (especially beryllium, CFC and tungsten/tungsten alloys), their damage thresholds in general, cracking or melting thresholds in particular and the influence of geometry (castellation, shaping), plasma exposure (H, He, mixed), neutron irradiation, etc. on these thresholds are current research topics. It is necessary to know these limits and understand material behaviour in order to assess the lifetime of components, be aware of operational limits, find better PFMs and optimise the design of PFCs for ITER and future reactors.

Fatigue tests of components with steady state heat fluxes and cycle numbers of ITER relevant ranges are widely used for investigations and qualification tests. Although the PFCs are close to their limits, it seems technologically feasible to build a divertor that can withstand several thousand ITER discharges regarding the SSHL [43]. However, the impact of transient heat loads and 14 MeV neutron irradiation are two factors, which are much more difficult to investigate. In current research projects neutron irradiation is simulated by using neutrons from fission reactors, which do not provide the correct energy spectrum and only moderate fluxes. To face this problem the International Fusion Materials Irradiation Facility (IFMIF) is planned, which should be able to provide neutrons with a fusion relevant spectrum and a flux of about 10^{18} $m^{-2}s^{-1}$ [44].

Transient heat loads are investigated by the same or similar machines used for steady state tests. These test facilities have not yet proven the capability to apply transient loads with ITER relevant intensities and frequencies at the same time (not to mention simultaneous SSHL). Hence tests performed so far apply up to 1000 pulses, 10 000 at most in occasional experiments, but the divertor in ITER may be subjected to more than 10^6 transient events of ELM type. In contrast to other transients, which show a loss of control of the plasma or a plasma contamination, ELMs occur in normal operation mode. The impact of such a high number of transient loads is unknown. It is expected that the thresholds will be lower for such high pulse numbers compared to the known thresholds found for 100 – 1000 pulses. Recent research shows that transients of the ELM type can be mitigated and even completely suppressed [39, 45, 46]. However, as ITER will be an experimental facility it will not be operated in just one or few special (ELM free) configurations and ELMs will pose a threat to the PFCs.

Scope of this work was to make high pulse number tests accessible using the electron beam facility JUDITH 2 in Forschungszentrum Jülich (Germany). JUDITH 2 is characterised by a very flexible beam guidance system that was considered to be appropriate for the task. It allows not only the application of transient heat loads but also the simultaneous simulation of a steady state heat load. Hence, material

behaviour should be investigated at different surface base temperatures. The facility also provides the necessary power density (this was assumed because of earlier studies [1]), and an active cooling circuit that allows ITER-like cooling. First, calculations regarding the energy deposition by the electron beam should be made to develop a fundamental understanding of the load patterns when using the electron beam. The circular beam pattern, used in all later experiments, was an outcome of these calculations (section 3.4). The width of the beam depends on the operational mode and is essential for the achieved power density, therefore, a campaign was planned to measure the beam profile (section 3.5). In order to simulate a high number of transient events high frequencies are necessary. This required the development of actively cooled components (section 3.1). The component geometry should be integrated into a finite element model to predict surface temperatures (section 2.4) and the results should be compared to pyrometer measurements of the surface temperature development in order to ensure the correct application of the loads (section 2.2). First tests were planned as proof of principle (section 3.3). After obtaining a working test procedure, tests on tungsten and CFC can now be performed to explore damage thresholds and observe the development of material degradation with increasing cycle number (chapter 5). This degradation was investigated and quantified by different post mortem analysis methods (section 2.3).

2 Test facilities and methods

2.1 Electron beam test facilities

The electron beam machines JUDITH 1 (JUelich DIvertor Test facility in the Hot cells) and JUDITH 2 were used in this work and are described below. However two general aspects should be discussed before.

First, the penetration depth of the electrons (or the energy distribution depth, as considered here) depends on the acceleration voltage. For JUDITH 1 and JUDITH 2 the typical values are $U_a^{J1} = 120$ kV and $U_a^{J2} = 50$ kV, corresponding to penetration depths in tungsten of ≈ 7 µm and ≈ 5 µm, respectively. For CFC these values are higher: ≈ 90 µm and ≈ 25 µm respectively, because of the low density of carbon. When the electron beam reaches this depth more than 95 % of the absorbed beam energy has been deposited [47, 48].

Second, the electron beam is partially reflected (backscattered electrons) and therefore only a fraction of the beam energy is actually absorbed. This energy reflection strongly depends on the material. For tungsten and carbon values of $R_W = 0.45$ and $R_C = 0.03$ are used. These values were obtained by Monte-Carlo-simulation for the pure elements [49]. Literature values for tungsten vary between 0.38 and 0.5 [48, 50] and recent experiments in JUDITH 1 confirm the value of the Monte-Carlo-simulation [51].

2.1.1 JUDITH 1

JUDITH 1 is located in a hot cell and is licensed for tests of radioactive and toxic materials and components. It has a maximum power of 60 kW and an acceleration voltage of up to 150 kV (fig. 2.1). Because of better machine stability 120 kV are used, reducing the maximum power to 48 kW. The machine can simulate transient as well as steady state heat loads. For the latter active cooling can be performed with water at room temperature at a maximum flow rate of 60 l/min.

The beam diameter is small, with a FWHM of ≈ 1 mm [52]. A triangular signal is used to sweep the sample surface. The typical pulse duration for an ELM-like experiment (and at the same time minimum pulse duration) is 1 ms. The beam path is defined by the dimensions in x– and y–direction and the sweep frequencies f_x and f_y. Such a beam path is shown in figure 2.2 along with the resulting time dependent

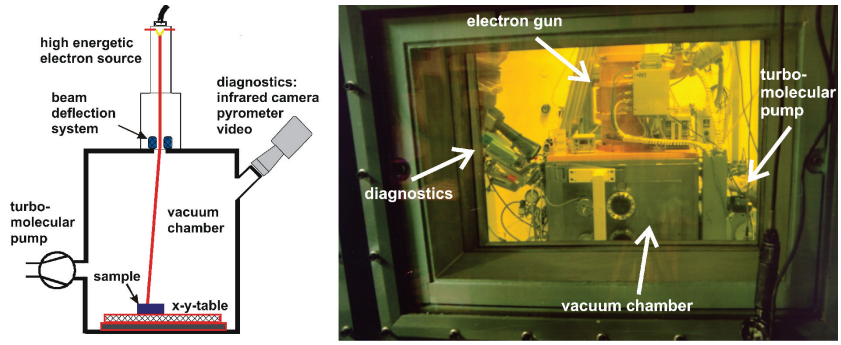

Figure 2.1: Schematic drawing and photo of the electron beam facility **JUDITH 1**. The photo shows the machine, located in a hot cell.

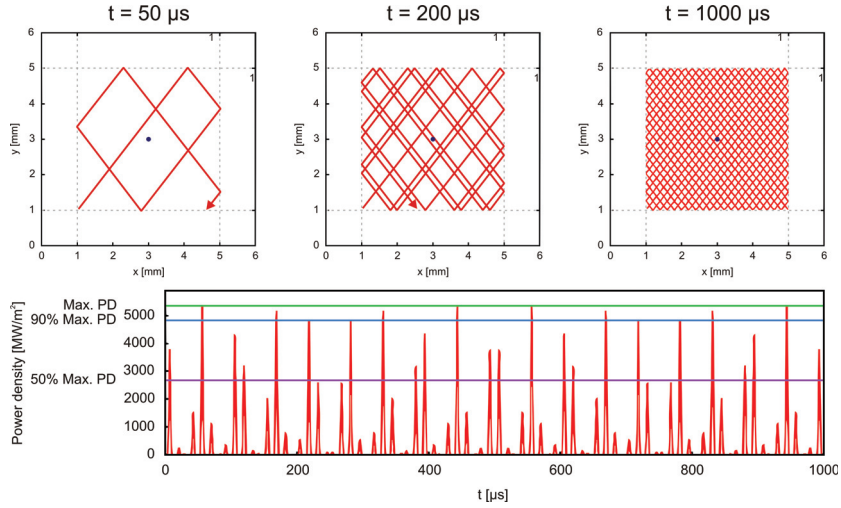

Figure 2.2: Electron beam path and applied power density for an experiment on a 4×4 mm^2 tungsten surface in JUDITH 1 (P = 11 kW, f_x = 31 kHz, f_y = 40 kHz, R_W = 0.45, Δt = 1 ms). Odd frequencies are chosen to achieve a homogeneous loading. The top pictures show the path after 50 µs, 200 µs and 1000 µs, the bottom picture shows the corresponding power density vs. time diagram for the blue spot in the centre of the loaded area. The average absorbed power density there is 0.38 GWm^{-2}.

power density for the centre of the loaded area. The test procedure relies on the fast scanning: Although the beam centre power density is $L_0 > 5$ GWm^{-2} (for the shown example of 11 kW power) the scan in figure 2.2 distributes the energy in the loaded area and creates an average absorbed power density of ≈ 0.38 GWm^{-2}. The example given was calculated for a tungsten surface ($R_W = 0.45$).

2.1.2 JUDITH 2

The electron beam facility JUDITH 2 consists of a cylindrical vacuum chamber (by "Trinos Vakuum-Systeme GmbH") with an EH800V electron beam gun (by "Von Ardenne Anlagentechnik GmbH") of 200 kW maximum power (fig. 2.3). The working acceleration voltage can be adjusted between 40–60 kV. Originally the machine was designed (and is used) for fatigue and screening tests of large components. It is equipped with a water cooling system that allows adjusting the water temperature between room temperature and 100 °C, with pressures up to 30 bar (3 MPa), flow rates of up to 200 l/min and a total cooling power of 150 kW [53]. The electron

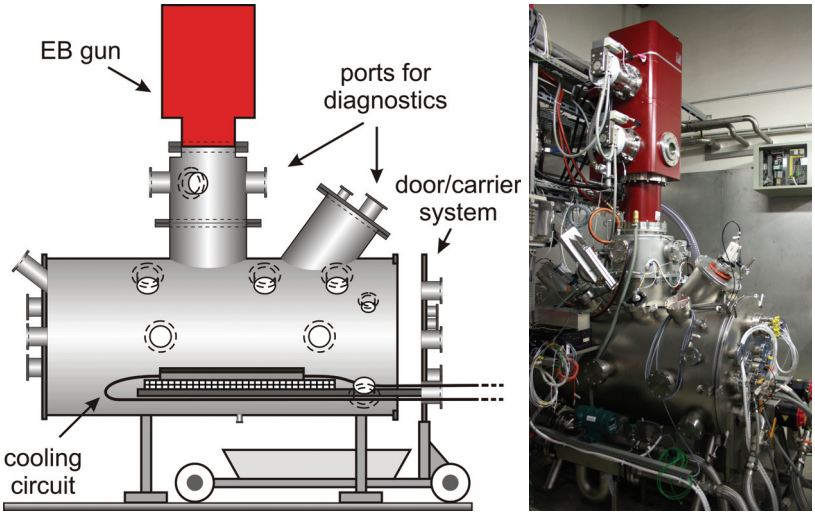

Figure 2.3: The electron beam facility JUDITH 2: Schematic view on the left, with opened door/specimen carrier system and picture of the machine on the right.

beam is guided via focussing magnetic lenses L_1 and L_2 and a deflecting lens [1] that are controlled by a program following x– and y–coordinates of a command file (standard ASCII file). The dwell time on a spot can be defined between 5 µs and 1 s. In contrast to JUDITH 1 the beam path can be chosen freely via the coordinates written into the command file. In order to simulate a steady state heat load a scanning path can be programmed that is used with a defocused beam to prevent local overheating. However, to simulate transient events special paths were developed in the course of this work. For this also the knowledge of the beam profile is crucial to determine the beam power density (sections 3.2 & 3.5).

JUDITH 2 is licensed for tests with toxic materials like beryllium (e.g. first wall prototype components for ITER).

More detailed descriptions of JUDITH 2 can be found in [1, 54, 55]. The newest

machine improvement is the installation of a pressure controller for the main chamber.

2.2 Temperature measurement by pyrometers

To measure surface temperatures during tests different pyrometers were used. A two wavelength pyrometer type QKTR 1075 from Maurer GmbH monitored the surface base temperature. Its time resolution of 20 ms prevented an observation of the simulated transients ($\Delta t = 0.5$ ms), but gives a good estimate of the surface base temperature. Because of the two wavelength technique the emissivity is of less importance. However, this is only valid if the emissivity of the object does not differ much for the used wavelengths (grey body assumption). In general this is not the case, but the wavelength ranges used (1.4 – 1.75 µm, 1.6 – 1.75 µm) lie close together to minimise the error.

A second pyrometer was used to resolve the fast events. The KMGA 740–USB from Kleiber has a time resolution of 10 µs covering a range of 350 – 3500 °C and can easily monitor single transients. Hence it was used to check the correct application of transients by the test procedure and the temperature development during and after a transient. The device operates with a single wavelength range of 2 – 2.5 µm. A comparison of the base temperature measured by the (nearly) emissivity independent two colour pyrometer and the base temperature shown by the fast pyrometer allowed to determine an emissivity value that could be used for the fast pyrometer. As this value also depends on temperature the peak values (several hundred degrees higher than the base temperature) recorded by the fast pyrometer have a bigger error than the base temperature values. Tungsten emissivity increases with increasing temperature [13], hence the peak values are underestimated by the device. One should also note that measurements at the beginning of an experiment are more reliable, because the surface morphology (and hence the emissivity) can change due to induced damage.

An approximation of the temperature uncertainty due to the uncertainty of emissivity is provided by [56]:

$$\frac{\Delta T}{T} \approx -\frac{\lambda}{5\lambda_{max}} \frac{\Delta \epsilon}{\epsilon} \tag{2.1}$$

with the peak wavelength λ_{max} and the used spectral wavelength λ. The peak wavelength follows from Wien's displacement law and relates to the temperature of a black body by:

$$\lambda_{max} = \frac{c_3}{T}$$

with Wien's displacement constant $c_3 = 2.8977685(51) \cdot 10^{-3}\,\mathrm{m \cdot K}$.

Measured temperatures were compared with the values obtained by finite element simulation (chapter 5).

2.3 Post mortem examination methods

2.3.1 Imaging techniques

Surfaces of tested samples were investigated by different imaging techniques. The chosen methods depended on the damage. For roughened surfaces light microscopy and laser profilometry were suitable to characterise and document the roughness. The laser profilometer (Polaris from UBM Messtechnik GmbH) can measure surface elevations of ±500 µm with an accuracy of 10 nm using the reflection of a 670 nm laser. In most measurements a 3D surface topography with a lateral resolution of 4 µm in x– and y–direction was recorded. The roughness parameter R_a, which was used to quantify the roughness, is defined as the arithmetic average of the deviation from the average height $\langle z \rangle$

$$R_a = \frac{1}{MN} \sum_{m=1}^{M} \sum_{n=1}^{N} |z(x_m, y_n) - \langle z \rangle| \tag{2.2}$$

$$\langle z \rangle = \frac{1}{MN} \sum_{m=1}^{M} \sum_{n=1}^{N} z(x_m, y_n) \tag{2.3}$$

Cracked surfaces were investigated best by scanning electron microscopy, mainly to investigate the morphology of crack edges, extreme roughening and melting and to distinguish strong roughening from cracks. Often both, secondary electron (SE) images and backscattered electron (BSE) images, were made. Secondary electrons mainly provide topographic information, while backscattered electrons provide information about chemical composition (heavier elements reflect more electrons and hence appear brighter). Backscattered electrons were also used for Electron Backscatter Diffraction (EBSD) to investigate the crystallographic orientation of a roughened surface area (section 5.2.2). This technique uses the patterns formed by electrons backscattered from different atomic lattice planes according to the Bragg condition to examine the crystallographic orientation of individual grains. A flat (polished) sample surface is crucial in order to get good results with this method.

2.3.2 Metallographic analysis

The crack depth is of particular interest to characterise the development (if any) of material deterioration. For this analysis cross sections of cracked samples were prepared. The sample is cut (by diamond wire cutting) leaving 2–3 mm of material for grinding and polishing. Grinding with SiC-paper and polishing with diamond suspension of 6–0.25 µm particle size reveals the cracks. The last preparation step was etching with a solution of NH_3, H_2O_2 and pure water (mixing ratio 1:2:7), giving a better visibility of cracks and grain structure/boundaries. Light microscope images were taken before and after etching, since it is sometimes easier to distinguish a crack from a grain boundary in the un-etched picture.

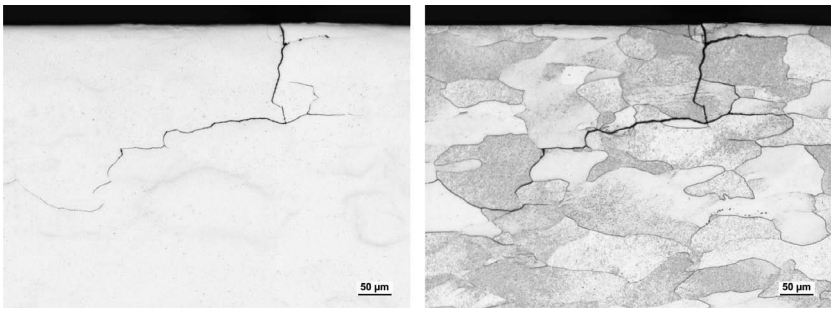

Figure 2.4: Light microscope image of a cross section of a cracked tungsten surface before and after etching.

2.4 Finite element temperature calculations

The finite element method (FEM) is a numerical technique mainly used to approximate solutions for partial differential equations. It it widely used in engineering and technology fields, for example the automotive and aeronautical industry, to calculate mechanical stresses, displacements, temperatures, flows of fluids etc. as well as their respective changes with time. In this work the finite element calculation software ANSYS 12.0.1 was used to predict the surface temperatures during experiments. First, the base temperature was of interest. The base temperature is the surface temperature immediately before a THL. It is determined by the thermal properties of the tested material, the sample geometry, the cooling power and the energy (SSHL + THL) intake. Because of the results of the FEM simulations the two wavelength pyrometer mentioned above (sec. 2.2) was chosen (it covered the appropriate temperature range). Second, the time necessary to achieve a dynamic equilibrium between heating and cooling should be determined (fig. 5.5). Third, a good estimation of the temperatures during a THL was of interest, especially to know the peak temperature. This temperature could not be measured by pyrometer, because of temperature dependence of the emissivity and insufficient positioning precision of the pyrometer spot/loading spot.

3 Test procedure development

To develop a test procedure for high cycle ELM–like loading with JUDITH 2 was a major aspect of this work. This chapter describes the development that led to the final test procedure. JUDITH 2 was not designed for this kind of tests and some experience with the machine had to be gained in order to achieve the desired result. Mock up design changed over time along with the development of the method (section 3.1).

The first tests showed the necessity for a sophisticated guidance of the beam on the sample surface. Therefore a circular pattern (section 3.4) was developed. It required more precise data on the beam diameter than existing at that point. This lead to improved beam diameter measurements (section 3.5) that provided the data for the final test procedure (section 3.6).

3.1 Mock up design development

In first tests an actively cooled flat tile module with a copper alloy heat sink was used (fig. 3.1). The PFM was cut from pure rolled tungsten plates (ITER reference grade [57]) with tile sizes of $12 \times 20 \times 5$ mm^3 and brazed to the heat sink. This

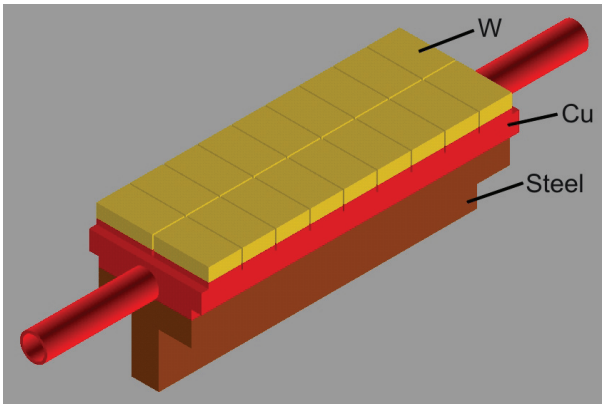

Figure 3.1: First mock up geometry: 18 tungsten tiles (rolled plate ITER grade) brazed to a copper cooling block, supported by a steel structure.

module was already used for thermal fatigue tests, but showed no severe failure and only a fine superficial crack network visible in SEM pictures. This was regarded as sufficient for some preliminary tests.

A new sample geometry was designed for the second campaign (fig. 3.2). As shown in chapter 3.3 the beam guidance was not satisfactory in the first experiments, hence the new tiles were designed with a larger area, facilitating the aiming with the beam. Three tiles were placed in a row, separated by gaps that allowed some thermal expansion during brazing. The tiles were separated by a significant distance in case

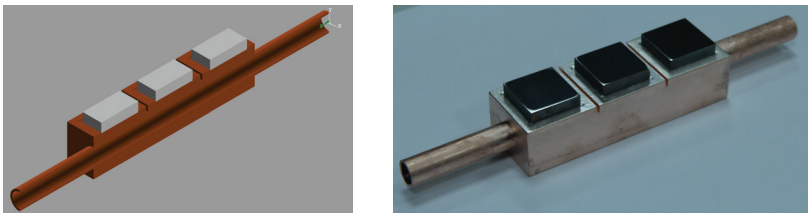

Figure 3.2: Second mock up geometry: Three tungsten tiles ($20 \times 20 \times 5$ mm^3) were brazed on a copper cooling block with a silver–copper solder.

they were used for independent experiments. The cooling structure was made of pure copper, the tungsten tiles are again made from pure tungsten, but of a different grade, described in section 4.1. They were brazed to the copper with a silver based solder foil as described in [58]. Smooth wetting and sound joints were achieved with this solder. This was verified by metallographic investigations of the cross section (fig. 3.3). The verification was mainly done because of the relatively big joint area that leads to higher stresses compared to the brazing tests done in [58].

The third design is an optimisation of the second. The materials did not change, only the geometry. It was optimised for the brazing process (deeper pools) and the mounting in JUDITH 2 (thicker cooling tube wall for higher stability). The tungsten tiles were downscaled to $12 \times 12 \times 5$ mm^3 as this is the standard specimen size used in many thermal shock tests in JUDITH 1 and in order to save material. The experience gained during the tests on the second design and the use of an aiming procedure allowed to decrease the size, because it seemed feasible to hit samples of this small area. The inner tube diameter was 8 mm, the distance between joint and tube inner wall 5.5 mm. All final experiments were performed with this design or with a similar design that had an additional place for a steel tile (fig. 3.4, 3.27). This steel tile was used for aiming (see sections 3.3 and 3.6 for the different aiming procedures).

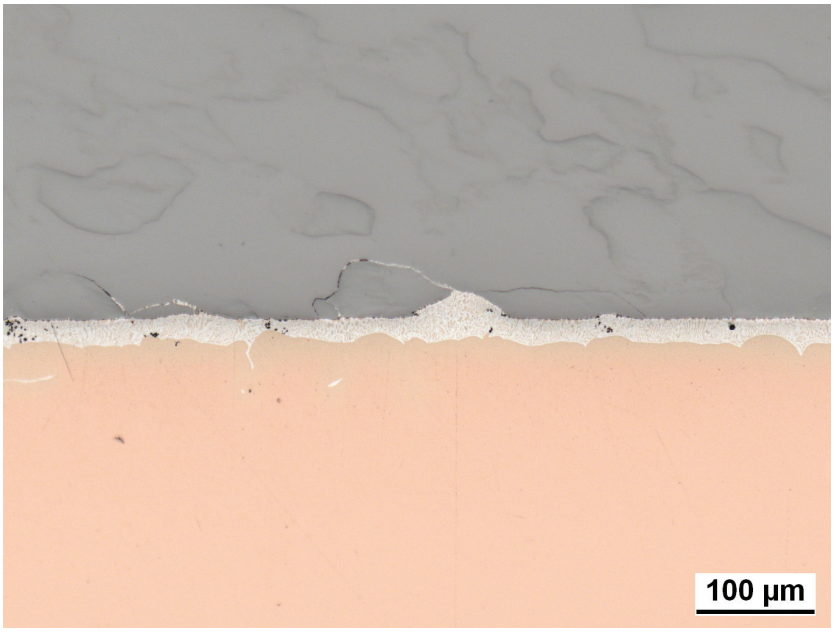

Figure 3.3: Light microscope image of a cross section of the braze joint between copper heat sink and the PFM tungsten with Ag–based solder.

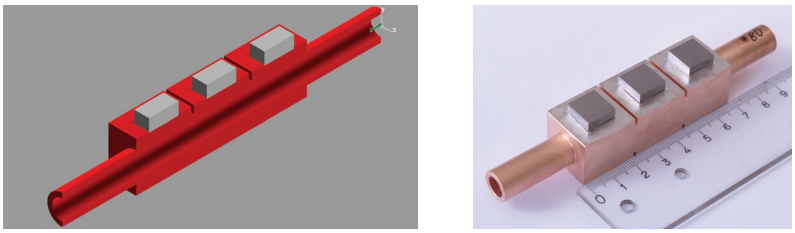

Figure 3.4: Third mock up geometry: Three tungsten tiles ($12 \times 12 \times 5$ mm^3) were brazed on a copper cooling block. A later design included a place for a fourth tile. A steel tile (same size as the tungsten tiles) was put in this place and used for aiming with the beam (fig. 3.27 and appendix B.1).

3.2 Beam profile and guidance

Simulation of ELM-like heat loads with electron beams leads to the problem of a homogeneous loading. The electron beams of JUDITH 1 and JUDITH 2 have a Gaussian shape, meaning energy/power is distributed as shown in figure 3.5. JUDITH 1 solves this problem by scanning at high frequencies (see 2.1.1), thus loosing flexibility but gaining a fairly homogeneously loaded area. The freely programmable beam path of JUDITH 2 makes it necessary to carefully design the experiment and to investigate the generated energy distribution beforehand. A detailed knowledge of the beam profile and guidance is crucial.

The aim of a homogeneously loaded area of a certain size is of interest because post mortem analysis and clear results depend on it. However, ELMs do actually not load PFCs homogeneously, but have a so called "footprint" of several millimetres width [33]. A limited loading area, surrounded by unloaded material is hence highly application relevant.

First beam shape measurements [1] with JUDITH 2 showed that the profile depends on various parameters: adjusted machine power, voltage, vacuum pressure, z-height (distance from electron source) and magnetic lens currents. These currents ($I(L_1)$ and $I(L_2)$) are given as percentage values of the maximum possible current.

The measurements also showed that the beam profile can be approximated by a Gaussian function and that the highest power densities are not achieved at highest machine power. The beam focussing is better at lower power thus allowing higher power densities. On the other hand, adjusting the machine power to values lower than $\approx$ 40 kW is only possible when switching to a mode with slow power control (so called TL-mode [1, 55]). In this mode the machine power can fluctuate and also needs several seconds at the beginning of an experiment to achieve full power. All measurements with JUDITH 2 were hence performed in the fast SL-mode.

The power density L of a Gaussian beam in a (x,y)–plane perpendicular to the beam direction is given by:

$$L(x,y) = L_0 \cdot e^{-\frac{x^2+y^2}{2\sigma^2}} \tag{3.1}$$

$$L_0 = \frac{P}{2\pi\sigma^2} \tag{3.2}$$

L_0 is the power density in the centre of the beam, σ the standard deviation (here: characteristic beam width) and P is the machine power. Calculations can be made to figure out the exact loading conditions at every spot of the sample and at each time point during the loading cycle. To facilitate these calculations a program called "Beambam" was developed.

The program is able to switch between a continuous scan mode, which is suitable for calculations for JUDITH 1 tests (fig. 2.2), and a point–to–point scan mode for JUDITH 2 experiments (fig. 3.8). Continuous scan mode is characterised by four parameters: The deflection frequency of the electron beam and the dimension of the

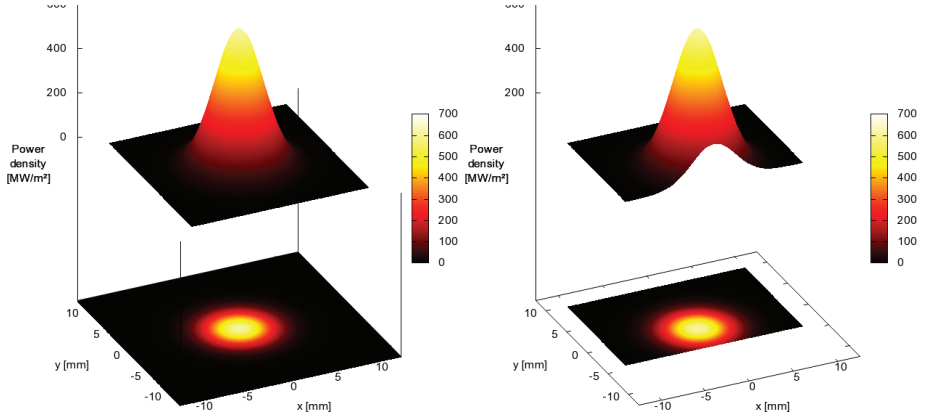

Figure 3.5: Gaussian power density distribution of the electron beam in JUDITH 2 at 44 kW with a reflection coefficient of $R_W = 0.45$ (for a tungsten surface). On the right side: Loss of part of the beam due to the geometry. This loss has to be considered when calculating a mean power or energy density for the sample.

sample, both for x– and y–direction.

Point–to–point scan mode uses a data file that contains a sequence of x– and y–positions for the beam (fig. 3.8). The dwell time for these "spots" is also defined in the file. In Beambam, individual dwell times for the spots are allowed. In the beam guidance software of JUDITH 2 the dwell time is fixed and identical for all spots. To circumvent this restriction, one can choose a small dwell time and repeat a point several times in the path file to accumulate dwell time for this point. Beambam can convert a point–to–point path file to a machine readable file for the use with the JUDITH 2 beam guidance software. However, any dwell time information is lost and the user has to set it in the beam guidance software.

For the experimental setup the following data are necessary: electron beam parameters, sample dimensions, information about positions (e.g. number of tiles on the sample, gaps) and the aforementioned scan path. The program assumes a rectangular sample holder with a sample consisting of an arbitrary number of tiles, ordered in rows and columns, separated by gaps. Two examples are shown in figure 3.7. The user has to input the tile and sample holder dimensions, as well as the number of rows and columns and the gap width to define the sample. Everything is defined in top view, the z–dimension is neglected. A point of interest (POI), a line of interest (LOI) and a region of interest (ROI) can be defined to get information about, for example, power density at that point/line/region. The coordinate system for all these positions and dimensions has its point of origin in the lower left corner of the setup (fig. 3.7). The program can generate pictures (via the software gnuplot), showing the path file on the sample (fig. 2.2, 3.6, 3.8, 3.9), energy density (fig. 3.6)

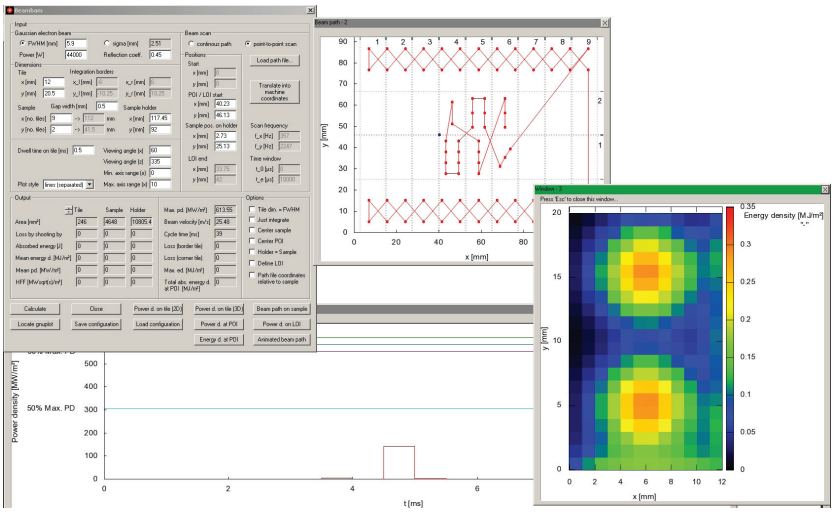

Figure 3.6: Beambam user interface. The main program window is shown in the upper left corner. Also shown: The visualisation of a point–to–point beam path (red) with the point of interest (blue) (upper right), the energy density distribution for one of the tiles (lower right) and the power density vs. time diagram for the point of interest (lower left).

and power density maps (fig. 3.10) or power density vs. time diagrams for the POI (fig. 2.2).

The first experiments used a simple pattern: several single spots hit a tungsten tile with a dwell time of 0.5 ms each. Every spot represented an ELM–like loading. The different number of spots on a tile resulted in different average heat loads and hence different surface temperatures. Beambam was first used to calculate the average power density, taking into account losses by geometry (fig. 3.5) and electron reflection. Second it calculated the beam centre power densities using the beam diameters of [1]. These first tests provided valuable results about the beam guidance, that led to the insight that an improved loading pattern was necessary. The novel circular beam loading pattern (section 3.4) has a similar feature to the JUDITH 1 sweeping tests: the beam is moving during the event. One ELM-like load was hence realised by the application of a lot of spots with the minimum dwell time of 5 µs.

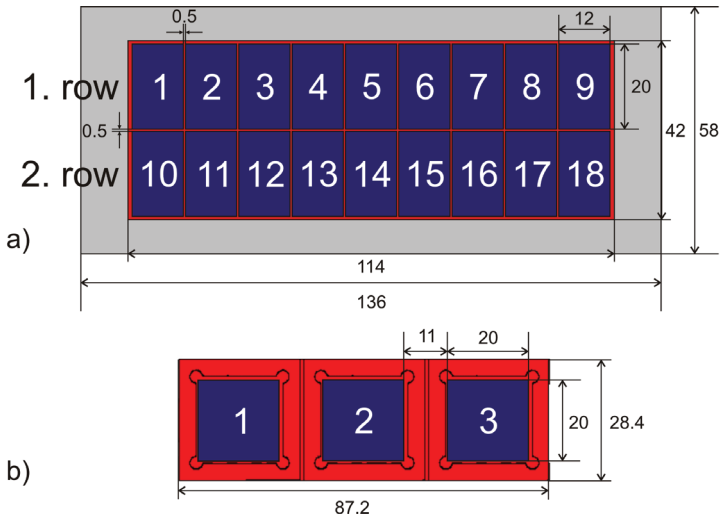

Figure 3.7: Top view of two mock ups. All dimensions are given in mm. Cooling tubes are ignored as they are not of interest for the surface loads. The tiles are coloured in blue, the sample in red and the (optional) sample holder in grey.

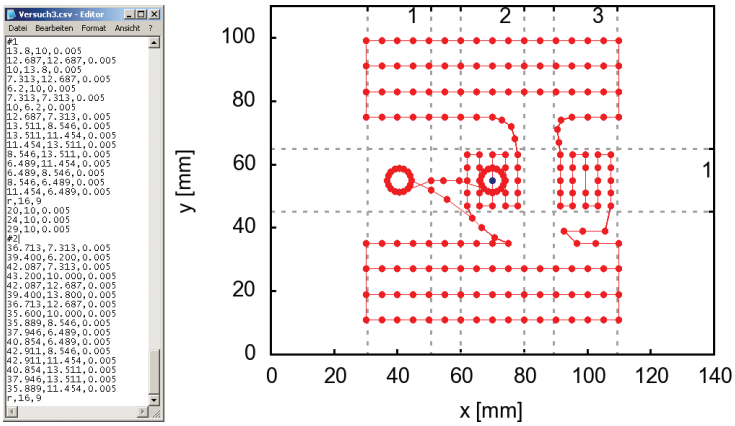

Figure 3.8: Point–to–point path file and beam path. The complete file produces the path on the right (the coordinates on the left only determine the two circular structures). The "r" command with the two parameters is interpreted as "repeat the last [parameter 1] points additional [parameter 2] times". Lines beginning with '#' are ignored (comment line). The sample dimensions are depicted in figure 3.7b, the coordinates in the file are given relative to the lower left corner of tile 1.

3.3 Procedure and results for the first mock up

The beam path chosen for the first experiment on the first mock up (section 3.1) is shown in figure 3.9. A dot represents a spot where the electron beam stays for 0.5 ms. The path can be divided in three regions that contain the same patterns. Each of these patterns was loaded with a certain number of cycles. The different patterns had three purposes. First, to achieve different mean power densities, roughly 1 MWm^{-2} per spot (fig. 3.10). This results in different surface temperatures for the individual tiles. Second, to investigate the effect of the Gaussian beam shape, e.g. the necessary distance between single spots to not influence each other. Third, to test the accuracy of the beam guidance of JUDITH 2.

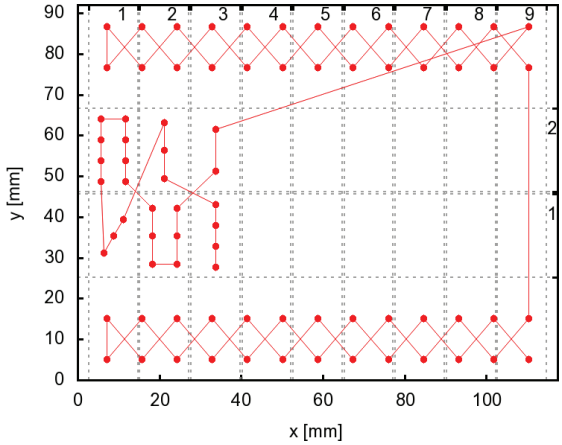

Figure 3.9: Beam path on the first mock up: Each dot represents a spot where the beam stays for 0.5 ms, simulating an ELM–like heat load. The different spot numbers result in different surface temperatures. The top and bottom part of the pattern load the beam dumps. The centre part covers one third of the mock up (six tiles).

The power density L_0 in the beam centre is defined by machine power and beam diameter (eq. 3.1). The beam diameter data found in [1] were used here. In order to get a high power density, the most favourable ratio of power and beam diameter was found to be at a power of 44 kW (5.9 mm FWHM value, lens currents and pressure optimised), resulting in $L_0 = 1.1$ GWm^{-2}. At these parameters the beam did not only have the highest power density of all measured parameter sets in the region of SL-mode (the faster of the two operational modes of JUDITH 2), but its diameter and therefore the power density was also relatively constant over a broad vacuum pressure range [1]. Taking into account the reflection coefficient for tungsten ($R_W = 0.45$), only 0.61 GWm^{-2} were absorbed. This means 0.3 MJm^{-2} absorbed energy density per spot for 0.5 ms dwell time. In order to increase the energy density the

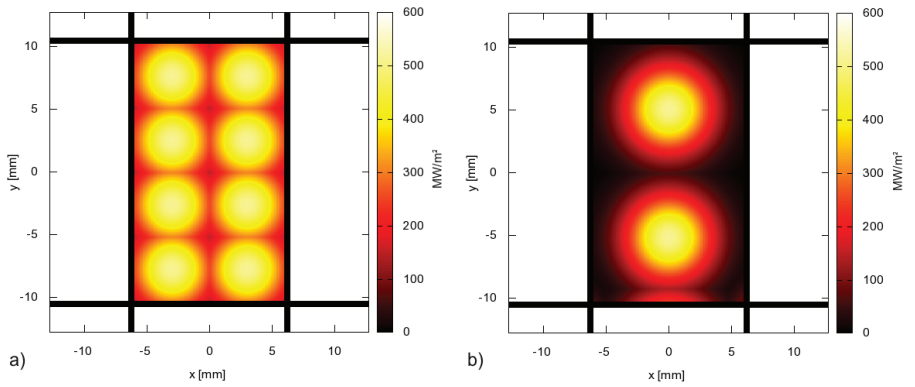

Figure 3.10: Power density distribution on tiles 1 and 3: The maximum value of 1.1 GW/m^2 is not reached because tungsten reflects about 45% of the electron energy.

pulse duration had to be increased. For a dwell time of 0.7 ms 0.43 MJm^{-2} were reached.

The aforementioned first mock up (called FT141-1, fig. 3.1) was loaded with the described pattern (fig. 3.9), that was divided into three sections. These were not loaded at the same time, but successively, applying 10^3, 10^4 and 10^5 pulses with a frequency of 25 Hz, a peak power density of $L_0 = 0.61$ GWm^{-2} and a dwell time of 0.5 ms (0.3 MJm^{-2}, fig. 3.9). The tiles showed no visible change (fig. 3.11a), even after 10^5 shots. Therefore the dwell time was increased to 0.7 ms in the second pass and again one third of the sample was exposed to the beam. The tungsten surface then showed severe cracks after 4000 cycles (fig. 3.11b). The cracks did not span the whole sample, not even for the closest arrangement of spots (fig. 3.10a). This might be attributed to the shift and extension of the real spot pattern compared to the desired one. As can be observed in figure 3.11b the beam guidance had to be optimised. The guidance was tested immediately before starting an experiment by usage of a steel plate that was mounted above the sample. The electron beam was switched on for a short time ($\approx$ 1 second), leaving traces of molten steel as in figure 3.12 (aiming procedure).

From the extension of the crack network a first approximation of the energy density threshold for the onset of cracking could be made. The cracks extended to a radius of 1.9 mm (minimum value in x-direction), which is related to a power density of 0.46 GWm^{-2} or an energy density of 0.32 MJm^{-2}. As this was the same value as the peak value of the first experiment (within experimental error margins) it may indicate a worse beam focussing in the first experiment.

To check whether the absence of any damage after the first pass might have been attributed to bad beam focussing, the first experiment was repeated with special attention to the beam parameters. Although the vacuum quality was not as good

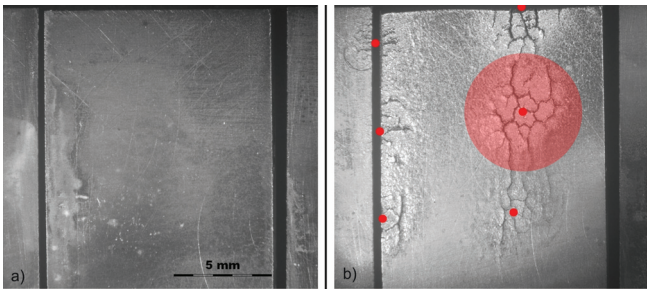

Figure 3.11: Light microscope image of the tile loaded according to figure 3.10a: **a)** after loading with 10^4 pulses of 0.5 ms (0.3 MJm^{-2}); **b)** after loading with additional 4000 pulses of 0.7 ms dwell time (0.43 MJm^{-2}). The dots indicate the electron beam centre, the circle the area within FWHM.

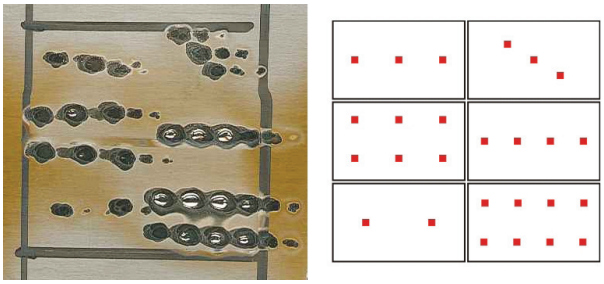

Figure 3.12: Steel plate to test the beam guidance. The molten spots indicate the beam centre position, the given pattern is shown on the right. Some "copies" of the clear spots are visible (e.g. in the upper right corner at the diagonal three–spot pattern). These occur because the machine needs a few tenth of a second to achieve full power and a stable operational state. During this time the beam deflection is still incorrect.

as desired, probably leading to a still not perfect focussing, the material showed cracks after 1000 cycles (fig. 3.13) on a yet undamaged part of the mock up. A minimum power density of 0.44 GWm^{-2} ($\rightarrow$ 0.22 MJm^{-2}) can be derived from the vacuum quality of $p_{av} \sim 3 \cdot 10^{-4}$ mbar. These results already showed: The beam was not well focussed in the first experiment because the chamber pressure was too high. The light microscope images also indicated that cracking just began. The cracks were much thinner than in the second experiment (however, one should keep in mind that the cycle numbers differ). It was decided to change the loading pattern and to prevent big distances between subsequent spots in order to improve guidance precision. A second motivation was to achieve a bigger homogeneously loaded evaluable area. It was also concluded that special attention had to be paid to the chamber vacuum pressure.

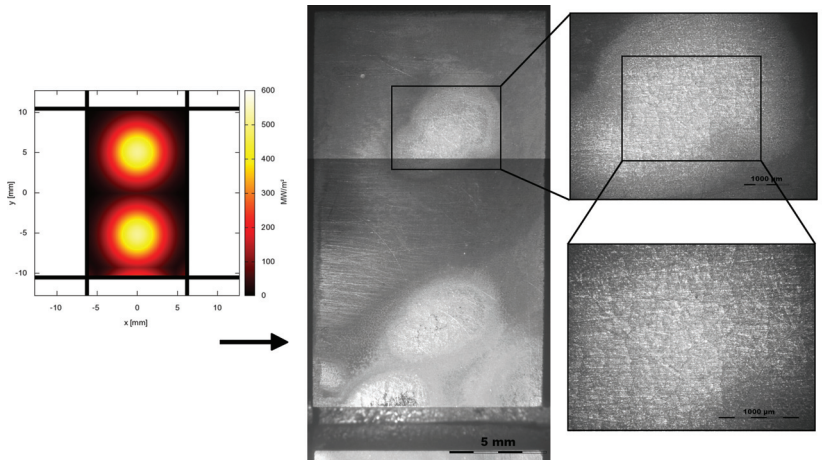

Figure 3.13: Light microscope image of the tile loaded according to figure 3.10b (small copy shown on the left) after 1000 cycles of 0.5 ms with improved beam focussing. The image in the middle is composed of two separate shots.

3.4 Circular beam loading method

The second generation mock up was used to test the new circular beam loading method and to get first results for the resistance of tungsten against high cycle transients. The new beam path used a dwell time of 5 µs per spot. This way a path can be designed with maximum flexibility. If the beam should stay on a spot for a longer time the position command can just be repeated. Because of the problems with the first experiments the path was designed to avoid any bigger gaps between subsequent spots. It applied ELM–like loads in a circular manner (fig. 3.14). Because of the great flexibility of the electron beam guidance system another possibility was considered: The interpulse time between subsequent loads of nearly 40 ms (at 25 Hz pulse repetition rate) can be used to apply a steady state heat load. This technique would allow to combine both types of loads (fig. 3.15) and create ITER relevant thermal loading conditions. However, first some considerations about the circular loading method were necessary.

The circular beam loading method was initially developed to increase the homogeneously loaded and evaluable area on the sample. As described in section 3.2 a beam path for an experiment consists of one or more spots. Loading test specimens with the Gaussian shaped electron beam in a single spot-like manner results in a small evaluable area around the spot centre, where loading is quasi-homogeneous. The radius r_p (distance from centre) at which the power density decreases to a

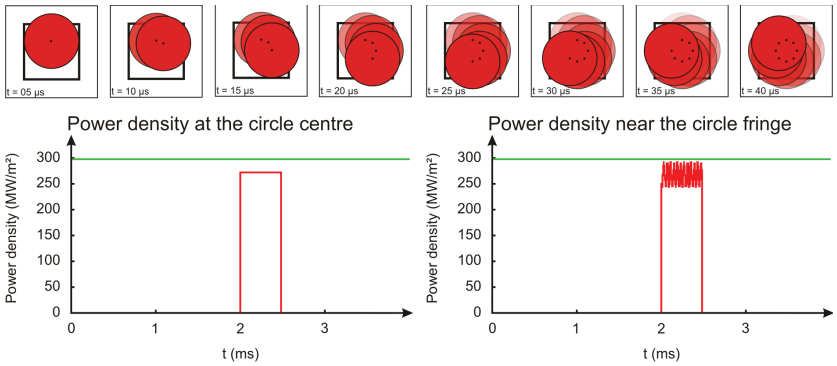

Figure 3.14: Circular beam loading method: The beam is guided around the loading centre in a circular path (top). This circle is repeated until the desired pulse duration is achieved (e.g. ≈ 0.5 ms). The resulting power density development in the centre and close to the circle fringe (but still inside) are shown below. The small power density fluctuations of $\approx 10\%$ are accepted and the circle area is regarded as homogeneously loaded with the centre power density.

fraction p of the peak value is determined by

$$r_p = \frac{FWHM}{2} \cdot \sqrt{-\frac{\ln(1-p)}{\ln(2)}} \tag{3.3}$$

This means the evaluable area for a spot with a beam FWHM = 8 mm and an acceptable power density difference of 15 % compared to the beam centre ($p = 0.15$) is $r_p \approx 1.9$ mm. Choosing a stricter limit results in an even smaller evaluable area. To increase this area the beam is guided in a circle, consisting of eight spots loaded with the minimum dwell time of 5 µs each. Hence the beam rotates around the loading centre at a fixed distance. An example of such a beam path is shown in figure 3.15. The combined heat loads on the centre tile of the depicted specimen simulate ITER relevant conditions of ELMs and ≈ 5 MW/m^2 (absorbed) steady state heat load. Within the duration of an ELM-like loading of 0.48 ms the beam circulates 12 times. The power density of the beam has to be increased to achieve the same power density in the centre of the circle as in the centre of a spot-like loading. A comparison of the resulting energy densities for spot-like loading and circular beam path loading is shown in figure 3.16. The results of the experiments with the second generation mock ups (fig. 3.15 & 3.17) using relatively wide circle radii (3.8 mm at FWHM = 6.55 mm, fig. 3.15 & 3.26) showed that the beam follows the circular path precisely, but the radius of the circle has to be small compared to the beam FWHM; otherwise the difference in power densities of circle centre and beam centre produces an inhomogeneous loading. This became obvious due to an inhomogeneous surface roughening, clearly following the circular beam path

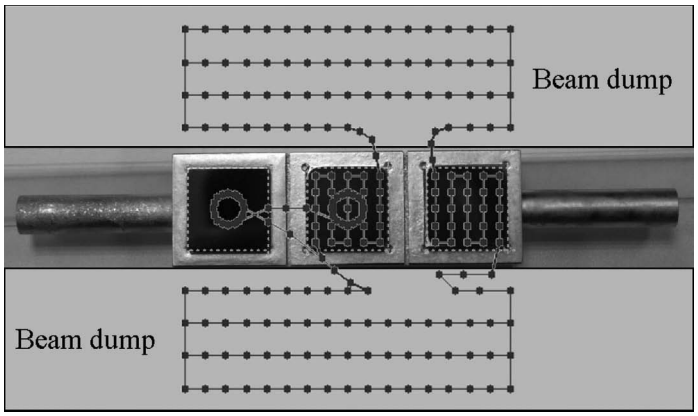

Figure 3.15: Top view of the beam path for a combined ELM + steady state heat load experiment on the second generation mock up (background). Every dot represents a spot where the beam stayed for 5 µs. The path shows three differently loaded areas (from left to right): ELM-like only, ELM-like + steady state, steady state only. During interpulse time the beam moved between the two beam dumps and applied steady state load.

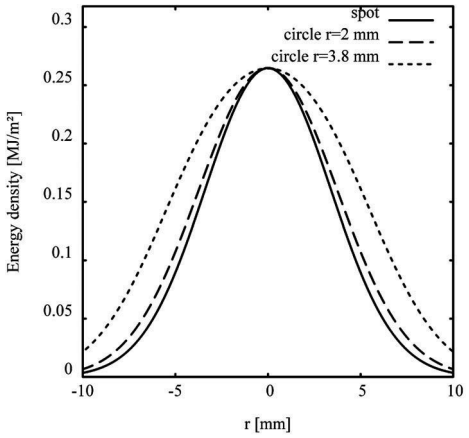

Figure 3.16: Comparison of energy densities for spot-like loading (power 40 kW) and circular beam path loading with a radius of 2 mm (power 47.6 kW) and 3.8 mm (power 74.7 kW). A FWHM of 8 mm and a pulse length of 0.48 ms are valid for all three curves.

(fig. 3.17). The roughening was more pronounced in case of additional SSHL (higher surface temperature). The calculated difference in power densities of beam centre and circle centre is depicted in figure 3.18, normalised to the beam centre power density, for three FWHM values as a function of circle radius. In order to estimate

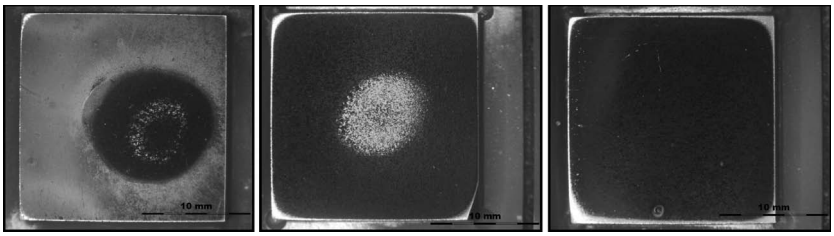

Figure 3.17: The sample tiles of the experiment shown in figure 3.15 after loading. Experimental parameters: absorbed power density in the beam centre 0.49 GW/m^2, absorbed power density in the circle centre 0.2 GW/m^2 (radius 3.8 mm), pulse duration 0.8 ms (pulse duration was increased to achieve a higher energy density), ELM frequency 25 Hz, number of ELMs 10000. Beam (0, 0) coordinate is in the centre of the middle tile. Comparing the left and centre pictures shows that beam guidance is best if the pattern is close to the (0, 0) position.

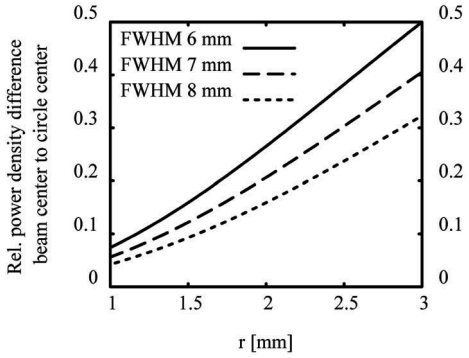

Figure 3.18: Difference in power densities between circle centre and beam centre, normalised to the beam centre power density, for three FWHM values as a function of circle radius.

an acceptable radius and also to show that the 5 µs spots of the circular pattern do not cause degradation effects on their own it is quite useful to use the heat flux factor (F_{HF}):

$$F_{HF} = L \cdot \sqrt{t} \tag{3.4}$$

L is the local power density and t the period this power density loads a surface. The heat flux factor is proportional to the surface temperature increase caused by the heat flux [59, 60]. Thus it is directly connected to the stresses induced by the temperature gradients that occur during THLs. F_{HF} is suitable for comparing loads with different power density and pulse duration parameters, as long as the time scale is similar (e.g. comparison of 0.5 ms tests and 1 ms tests or 5 ms disruption simulations in JUDITH 1 and 2). A comparison of F_{HF} of a spot-like loading or a complete

circular load (FWHM = 8 mm, L = 1 GWm^{-2}, t = 0.48 ms) of 21.9 $MWm^{-2}\sqrt{s}$ and F_{HF} of a single shot in a circular pattern of radius 2 mm (FWHM = 8 mm, L = 1.2 GWm^{-2}, t = 5 µs) of 2.7 $MWm^{-2}\sqrt{s}$ shows a difference of one order of magnitude, ensuring a 5 µs pulse has no impact on its own. This can also be seen experimentally: the steady state heat loading path in figure 3.15 consists of 5 µs spots that produce an average steady state heat load of 4.4 MW/m^2 (absorbed) during the experiment. The sample tile does not show any surface modification (roughening, swelling or cracking) in that area (fig. 3.17). It was verified by light microscopy, SEM and laser profilometry that no detectable changes occurred compared to the sample surface before loading.

A radius of 2 mm at a beam FWHM of 8 mm would increase the evaluable area by $\approx$ 400%, using an acceptable power density difference of $p = 0.15$. But as the experiments showed it is also necessary to consider the energy density when defining the evaluable area. A comparison of energy densities (fig. 3.16) shows: the broadening of the energy density distribution is small for such a small radius. Defining the evaluable area by a certain absorbed energy density leaves an increase in evaluable area of only $\approx$ 10–20 %.

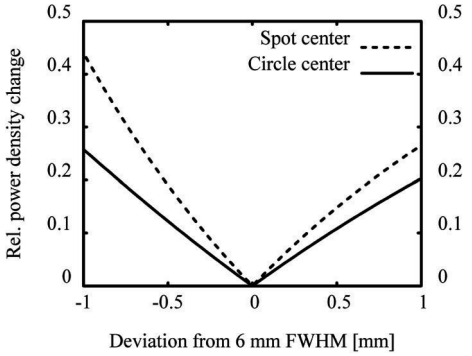

Figure 3.19: Power density change for a beam with FWHM = 6 ± 1 mm relative to a beam with an exact FWHM of 6 mm for spot-like loading and for the centre of a circular beam path. It is clearly visible that the circular beam path has the advantage of an increased stability against variations in FWHM.

However, the circular beam path shows another beneficial effect: It provides a better stability against changes in beam FWHM caused by e. g. vacuum quality variations. As an example figure 3.19 shows the power density change for a beam with FWHM = 6 ± 1 mm relative to a beam with an exact FWHM of 6 mm, both for spot-like loading and for the centre of a circular beam path.

Summarising the obtained results and theoretical considerations four conclusions can be drawn: First, the circle radius has to be small compared to the beam FWHM that itself has to be small to achieve the necessary power densities. Despite the marginal increase of evaluable loaded surface area, circular beam loading is a useful

method, as it additionally shows an improved stability against changes in beam FWHM. Second, the experiences during testing and the results showed that the electron beam achieved the best precision if the desired pattern was close to the origin of ordinates. Third, the application of additional SSHL did not pose any problems and led to significantly different material response. Fourth, the material showed roughening, a degradation which is notable but less severe than cracking. Hence the used load was already in a region of interest. The circle centre was loaded with 10^4 pulses of 0.8 ms duration and 0.2 GWm^{-2} power density. This corresponds to $F_{HF} = 5.7\ MWm^{-2}\sqrt{s}$. Although the chosen circle radius was too wide, this number served as first estimate for the planning of following experiments. In order to find a damage threshold, the intensity had to be decreased below this heat flux factor.

3.5 Improved beam profile measurements

The results of the first tests and the theoretical calculations regarding the new circular loading method showed the need for more precise beam profile measurements, in particular to characterise the influence of vacuum pressure on beam diameter. A series of tests was started with a new beam profile measurement technique[1].

3.5.1 Experimental setup

Three tungsten wires/rods were mounted on a supporting structure from which they were electrically isolated by small ceramic cylinders (fig. 3.20). The wires have to be parallel and the distance d between them has to be known. Each of the wires was connected to a cable that conducts the electric current absorbed by the wire. This current was indirectly measured with an oscilloscope by the voltage drop across a resistor.

Tungsten was chosen as wire material for its high melting point, high thermal conductivity and low electron absorption, minimising the risk of a local overheating. The high electron reflection ($R_W \approx 0.45$) leads to a lower absorbed heat load while not changing the signal shape (only the intensity).

The earthed support structure was made of copper to avoid electrostatic charge effects and to quickly conduct away any heat. It was placed in the test chamber of JUDITH 2 together with two beam dumps, water cooled copper blocks that are used to absorb the major part of the incoming power.

[1]This method was developed by Dr. Axel Schmidt and Andreas Bürger and is being patented under filing no. 102010025123.2, filing date: 25.06.2010

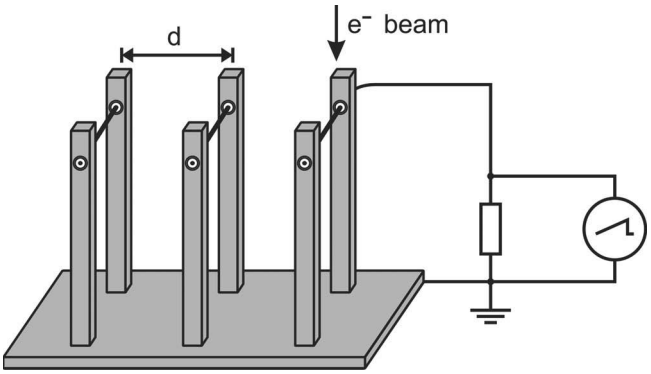

Figure 3.20: Experimental setup for the beam profile measurements. The support structure is made of copper, the wires of tungsten and small (white) ceramic cylinders isolate them from each other. The current through each wire was measured with a resistor and an oscilloscope, shown exemplarily on the right for the first wire.

3.5.2 Experimental procedure

The electron beam was guided back and forth between the two beam dumps passing the three wires (fig. 3.20, 3.21). The oscilloscope signal is observed and recorded. It depicts the electron current versus time. To get a spatial distribution of the passing electron beam (current) the two outer wires are used: With the knowledge of the distance d between the wires and their respective signal differences a beam velocity can be calculated, allowing converting the time information to distances.

As many parameters influence the beam shape and machine time is limited a few chosen sets of parameters were studied up to now. The z-height in the chamber was always kept constant at the working height of standard test specimens in the chamber [54]. At least ten measurements were recorded for every set of parameters. Each measurement was evaluated by fitting Gaussian functions to the data and calculating the conversion factor (beam velocity). A Gaussian function was chosen because of several reasons. First, it describes the beam shape well and was already successfully used in former measurements. Second, it provides a single parameter defining the beam diameter: the Full Width at Half Maximum (FWHM) assuming the beam is approximately symmetric which was shown in [1]. Third, the described setup always absorbs all electrons along the wire, meaning it integrates over one dimension. For a Gauss function fit this does not change the result for the FWHM. The FWHM is used to quantify the beam diameter. An exemplary measurement and fit are depicted in fig. 3.22.

For all measurements the main chamber pressure was controlled manually by a needle valve as the automatic pressure control was not yet installed at that time.

The setup was tested with different wire diameters as it is desirable to use a

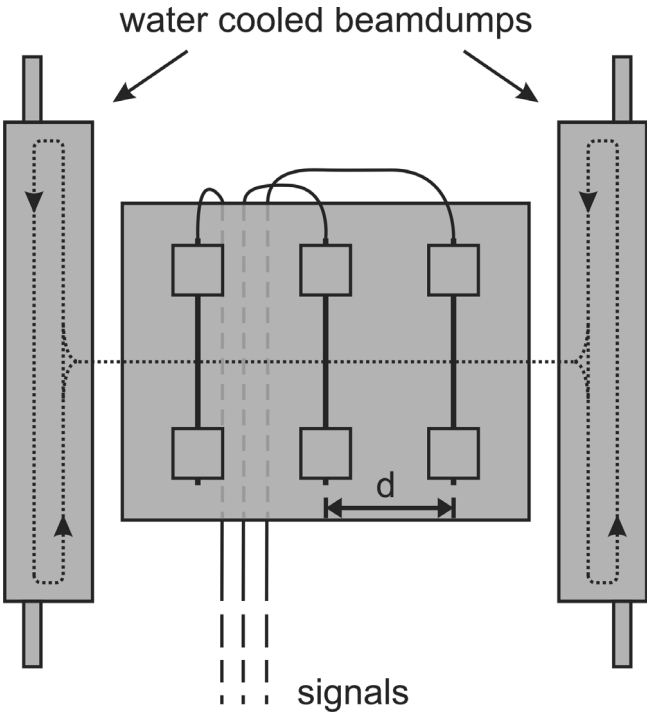

Figure 3.21: Experimental procedure for the beam profile measurements (top view of fig. 3.20). The beam mainly circulates on the beam dumps which absorb and dissipate the heat. From time to time the beam is led across the wires to the other beam dump. This gives a measurable signal through the wires which can be seen on the oscilloscope screen. It is recorded for later analysis.

small wire thickness for a better resolution while this approach might lead to local overheating. Different beam velocities were also tested.

3.5.3 Results

The tests with different wire thicknesses showed no problems due to overheating in any case for machine power up to 100 kW, even at the lowest beam velocities (higher powers have not been tested yet). Nevertheless thin wires were difficult to handle and did not keep in place/shape due to bending and sagging. A significant improvement in resolution could not be observed for the thinnest wires anyhow. The beam shape could directly be observed on the oscilloscope screen (fig. 3.22). It was also recorded and analysed as described providing a mean FWHM value and a standard deviation for each set of parameters (fig. 3.23).

Several measurements showed that focussing improved with decreasing chamber pressure (fig. 3.23). In [1] it was shown that further decreasing the pressure

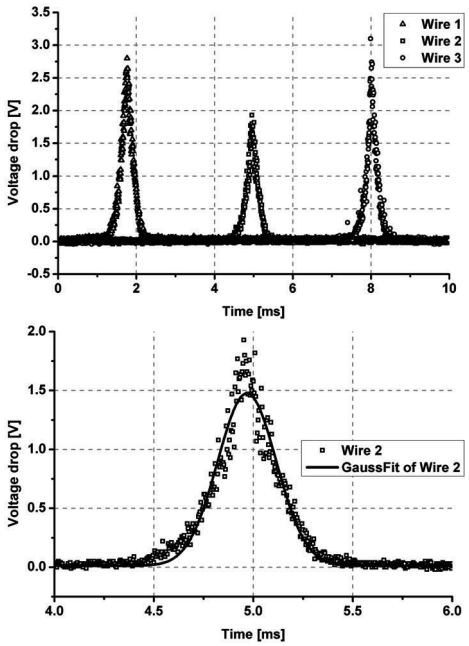

Figure 3.22: (a) Beam profile measurement at P = 38 kW machine power, U_a = 50 kV acceleration voltage, main chamber pressure $p_{chamber} = 3.5 \cdot 10^{-4}$ mbar, magnetic lens currents $I(L_1) = 100$ %, $I(L_2) = 40$ %. The outer wires 1 and 3 are thicker than the centre wire and therefore produce a signal of higher amplitude. **(b)** shows the centre wire signal only with a Gauss fit. The FWHM for this (single) measurement is 5.43 ± 0.11 mm.

led to a defocussing again, meaning an optimum pressure range exists. However, this could not be verified up to now as lower main chamber vacuum pressure than $1.3 \cdot 10^{-4}$ mbar could not be achieved during these calibration campaign. The active cooling might have been a reason for this, as experience shows that an increasing number of pressurized flanges leads to decreasing vacuum quality. An increased dependency of the beam FWHM on the focussing lens current (stronger slope, pronounced minimum) as well as a shift of the minimum diameter towards higher lens 2 currents could be observed for decreasing pressure (fig. 3.23). The obtained diameter can be used to calculate the power density (L_0) in the centre of the Gaussian beam using equation 3.2 and the machine power P. The FWHM and σ are proportional:

$$\mathrm{FWHM} = 2\sigma\sqrt{2\ln(2)} \tag{3.5}$$

The maximum incident power density achieved was 2.8 GW/m^2 (at 43 kW, 50 kV, $1.3 \cdot 10^{-4}$ mbar, $I(L_1) = 100$ %, $I(L_2) = 38$ %).

The new measurement method for high power electron beams proved to work very well. In contrast to former methods it directly showed a beam shape on the

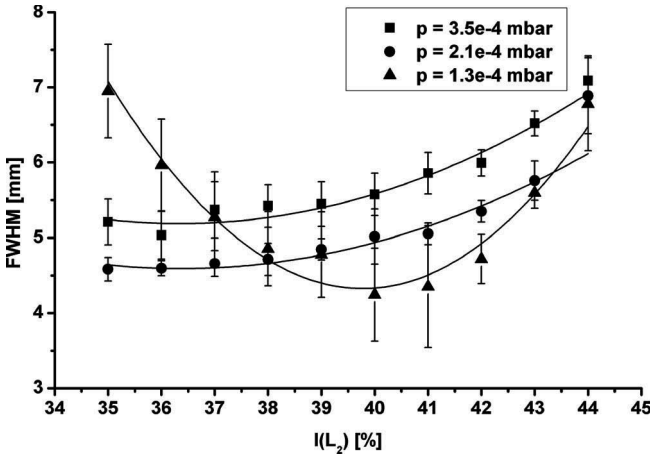

Figure 3.23: Dependency of beam FWHM on lens 2 current ($I(L_2)$) and chamber pressure at 38 kW machine power, 50 kV acceleration voltage, $I(L_1)$ = 100 %. Every data point is an average of at least ten measurements. The error bars show the standard deviation, the lines are fitted polynomials (2. degree).

oscilloscope screen during the measurement, enabling to change parameters and focus the beam while observing it. It was also the fastest method used so far and works for a machine power of at least up to 100 kW. The tests indicated that it will work for higher power too, as even the thinnest tungsten wires showed no problems. In case of overheating the beam velocity can be increased.

The complete results are listed in appendix C.

3.6 Final test procedure

The final procedure that was used for all the experiments consisted of several steps. In all calculations the absorption of the respective material has to be considered.

1. A desired transient intensity and SSHL had to be chosen.
2. A tolerable circle radius r_{circ} had to be calculated: Small enough that the power density in the beam centre L_0 is at most 10 % higher than the power density in the circle centre L_{abs} (acceptable power density difference $p = 0.1$).
3. A machine parameter set at which the beam power density fits the needs had to be found. The parameter sets used are listed in table 3.1.
4. An appropriate beam path had to be designed. It had to fulfil several requirements:
   - The distance between subsequent coordinates should be some millimetres at most.
   - The pattern had to be repetitive: experiments were carried out at 25 Hz

this meant a 40 ms pattern. At 5 µs dwell time per spot 8000 coordinates were necessary. The maximum number of coordinate points per file allowed by the guidance software is 2600 [55]. Hence the pattern consisted of at least two files, one for the transient load (the circle) and one for the interpulse time (beam dump and/or SSHL). The latter had to be repeatable. It usually consisted of roughly 200–400 coordinates which were repeated 20–40 times.

- Start and end points must be close, because the pattern is repeated (see first requirement).
- The transient load pattern (circle) was located around the origin of coordinates (best beam guidance accuracy).
- During interpulse time the beam had to be guided to the beam dumps to dissipate the heat (fig. 3.24).
- Heat load distribution on the beam dumps should be homogeneous and the load must not exceed 5 MWm^{-2} [61] to prevent damage.
- If a SSHL was required, the interpulse pattern got more complicated: The sample and the beam dumps had to be heated in turns with a frequency of roughly a millisecond in a meander-like pattern. The pattern had to span the sample tile area and even exceeded it in order to achieve a homogeneous load. Hence it depended on the beam diameter, because the beam diameter, its position on the tile and the tile size determine the losses (fig. 3.5). This meant a SSHL pattern had to be designed uniquely for each transient power density.
- The pattern had to be designed differently depending on the position of the tile (right, left, centre) to use the correct beam dump area. Heat load on the clamps had to be avoided as they overheated easily. However, a pattern for the right tile could be mirrored to obtain a pattern for the left tile. The mirror axis is a vertical line through the circle centre (not through the pattern centre) because the whole mounting table with the beam dumps is moved to place the circle centre at the origin of ordinates of the beam (fig. 3.25).

5. After mounting a sample in the JUDITH 2 machine an aiming procedure was necessary in order to hit the desired tile. This was either done by a steel plate that was placed on top of the sample (fig. 3.26) and removed after aiming or by a fourth steel tile (fig. 3.27). Aiming using a steel tile had two advantages: It was not necessary to open the machine after the aiming procedure to remove the steel plate. The aiming was also more precise because it is done on the same z-height as the tiles. In any case the beam was switched on for a second and the position of the transient load was observed as glowing spot via a video camera. Melt droplets on the steel revealed the impact position and allowed to precisely adjust the pattern with the beam guidance software. The sample was already installed in the approximate central position, hence only small

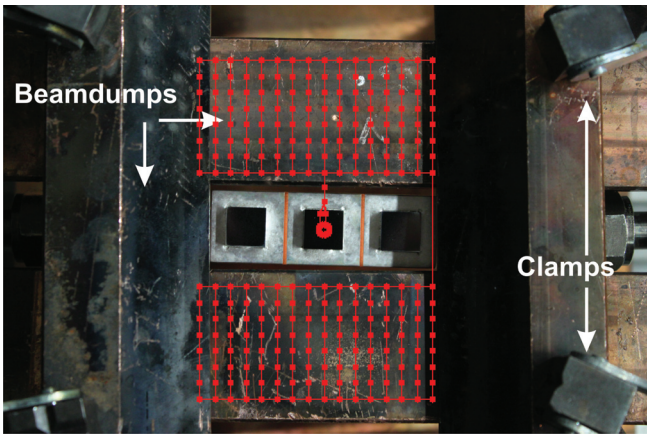

Figure 3.24: Top view of mock up mounted in JUDITH 2. The mock up (fig. 3.4) is surrounded by four beam dumps, actively cooled copper blocks, which are fixed by four clamps (partially visible in the corners of the picture). A simple beam path that applies THLs (circle) only on the centre tile is shown in red. Most spots of the path are located on the beam dump for heat dissipation, because the beam is not needed on the sample during 39.5 ms out of 40 ms.

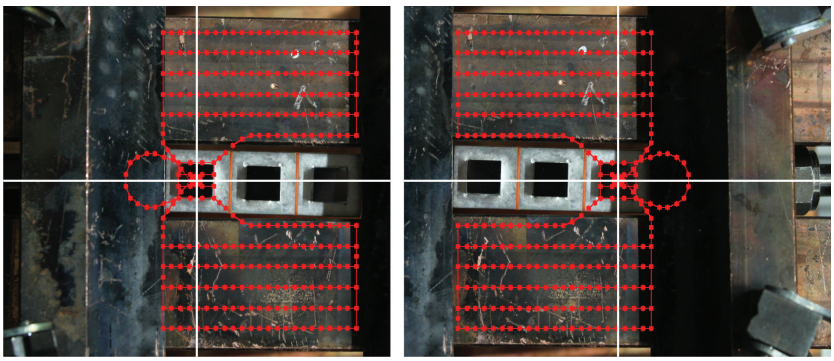

Figure 3.25: Top view of mock up mounted in JUDITH 2. An example of a beam path (red) that applies a combined transient and SSHL. The path on the left picture cannot be used for the centre or right tile as it would load the clamps. It can, however, be mirrored vertically and then be used for the right tile (mirror axis in the centre of the transient load circle) as it is shown on the right picture. The mounting table is moved to keep the origin of ordinates of the beam in the circle centre (white cross).

corrections were necessary. All machine parameters like power, acceleration voltage etc. and the pattern for the test always had to be used for aiming, otherwise the beam position can change. All cooling systems had to be in full

operation as well, because the high water pressure can move the whole setup when switching it on.

6. The pyrometer position had to be checked after aiming. However, due to geometric reasons (like small target area and beam dumps blocking the line of sight) it was very difficult to place the pyrometer correctly.

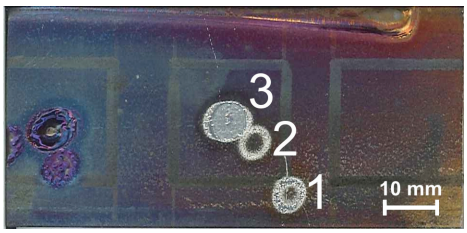

Figure 3.26: Surface of a steel plate used for aiming. The lines show the position of the tiles located below the plate. Melt traces of the first, second and third shot are clearly visible (numbers). After the last shot the plate was removed and the actual experiment was started. The plate was used in a test of the second mock up design (fig. 3.15) with $r_{circ} = 3.8$ mm. Although it became apparent that this radius is too large, the circles proved the working principle of the circular loading pattern (section 3.4).

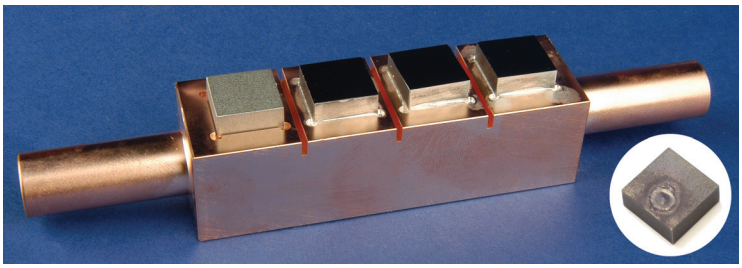

Figure 3.27: Mock up (final design) with fourth position for a steel aiming tile (leftmost). The lower right corner shows a steel tile after usage.

7. The beam dumps were used during experiments and had to be baked out (done with the beam dump pattern written for the test) before aiming, in order to get rid of water and dirt that clearly deteriorated the vacuum quality at first. This procedure only needed some minutes until vacuum pressure was stable.
8. The first tile was tested. Each tile usually has an individual pattern, because of different test conditions.
9. After testing the first tile the mounting table was moved to place the next tile at the central position. The next beam pattern was loaded and in most cases aiming had to be repeated for small corrections.

10. After all tests were finished the sample was demounted. At the same time attention was paid to the temperatures inside the chamber. The actively cooled parts (like the sample itself) were cooled to the coolant temperature within seconds, but some other parts, like the mirror for the infra-red camera could be destroyed by oxidation when ventilating the chamber too early.

Table 3.1: Parameter sets used for the tests after development of the final procedure. Due to different electron absorption coefficients different sets had to be found for each material. Lens 1 and 2 currents are given in % of the maximum current allowed (like in the software of the machine). The main chamber pressure was always $p_{chamber} = 3.5 \cdot 10^{-4}$ mbar.

F_{HF} ($MWm^{-2}\sqrt{s}$)	L_{abs} (GWm^{-2})	r_{circ} (mm)	Power (kW)	Voltage (kV)	I(L1) (%)	I(L2) (%)	FWHM (mm)
W ($R_W = 0.45$)							
3	0.14	2	43	40	100	40	11.88
6	0.27	1.5	43	40	100	34	8.36
7.5	0.34	1.44	43	40	100	30	7.41
9	0.41	1.2	40	50	100	42	6.61
12	0.55	1.05	40	50	100	39	5.67
CFC ($R_C = 0.03$)							
9	0.41	1.6	43	40	100	35	9.05
12	0.55	1.3	43	40	100	33	7.88
15	0.68	1.2	40	50	100	42	6.61

4 Experimental conditions and test matrix

4.1 Tested PFMs

4.1.1 Tungsten

The test components consisted of tungsten tiles of 12 × 12 × 5 mm^3 brazed to an actively cooled copper block (section 3.1). The tungsten tiles were cut from a disc shaped block of pure (99.97 wt%) tungsten provided by Plansee AG, Austria (fig. 4.1). It was produced by cold isostatic pressing of homogenised powder, sub-

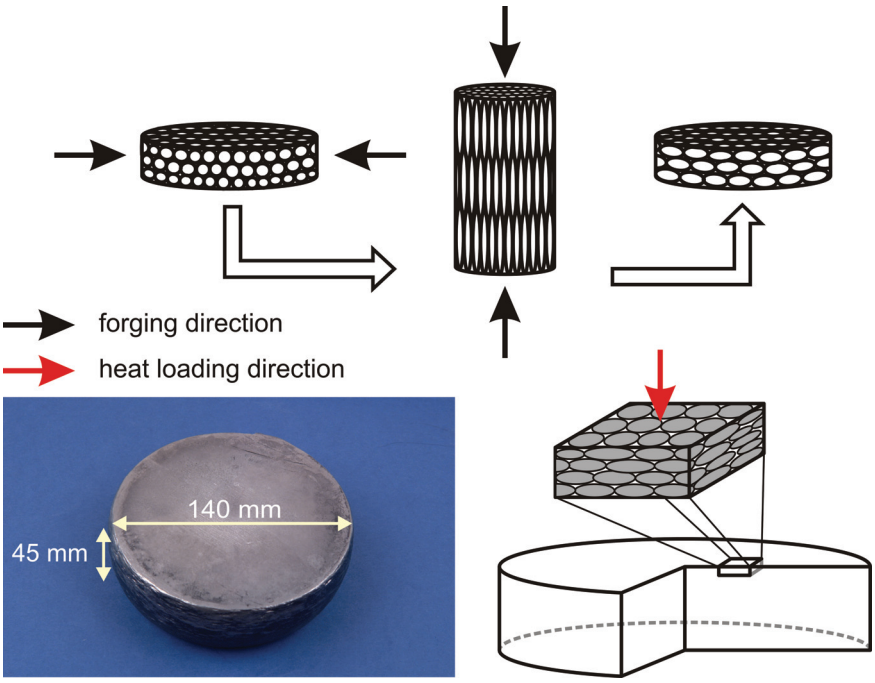

Figure 4.1: Pure double forged tungsten disc as provided by Plansee AG, Austria. Forging steps, cutting scheme and grain orientation of tiles are shown.

sequent sintering at 2000 – 2500 °C and forging into a rod. A second forging step in axial direction ensued, with intent to create an isotropic material. At last the disk was annealed at 1000 °C for stress relieving. Despite the intention to create an isotropic material, microstructural investigations showed that the grains of the material were disc shaped (following the shape of the block) with an aspect ratio of ≈ 0.4 [62]. The grains were oriented parallel to the loaded surface, which was always polished to mirror finish (with diamond suspension of 1 µm; done before brazing to the cooling structure) to assure well-defined starting conditions. Profilometry scans on polished surfaces showed a mean roughness of about $R_a \approx 0.1$ µm (before and after brazing). Typically deviations from zero line were ≤ 1 µm. These irregularities were related to the texture: grains of different crystallographic orientations have different mechanical properties in surface plane direction, hence some grains are more prone to material removal by polishing with the diamond suspension than others. This leads to hills and valleys which are visible in light microscope images (fig. 4.2).

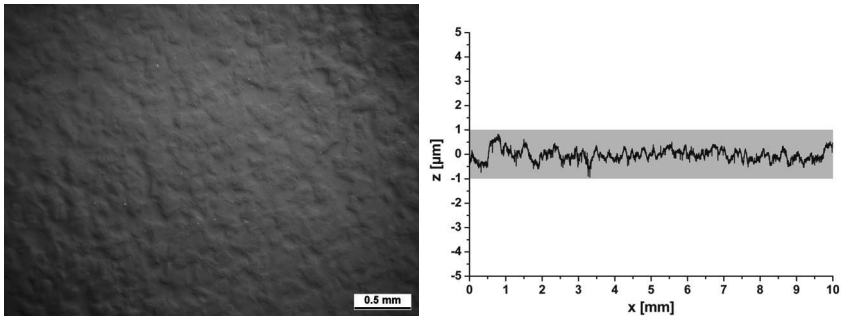

Figure 4.2: Light microscope image of polished tungsten and corresponding profilometry result as it appears before testing. A special lighting shows the roughness that remained after polishing. This texture occurs due to the different mechanical properties of differently oriented grains. Surface average roughness is typically $R_a = 0.05$ – 0.12 µm. Maximum valley/peak depth/height is typically 0.5 – 1 µm.

4.1.2 CFC

The test components consisted of NB31 and NB41 CFC tiles of $12 \times 12 \times 5$ mm^3 brazed to an actively cooled copper block (section 3.1). Both CFC types are made of carbon fibre bundles aligned in orthogonal directions as shown in figure 4.3. The pitch fibres, aligned perpendicular to the surface, have the highest thermal conductivity in fibre direction. The PAN (polyacrylonitrile) fibres are aligned parallel to the surface. These fibre bundles are used to achieve high tensile strength. The bundles in z-direction are produced by using a hook-like tool to pull out fibres from

the PAN bundles, perpendicular to PAN and pitch direction. This process is called needling. The whole production process of carbon composites is described in detail in [63], investigations of material properties and thermal shock behaviour in [64–67]. The tiles used for the experiments were polished like the tungsten tiles, but due to the porous nature of CFC the surface is never as plain as the tungsten surfaces.

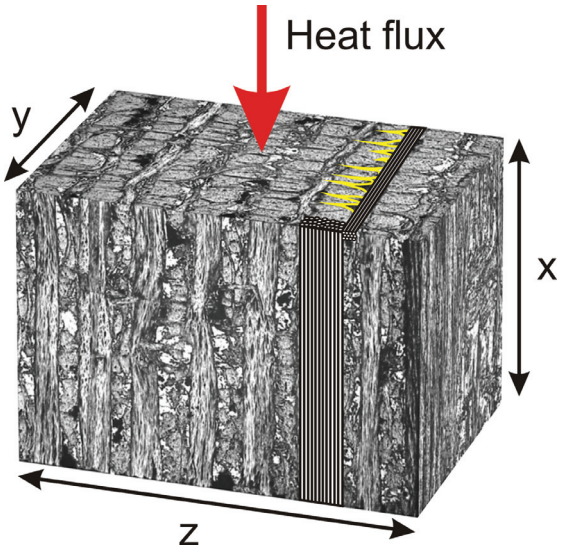

Figure 4.3: CFC NB31 material block and its different fibre bundles: pitch fibres in x-direction, PAN fibres in y-direction and needled PAN fibres in z-direction (yellow).

4.2 Experimental conditions

For the experiments the components were mounted in JUDITH 2 and connected to the cooling circuit. Water was used as coolant with a temperature of 100 °C (meaning this was also the starting component temperature for all tests). At this temperature the heat transfer coefficient is high and hence a better cooling efficiency is achieved compared to cold water cooling. Water pressure was 3 MPa (30 bar) with a flow rate of 100 l/min. Pressure and temperature were close to the ITER cooling system parameters [32].

A pulse frequency of 25 Hz and a pulse duration of 0.48 ms were kept constant for all experiments. The electron absorption coefficient used to calculate the absorbed power density was assumed to be 0.55 for tungsten and 0.97 for carbon and was obtained by Monte-Carlo simulation for pure tungsten/carbon [49]. The circular beam loading method with the aforementioned radii (section 3.4, table 3.1) was always used.

All tests performed are shown in table 4.1. In general, surface temperatures depend on SSHL (0 – 10 MWm^{-2}), PFM, component geometry, cooling, and beam width to tile size ratio. The values given in table 4.1 are nominal values which represent the true temperature. The real surface temperatures can deviate by a few ten degrees and were obtained by finite element simulations (sections 2.4, 4.3 and 5.1) and, if above 350 °C, verified by pyrometer measurements (section 2.2 & 5.1). These temperatures were reached a few seconds after the start of an experiment (situation of equilibrium with the cooling, fig. 5.5).

Experiments were interrupted after every 10,000 pulses ($\hat{=}$ 400 s) for 10 s, resembling an ITER discharge. The component cooled down to starting temperature (100 °C) during this time.

Table 4.1: Test matrix. Every test that was performed is indicated by an ⊗. A frequency of 25 Hz was always used. Energy density H_{abs}, power density L_{abs} and heat flux factor F_{HF} are proportional to each other because the pulse duration is constant ($\Delta t = 0.48$ ms).

	Tungsten											CFC		
T_{surf} (°C)[1]			200			400		700				450		
SSHL (MWm^{-2})			0			5		10				10		
H_{abs} (MJm^{-2})	0.07	0.13	0.16	0.19	0.26	0.13	0.19	0.07	0.13	0.19	0.26	0.19	0.26	0.33
L_{abs} (GWm^{-2})	0.14	0.27	0.34	0.41	0.55	0.27	0.41	0.14	0.27	0.41	0.55	0.41	0.55	0.68
F_{HF} ($MWm^{-2}s^{0.5}$)	3	6	7.5	9	12	6	9	3	6	9	12	9	12	15
10^3 pulses			⊗	⊗	⊗		⊗			⊗	⊗	⊗[2]		
10^4 pulses		⊗		⊗	⊗	⊗	⊗		⊗	⊗	⊗	⊗[2]	⊗[3]	⊗[3]
10^5 pulses		⊗		⊗	⊗	⊗	⊗	⊗	⊗	⊗	⊗	⊗[2]		⊗[3]
$2.5 \cdot 10^5$ pulses	⊗	⊗												
10^6 pulses		⊗						⊗						

[1]Nominal temperature, exact values depend on loading conditions (section 5.1) [2]NB31 [3]NB41

4.3 Temperature simulations

As the sample geometry was changing during development of the test procedure, a script file with a parametrised geometry was written. A set of parameters like tile dimensions, cooling tube radius or tile distance has to be provided, everything else is calculated automatically. As the electron beam of JUDITH 2 can be focussed on different spots via x– and y–coordinates, the script was designed to accept coordinate files (in millimetres, not in machine coordinates, but the Beambam software provides a conversion based on the linear dependence given in [1]) and apply the loads. The Gaussian shape of the beam (section 3.2) is used when applying heat loads, so the beam diameter (σ) and centre power density (L_0, equation 3.1 in section 3.2) has to be given. Material properties were taken from the ITER materials database [68] for tungsten and from [66] and [69] for CFC NB31 and NB41 respectively. The data set available for NB31 contained separate data for PAN and pitch fibres, hence the individual fibre bundles could be simulated (with perfect thermal contact between them).

Temperature dependent heat transfer coefficients for the active cooling were calculated with the EUPITER code [70] for the given experimental conditions (previous section). The heat transfer coefficient increases with increasing coolant temperature, at least up to 320 °C. However, as the cooling is very efficient, temperatures that high are not achieved, hence simulation results showed differences of only $\lesssim 1\,°C$ when using a fixed (100 °C, temperature independent) heat transfer coefficient.

In all simulations radiative cooling was omitted (to save calculation time) because it does not contribute significantly to the heat balance for the given situation. The highest temperatures, achieved during a THL, were about $T_{surf} \approx 1400\,°C$. Using the Stefan–Boltzmann law

$$j^* = \epsilon \sigma_{SB} T^4 \tag{4.1}$$

an emissive power density of $j^* \approx 0.44$ MWm^{-2} can be estimated ($\sigma_{SB} = 5.6704 \cdot 10^{-8}$ Wm^{-2}K^{-4}), assuming a "worst case" emissivity of $\epsilon = 1$ and neglecting the emission of the surrounding machine (which is cooled to room temperature). This is three orders of magnitude smaller than the heating power density. During interpulse time the surface temperature reaches $T_{surf} \approx 700\,°C$ at most and hence radiates with $j^* = 0.05$ MWm^{-2}, which is $1/200^{th}$ of the SSHL power density (or less for $\epsilon < 1$).

Perfect heat conduction through the brazing interface was also an assumption in all simulations. The brazing of tungsten and copper with a silver based solder showed excellent wetting and only rarely cavities (fig. 3.3). Additionally silver has an extremely high thermal conductivity, compensating small defects in the brazing layer [58]. However, the assumption of a negligible influence of the joint is only valid for thermal calculations as performed here, not for mechanical.

First simulations were done with the full implementation of every 5 µs spot of the circular beam loading. One THL consists of 96 steps (8 spots, repeated 12 times), plus the interpulse time until the next pulse. This procedure was changed, because

it was too time consuming, by replacing the energy intake of the 96 (Gaussian) 5 µs pulses with a single Gaussian. This "virtual" Gaussian beam is formed when adding the intake of all single spots:

$$\begin{aligned} H_{virt} &= L_{abs}^{bc} \cdot N_{rep} \cdot \Delta t_{sp} \cdot \sum_{i=1}^{n_{sp}} e^{-\frac{\left(x+r_{circ}\cdot\cos\left(i\cdot\frac{360}{n_{sp}}\right)\right)^2+\left(y+r_{circ}\cdot\sin\left(i\cdot\frac{360}{n_{sp}}\right)\right)^2}{2\sigma^2}} \\ &\overset{r_{circ}<\sigma}{\approx} L_{abs}^{cc} \cdot \Delta t \cdot e^{-\frac{x^2+y^2}{2\sigma^{*2}}} \end{aligned} \tag{4.2}$$

A circle with a radius of r_{circ} consisted of $n_{sp} = 8$ spots which were repeated $N_{rep} = 12$ times. Actually the sum does not result in a Gaussian, as can easily be seen when increasing the distance r_{circ} of the individual Gauss functions, but for distances $r_{circ}<\sigma$ it is approximated well by a Gaussian. The "virtual" Gaussian has the width σ^* of H_{virt} and the centre power density L_{abs}^{cc} (table 3.1). This replacement technique allowed to perform simulations of the first four seconds of an experiment in a reasonable time. After this time the dynamic equilibrium between heating and cooling was reached.

The complete simulation script is found in appendix A.

5 Results and discussion

5.1 Temperature measurements and simulation results

Successful surface temperature measurements with the fast pyrometer for experiments with 10 MWm^{-2} SSHL and 5 MWm^{-2} SSHL are shown in figures 5.1 and 5.2 respectively. An emissivity value of $\epsilon_W = 0.2$ was used for all measurements on tungsten. This value was chosen using the base surface temperature provided by the two colour pyrometer as calibration point.

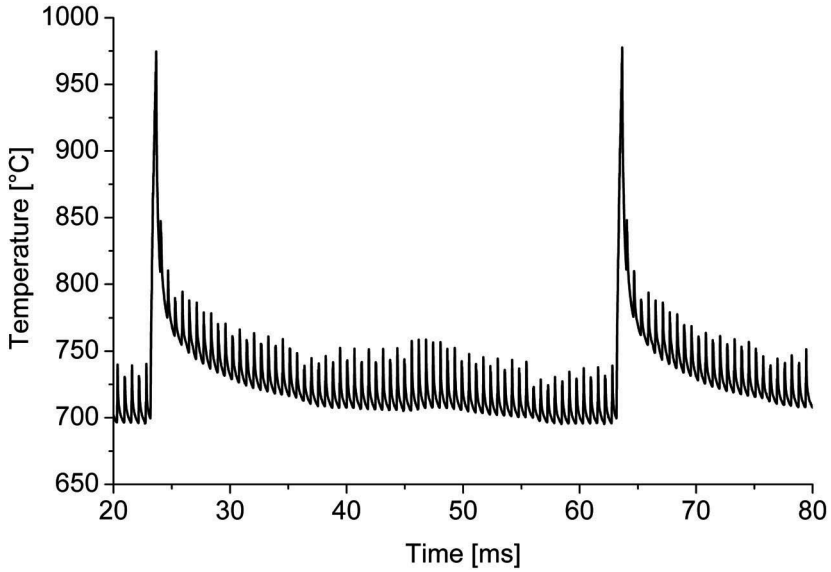

Figure 5.1: Temperature measurement with the fast single colour pyrometer on tungsten ($\epsilon_W = 0.2$). The experiment applied THLs of 0.55 GWm^{-2} and a SSHL of 10 MWm^{-2}. This led to a base temperature of $\approx 700\,°C$. The impact of the ELM–like pulses (every 40 ms) is clearly visible, as well as the 64 small spikes (per cycle) caused by the electron beam sweeping that provides the SSHL.

The results clearly showed that the loading patterns were applied correctly by the machine. Two main features of the temperature graph were visible: first, a temperature leap of several hundred degrees Celsius ($dT/dt \approx 10^6$ Ks^{-1}) caused by the induced THL. One should note that the peak temperature value is inaccurate, because of emissivity changes during temperature rise, and, more important, because an exact overlap of loaded area and pyrometer spot could not be guaranteed. However, the purpose of the measurement was to check the temperature development and to compare the base temperature with the simulation predictions.

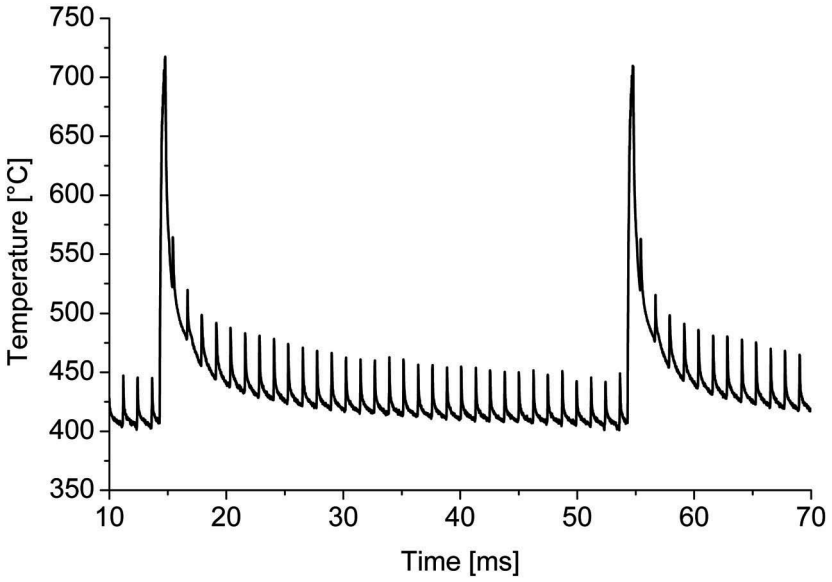

Figure 5.2: Temperature measurement with the fast single colour pyrometer on tungsten ($\epsilon_W = 0.2$). The experiment applied THLs of 0.41 GWm^{-2} and a SSHL of 5 MWm^{-2}. This led to a base temperature of $\approx 400\,°C$. The impact of the ELM–like pulses (every 40 ms) is clearly visible, as well as the 32 small spikes (per cycle) caused by the electron beam sweeping that provides the SSHL.

Second, the cool down phase (interpulse time), was superimposed by small peaks that were caused by the electron beam sweeping. Sweeping provided the SSHL and was applied by a complex beam guidance pattern (section 3.6). The number of small spikes corresponds to the number of times the beam should switch between the two beam dumps, loading the tile. Checking the distance of the THL leaps showed the correct application of one ELM–like load every 40 ms (25 Hz). This is of importance because the number of applied pulses is calculated by multiplying the frequency with the duration of the experiment. The measurement shows that the guidance software takes the time into account that the beam needs to travel from

one spot to the next. Otherwise the time between successive transient loads would have been more than 40 ms (i.e. not taking into account a travelling time of only 0.5 µs between successive spots would lead to ≈ 4 ms delay).

The surface temperature reaches ≈ 700 °C and ≈ 400 °C for the two cases of 10 and 5 MWm^{-2} respectively (fig. 5.1, fig. 5.2). The overall energy intake is also influenced by the THL intensity. Especially if the beam is broad compared to the tile width losses become important (fig. 3.5). Experiments with $F_{HF} = 3\ MWm^{-2}s^{0.5}$ (beam FWHM ≈ 12 mm) have significant losses. The computed average load intake of the 12 × 12 mm^2 tungsten tile surface by these transients was ≈ 1.1 MWm^{-2} while it was about 1.6 – 1.8 MWm^{-2} for experiments with higher F_{HF} value.

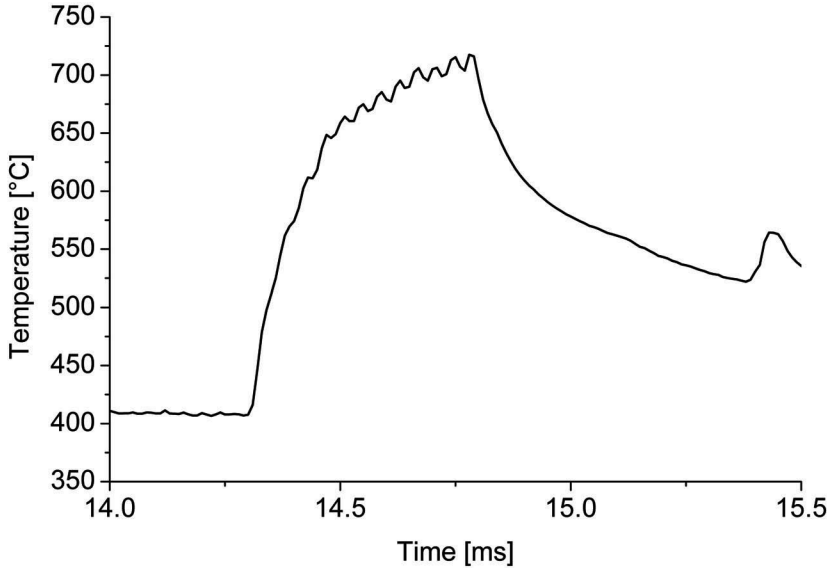

Figure 5.3: Temperature measurement with the fast single colour pyrometer showing the temperature rise during a THL (detail of fig. 5.2). The bumps are a result of the circular loading while observing a spot next to the circle centre (compare with loading, fig. 3.14).

A detail of figure 5.2 is shown in figure 5.3, magnifying the temperature leap caused by the THL. The circular loading became apparent in this measurement as every circling of the beam is visible as small bump (12 in total). The loaded area and the pyrometer spot did not overlap perfectly and the temperature was measured some fractions of a millimetre apart from the loading centre (otherwise the bumps would not be visible).

Pyrometer measurements were also done during the tests on CFC. An emissivity value of $\epsilon_{CFC} = 0.9$ was used, again calibrated with the two colour pyrometer. Although the SSHL was 10 MWm^{-2}, the base temperature was only about

$T_{surf} \approx 500\,°C$ due to the excellent thermal conductivity of CFC.

The measured temperatures correspond well to the predictions made by the FEM simulations. Figure 5.5 shows the surface temperature development for a component loaded with the most severe thermal loads (10 MWm^{-2} SSHL and THL of $F_{HF} = 12\ MWm^{-2}s^{0.5}$) on tungsten. An equilibrium temperature of $T_{surf} \approx 700\,°C$

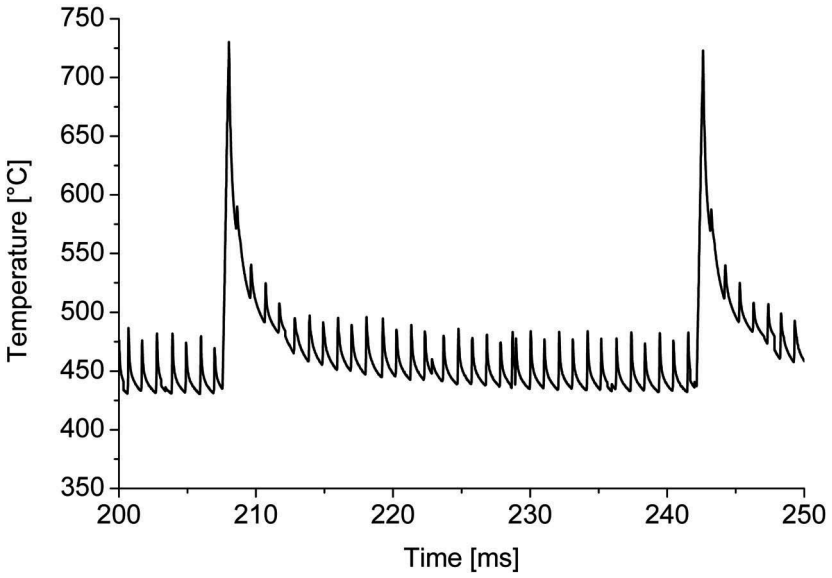

Figure 5.4: Temperature measurement with the fast single colour pyrometer on CFC NB31 ($\epsilon_{CFC} = 0.9$). The experiment applied THLs of 0.41 GWm^{-2} and a SSHL of 10 MWm^{-2}. This led to a base temperature of $\approx 500\,°C$. The impact of the ELM–like pulses (every 40 ms) is clearly visible, as well as the small spikes caused by the electron beam sweeping that provides the SSHL.

and peak temperatures of $T_{peak} \approx 1400\,°C$ were achieved after 4 seconds ($\hat{=}$ 100 pulses). The temperature at the joint between tungsten and copper was $< 300\,°C$ and the gradient from surface to cooling tube inner wall was $< 100\,°C/mm$. The temperature predictions for CFC did not correspond to the measurements as well as for tungsten: A higher base temperature of $T_{surf} \approx 500\,°C$ was expected (fig. 5.10). The difference may be attributed to an actually lower emissivity (however, this should not contribute more than a few percent) and to the fact that the pyrometer gives an average value of pitch and PAN fibre temperatures. However, the volumetric heating effect due to the high electron penetration depth has probably the strongest impact (section 2.1). In the simulations a pure surface load is assumed.

Figures 5.7, 5.8 and 5.10 show the simulated base and peak surface temperatures for all conditions. The base temperature is lowest for $F_{HF} = 3\ MWm^{-2}s^{0.5}$ on tungsten, the case with the highest losses because of the large beam diameter. In order to

facilitate the description of results, nominal temperatures of $T_{surf} \approx 200\,°C$, 400 °C and 700 °C are used for tungsten and $T_{surf} \approx 500\,°C$ is used for CFC, representing the different SSHL steps.

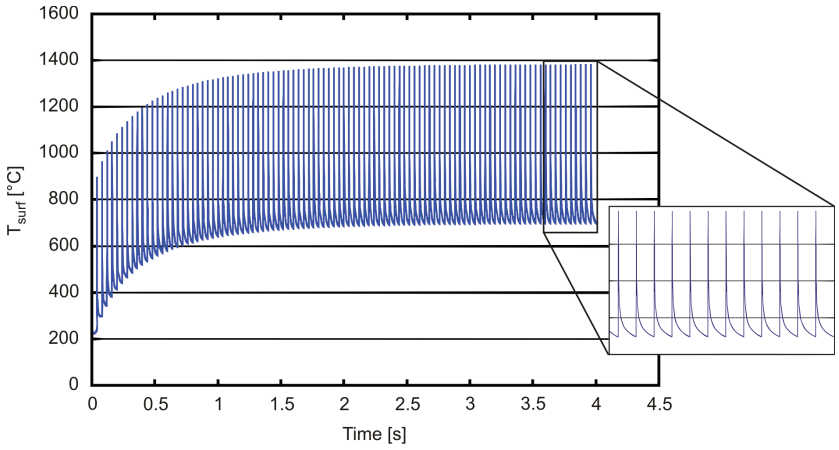

Figure 5.5: Surface temperature at the centre of a tungsten tile exposed to THL pulses of $F_{HF} = 12\ MWm^{-2}s^{0.5}$ and an additional SSHL of 10 MWm^{-2}. After 4 seconds an equilibrium with the cooling is achieved, resulting in a base surface temperature of $T_{surf} \approx 700$ °C and peak temperatures of $T_{peak} \approx 1400$ °C. Conditions apply as described in section 4.3.

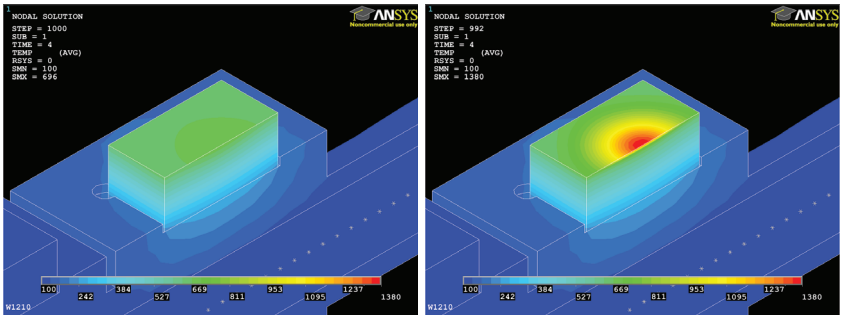

Figure 5.6: Temperature distribution for a tungsten tile exposed to THL pulses of $F_{HF} = 12\ MWm^{-2}s^{0.5}$ and an additional SSHL of 10 MWm^{-2} after 4 seconds. The images show the moment immediately before (left) and after (right) a THL pulse.

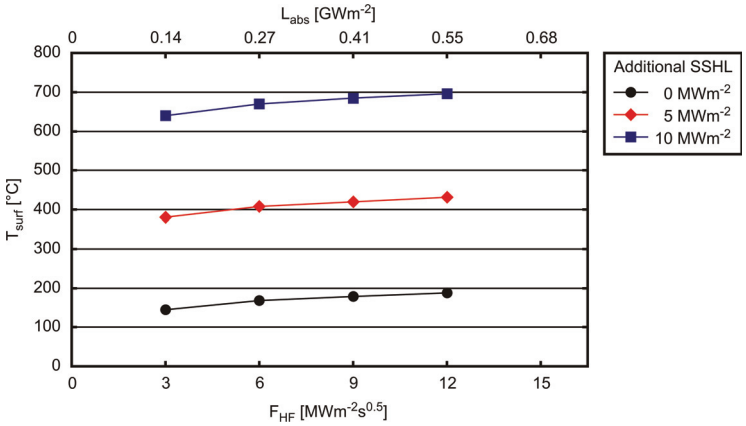

Figure 5.7: Simulation results for the base surface temperature of tungsten tiles exposed to different THL pulses (x-axis) and additional SSHLs.

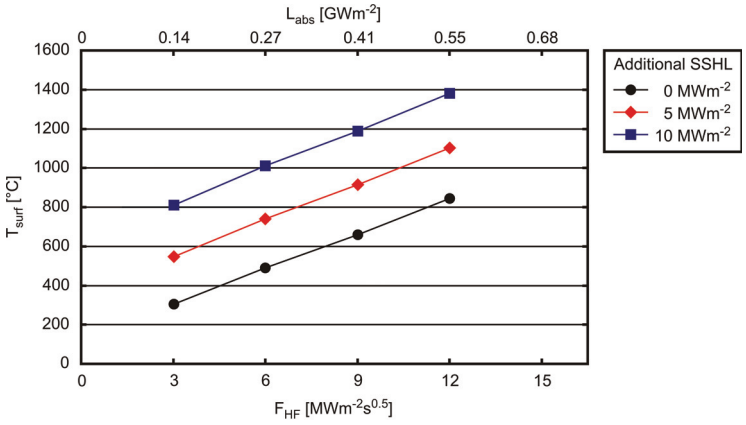

Figure 5.8: Simulation results for the peak surface temperature of tungsten tiles exposed to different THL pulses (x-axis) and additional SSHLs.

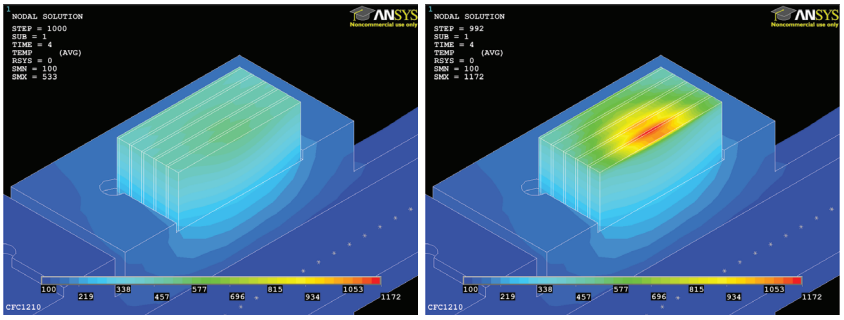

Figure 5.9: Temperature distribution for a NB31 CFC tile exposed to THL pulses of $F_{HF} = 12\ MWm^{-2}s^{0.5}$ and an additional SSHL of 10 MWm^{-2} after 4 seconds. The images show the moment immediately before (left) and after (right) a THL pulse. The PAN fibres are hotter than the pitch fibres because of their worse thermal conductivity (in depth, towards the cooling).

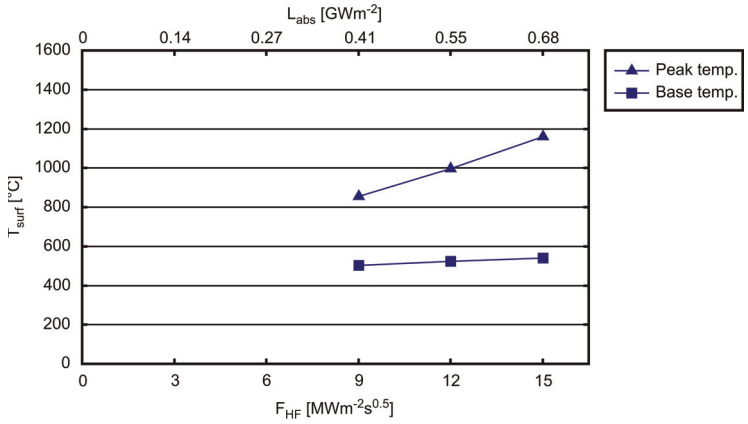

Figure 5.10: Simulation results for the peak and base surface temperature of NB31 CFC tiles exposed to different THL pulses (x-axis) and an additional SSHL of 10 MWm^{-2}. The axis scaling is the same as in figure 5.8. The results for NB41 CFC are not shown because they differ only by 1 – 4 % from the NB31 values.

5.2 Tungsten

5.2.1 Overview

The double forged tungsten tiles were exposed to 10 – 10^6 THL pulses of F_{HF} = 3 – 12 $MWm^{-2}s^{0.5}$ at surface temperatures of about 200 °C, 400 °C and 700 °C. The names used for the samples are composed of two (no SSHL) or three (with SSHL) parts: The first part refers to the heat flux factor in $MWm^{-2}s^{0.5}$ with which the sample was loaded. It has two digits always. The last part carries the information about the number of cycles in scientific notation. If a SSHL was used, it is noted in the middle (in MWm^{-2}), also always with two digits. A sample loaded with 250 000 pulses of F_{HF} = 6 $MWm^{-2}s^{0.5}$ and a SSHL of 5 MWm^{-2} would be named 06052.5E5.

$$\underbrace{06}_{\substack{F_{HF}\\(MWm^{-2}s^{0.5})}}\ \underbrace{05}_{\substack{SSHL\\(MWm^{-2})}}\ \underbrace{2.5E5}_{\text{number of pulses}}$$

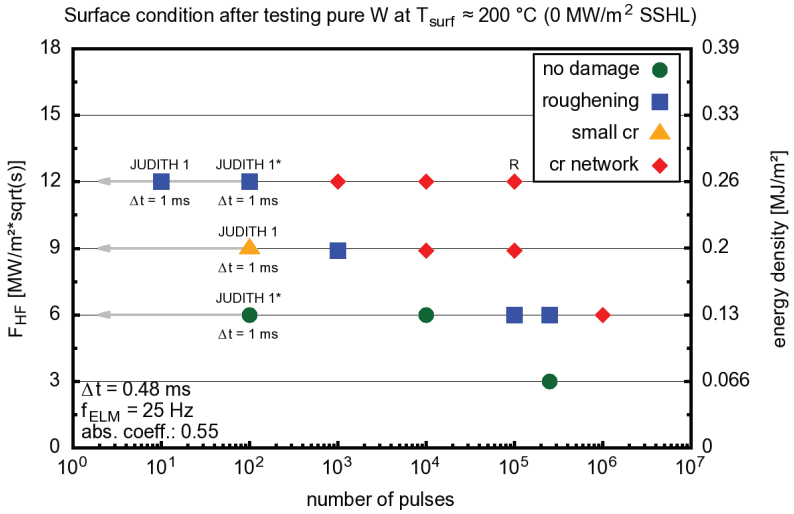

Figure 5.11: Surface condition of tungsten samples tested at a surface temperature of ≈ 200 °C (no SSHL). Undamaged samples are represented by a green dot, roughened samples by a blue rectangle, samples with small unconnected cracks by an orange triangle and samples with a crack network by a red diamond. One sample showed recrystallisation at the surface near a crack (indicated by "R"). Samples tested in JUDITH 1 are labelled accordingly, samples indicated by an asterisk were added according to [62].

After exposure, samples were examined by light microscope, SEM and laser profilometry as well as by metallographic investigation of the cross section of the

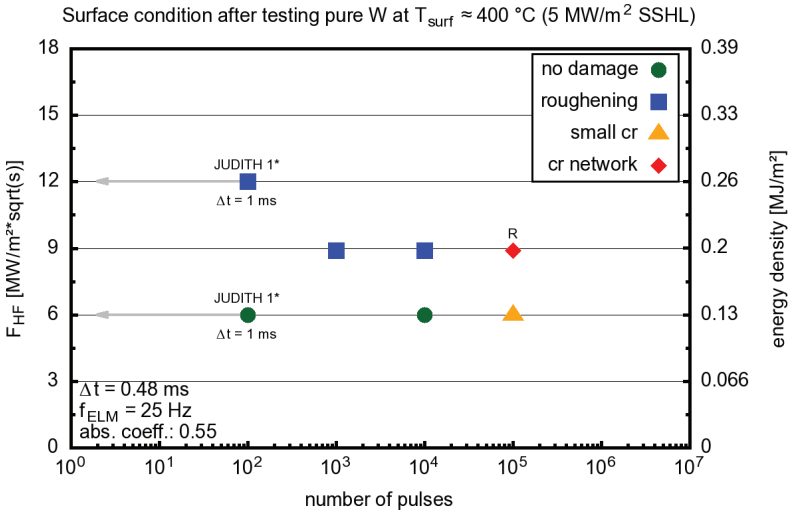

Figure 5.12: Surface condition of tungsten samples tested at a surface temperature of ≈ 400 °C (5 MWm^{-2} SSHL). One sample was cross sectioned and showed recrystallisation, indicated by "R". Samples tested in JUDITH 1 are labelled accordingly, samples indicated by an asterisk were added according to [62].

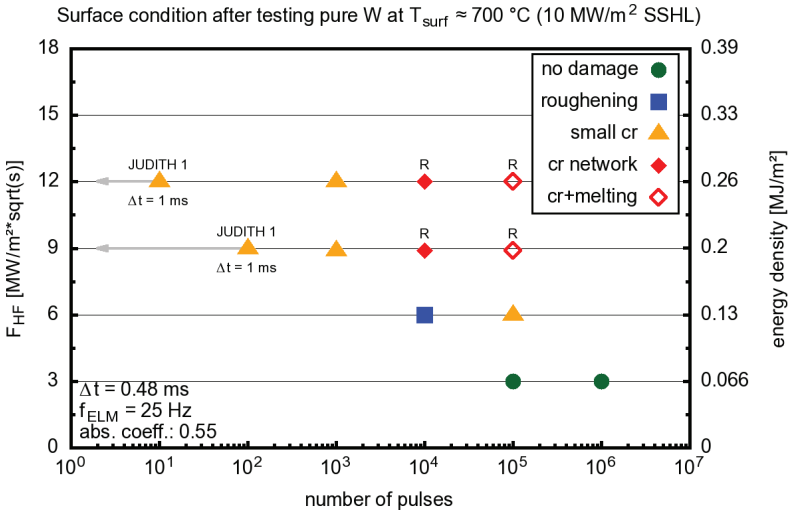

Figure 5.13: Surface condition of tungsten samples tested at a surface temperature of ≈ 700 °C (10 MWm^{-2} SSHL). Samples that were cross sectioned and showed recrystallisation are indicated by "R". Samples tested in JUDITH 1 are labelled accordingly.

specimens. The damage was categorised according to the type of observed degradation. Overview graphs show the results of different experiments (fig. 5.11 – 5.13). Roughened samples show a change in reflectivity visible at optical inspection and on light microscope images (fig. 5.15). This change could be identified as roughening by using laser profilometry. Cracks appear with increasing cycle number/power density ("small cracks", fig. 5.22a) and connect to a "crack network" (fig. 5.22b). Small cracks were only observed at elevated temperatures ($T_{surf} \approx 400\,°C$ and $700\,°C$). After further pulses also melting took place for the most severely loaded samples (fig. 5.22c,d).

These categories are rather rough as only few samples showed similar damage. Hence, in some cases the categories did not fit as well as in others. Sample 121E3 (1000 pulses of $F_{HF} = 12\ MWm^{-2}s^{0.5}$, $T_{surf} = 200\,°C$, fig. 5.17) showed mainly roughening, but one single multiply branched crack at the fringe of the loaded area. It had to be classified as "cracked" although it is quite different from other cracked samples. Some samples are therefore discussed in more detail, like 121E3.

A few selected samples were tested in the JUDITH 1 facility (low pulse number tests). They are also shown in the overview diagrams as a supplement. Because of the minimum pulse duration of 1 ms they can, however, not be compared using the power or energy density, but the heat flux factor. Samples loaded in JUDITH 1 always showed a stronger degradation than samples loaded at similar conditions in JUDITH 2. Hence the test with 100 pulses of $F_{HF} = 9\ MWm^{-2}s^{0.5}$ at $T_{surf} = 200\,°C$ showed small cracks already, but the test at the same heat flux factor/temperature with 1000 pulses in JUDITH 2 showed only roughening. This might be attributed to the scanning mode in JUDITH 1 which is less homogeneous compared to the JUDITH 2 transient simulation method (fig. 2.2, fig. 3.14).

In contrast to typical thermal shock tests performed at higher power densities and lower pulse numbers the results showed a slow evolution of degradation. This development suggested that cracks originate from thermal fatigue. A first directly observable effect of this fatigue is roughening.

5.2.2 Roughening

Profilometry revealed that the surface generally developed a higher mean roughness $R_a \approx 0.15 – 0.3\ \mu m$, also next to the area loaded with transients (and even without SSHL). This was invisible to the naked eye, the samples were still mirroring. On LM images the surface showed a more pronounced structure than already visible before testing. This small scale waviness (wavelength ≈ grain size) seems to be an effect of the thermal expansion and contraction of the surface.

When looking at the samples after removing them from the machine, roughening of the area loaded with transients was immediately visible as dulled spot on the otherwise mirroring tungsten surface. The investigation of this roughness revealed a more pronounced roughening for higher base temperatures and pulse numbers

(higher mean roughness R_a, fig. 5.14). It also appears earlier for higher temperatures, i.e. at $F_{HF} = 6$ MWm^{-2}s$^{0.5}$ for 10^4 pulses there was no damage at $T_{surf} \approx 200\,°C$ / $400\,°C$, but roughening was observed at $T_{surf} \approx 700\,°C$. The overview of all measured R_a values (fig. 5.14) as well as the LM and SEM images showed that the roughening process continued after crack formation, leading to highly deformed surfaces (fig. 5.22d). Although increasing, the observed roughness seems to reach a saturation for $T_{surf} \approx 200\,°C$. However, the number of data points to confirm this is too small.

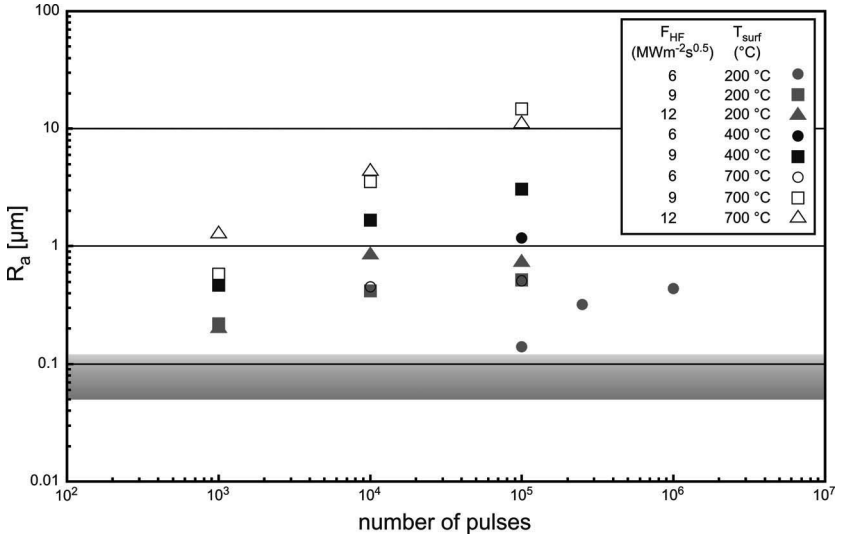

Figure 5.14: Overview of mean roughness values of the loaded areas. All samples that showed at least roughened surfaces are shown. The area highlighted in grey denotes the range of R_a values covered by unloaded (polished) samples.

In the case of sample 061E5 the roughening was for the first time found to be present on some tiny spots and did not cover the complete loaded area. This was the first indication that the roughening process proceeded faster on certain areas. The mean roughness increased from $R_a = 0.1$ µm to $R_a = 0.14$ µm, which is barely significant, but the damage was also visible in the LM images when using a special light incidence (fig. 5.15).

Samples tested after 061E5 showed: in early stages of degradation, roughening was often found to occur at preferential locations. By laser profilometry roughness with an amplitude of just a few hundred nanometres was identified for sample 121E3 (fig. 5.17). Later stages of roughening had amplitudes up to > 20 µm. The observed localised roughened spots on some samples were analysed by using Electron Backscatter Diffraction (EBSD) on the surface of the sample shown in figure 5.17. Despite the roughening, the surface was flat enough to allow the usage of the EBSD

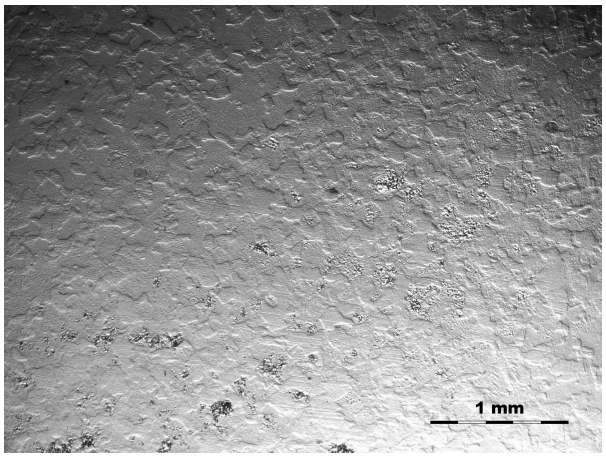

Figure 5.15: LM top view image of the tungsten sample 061E5 after loading. Just a few spots showed some roughening. This was the sample with the slightest traces of surface modification (regarding the R_a value) of all tested samples.

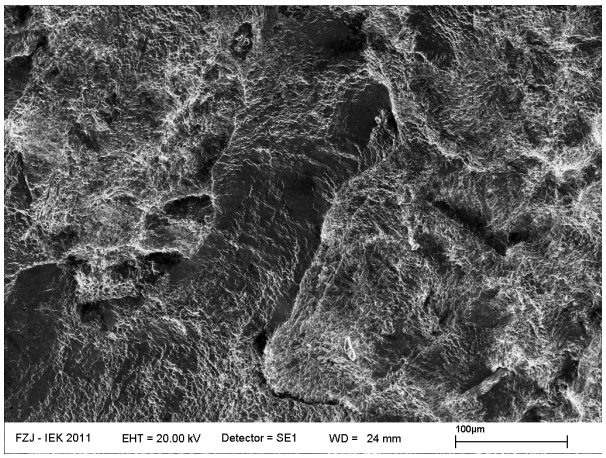

Figure 5.16: Surface SEM image of the tungsten sample 09051E4. The sample showed the strongest roughening of all (only) roughened samples. The mean roughness in the loaded area was $R_a = 1.67$ µm compared to $R_a = 0.19$ µm for the unloaded area.

technique. Figure 5.19 shows three colour coded maps of the surface area. The colours describe the orientation of lattice planes with respect to the surface normal and to the other two spatial directions indicated on the SEM picture of the same area (rolling and transverse). The roughened spots coincided with grains whose [001] direction was parallel to the surface. This grain orientation has a lower yield strength

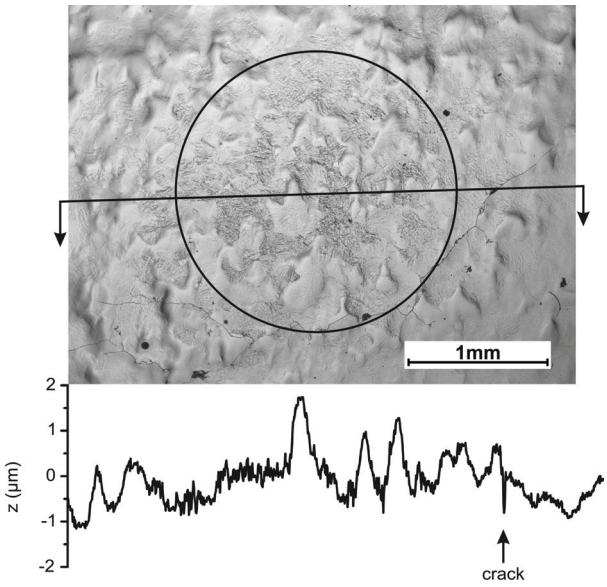

Figure 5.17: Surface LM image and laser profilometry line scan of the tungsten sample 121E3. The circle roughly indicates the loaded area. The line corresponds to the profilometry scan at the bottom. A crack is visible, but the sample is mainly roughened. The roughening is limited to certain spots.

in surface plane direction and, therefore, starts to deform first. The difference in yield strength comparing the stronger [011] and the weaker [001] direction is about a factor of two for a temperature range of 77 K – ≈ 423 K (fig. 5.18). The weaker

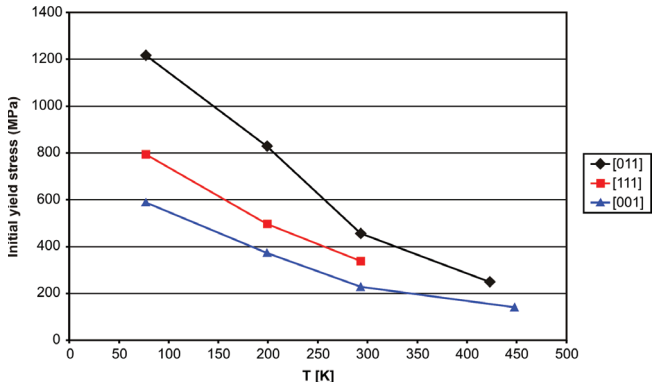

Figure 5.18: Initial yield stress of different crystallographic orientations of tungsten depending on temperature, according to [16].

grains are also more prone to material removal due to polishing, which explains

why they lay deeper (texture in figure 5.17, also visible on unloaded surfaces before experiments, fig. 4.2). A higher homogeneity in surface roughening was observed at higher temperatures (fig. 5.16), either because of higher stresses or because of a vanishing difference of yield strength of the crystallographic orientations at higher temperatures.

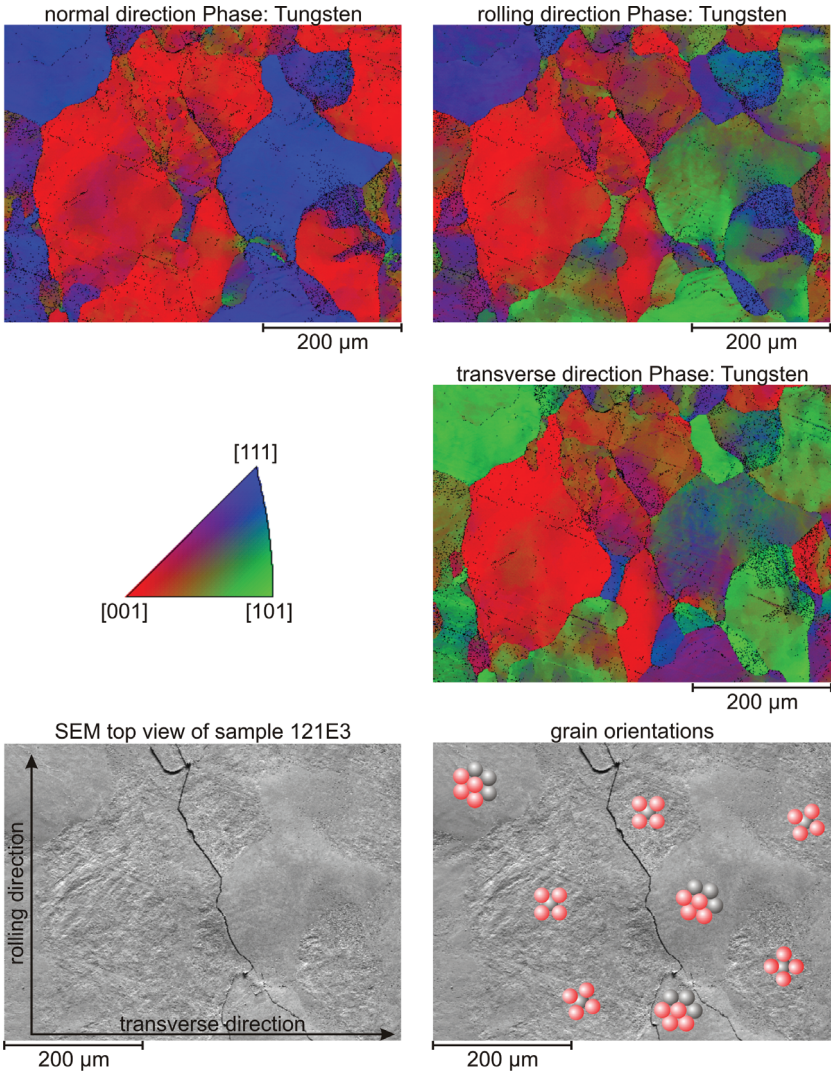

Figure 5.19: EBSD investigation of the tungsten sample 121E3. The roughened areas are coextensive with the grains whose [001] direction is parallel to the surface. This crystallographic direction has a lower yield strength in surface plane direction [16].

5.2.3 Cracking and melting

Cracks appeared when applying a high pulse number ($> 10^4$) for $F_{HF} > 6$ MWm^{-2}s$^{0.5}$ or when increasing the power density above a certain limit at a given pulse number. At $T_{surf} \approx 200$ °C the threshold strongly depended on the pulse intensity: between 10^2 and 10^3 pulses for $F_{HF} = 12$ MWm^{-2}s$^{0.5}$ (if the data from [62] are taken into account using the same heat flux factor), between 10^3 and 10^4 for $F_{HF} = 9$ MWm^{-2}s$^{0.5}$ and between $2.5 \cdot 10^5$ and 10^6 for $F_{HF} = 6$ MWm^{-2}s$^{0.5}$ (fig. 5.11). Experiments at $T_{surf} \approx 400$ °C (fig. 5.12) show a lower threshold at $F_{HF} = 6$ MWm^{-2}s$^{0.5}$ (10^4 – 10^5) but a higher threshold for $F_{HF} = 9$ MWm^{-2}s$^{0.5}$ (10^4 – 10^5). This behaviour is discussed further down, but may also be explained by a statistical deviation. The sample in question (09051E4) is the most severely roughened of all non–cracked samples (fig. 5.16). For the highest base temperature $T_{surf} \approx 700$ °C the thresholds are about one order of magnitude lower than for $T_{surf} \approx 200$ °C.

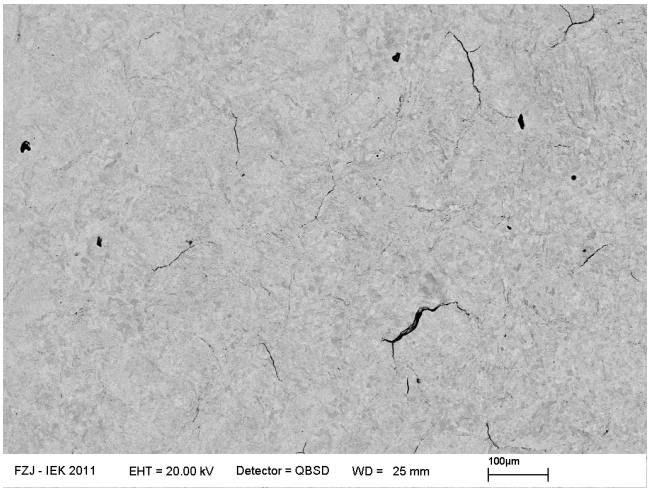

Figure 5.20: SEM image of the surface of sample 09101E3 showing the "small cracks" phase. The sample was loaded with 10^3 pulses of $F_{HF} = 9$ MWm^{-2}s$^{0.5}$ at $T_{surf} \approx 700$ °C. The cracks were straight or often also star–shaped with three branches. They were not connected with each other. A BSE image was chosen here because it provides a better contrast than a SE image.

In case of $T_{surf} \approx 200$ °C cracks typically appeared more sudden than at elevated temperatures, because the material appeared to be still fully or partially in a brittle state. This and the crack depth data discussed below indicated a fast crack development once they appeared, although the appearance of cracks may need $> 10^5$ pulses like in the case of $F_{HF} = 6$ MWm^{-2}s$^{0.5}$. Hence a "small cracks" phase may exist but was not observed for $T_{surf} \approx 200$ °C. Earlier experiments with the same material [62] showed that 150 – 200 °C is a critical temperature, above which the material be-

haved more ductile. An example for the "small cracks" phase is shown in figure 5.20. The cracks were small straight lines or had a star shape with three branches. These star shaped cracks indicate that the cracks often start at the intersection of the boundaries of three grains.

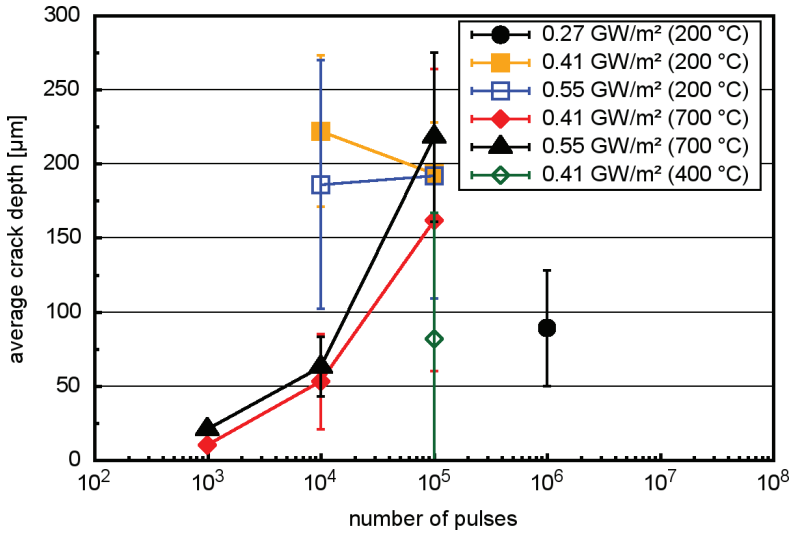

Figure 5.21: Average crack depths for different loading conditions. Typically 3 – 9 cracks were visible in a cross section.

Brittleness also explained the evolution of crack depth (fig. 5.21): It did not increase from 10^4 to 10^5 pulses at $T_{surf} \approx 200\,°C$, but did so for the exact same loading conditions at $T_{surf} \approx 700\,°C$. The crack depths at $T_{surf} \approx 700\,°C$ were significantly lower for 10^4 pulses and the first small and shallow cracks appeared already after 10^3 pulses. This suggests a development (as it was expected for fatigue cracks in a more ductile regime) instead of a sudden cracking. Investigations with lower pulse number (≤ 1000) and higher intensity showed that this development ends when the crack depth provided the necessary amount of stress relief [51]. Therefore, pulses of higher intensity created higher average crack depths. The pulse intensity determined (together with material properties) the penetration depth of the transient load and the stress amplitude. This seems to be the case here as well: The crack depth development stopped (at least for the $T_{surf} \approx 200\,°C$ case) and higher intensities led to higher crack depth. For the higher temperature case $T_{surf} \approx 700\,°C$ the same crack depth is achieved after 10^5 pulses. However, only tests at 10^6 pulses could confirm if the development stops at this depth.

The average crack depth of the sample 061E6 remained as low as ≈ 90 µm, while samples loaded with 10^5 pulses of $F_{HF} = 9\ MWm^{-2}s^{0.5}$ and $F_{HF} = 12\ MWm^{-2}s^{0.5}$ achieved average crack depths of ≈ 200 µm. The only exception (09051E5) can be explained by an extremely deep crack (≈ 300 µm) found in the sample centre. This

crack released a major fraction of the occurring stresses and thus prevented other cracks from growing. The growth of this crack was most probably facilitated by two defects in the material (cavities) it was found to cross.

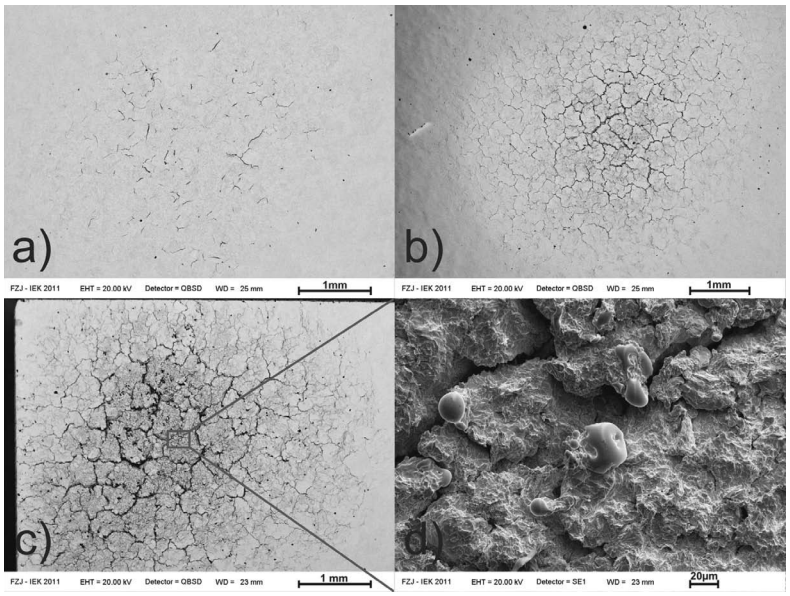

Figure 5.22: SEM images of samples loaded with 10^3 (a), 10^4 (b) and 10^5 (c) pulses of $F_{HF} = 12$ MWm^{-2}s$^{0.5}$ at $T_{surf} \approx 700$ °C. The material showed different stages of degradation: (a) small unconnected cracks, often star shaped; (b) well–marked crack network; (c) crack network + melting; the detail (d) shows the deformed surface with melt droplets, particularly on protruding parts.

In general, cracks occurred at lower pulse numbers in case of higher base temperatures (10^3 pulses with $F_{HF} = 9$ MWm^{-2}s$^{0.5}$: roughening at $T_{surf} \approx 200$ °C, cracking at $T_{surf} \approx 700$ °C). An exception was the test with 10^4 pulses at $F_{HF} = 9$ MWm^{-2}s$^{0.5}$, which showed cracking at $T_{surf} \approx 200$ °C and $T_{surf} \approx 700$ °C but only roughening at $T_{surf} \approx 400$ °C. This is explained by the ductility of the material which was high enough at 400 °C to prevent cracking up to this pulse number. At 200 °C the brittleness led to earlier cracking, while at 700 °C the lower yield stress caused a stronger deformation, hence higher fatigue damage and an early appearance of fatigue cracks.

Continued cycling after crack formation resulted in erosion of crack edges at $T_{surf} \approx 200$ °C and surface deformation at high temperatures. Erosion was observed on the sample 061E6 (fig. 5.23), in contrast to the samples loaded with 10^4 – 10^5 pulses of higher intensities. These showed a typical crack network with keen crack edges like on sample 091E5 (fig. 5.24). However, ripples were already visible at the crack edges of 091E5 as well. It can be deduced that the erosion was caused by

mechanical fatigue of prominent crack edges that repeatedly rubbed against each other at every pulse due to cyclic thermal expansion. This mechanism caused an accumulation of plastic deformation at the crack edges, which also explained the particular roughening around edges and the often observed increased height of crack edges (relative to the inter–crack areas), so called lifting. Such mechanisms were also observed in [58, 59].

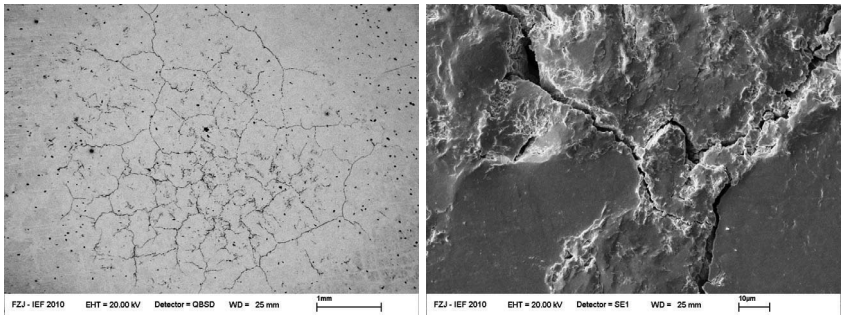

Figure 5.23: SEM images of the sample loaded with 10^6 pulses of $\mathbf{F_{HF} = 6\ MWm^{-2}s^{0.5}}$ at $\mathbf{T_{surf} \approx 200\,°C}$ (061E6). The overview on the left shows a well-marked crack network. The same loading conditions resulted only in a roughened surface after $2.5{\cdot}10^5$ pulses. Parts of the surface appear rough while others seem to be unchanged (probably "weak" and "strong" grain orientations, section 5.2.2). The detail on the right indicates the danger of erosion. Cyclic friction at the crack edges loosened small surface fragments.

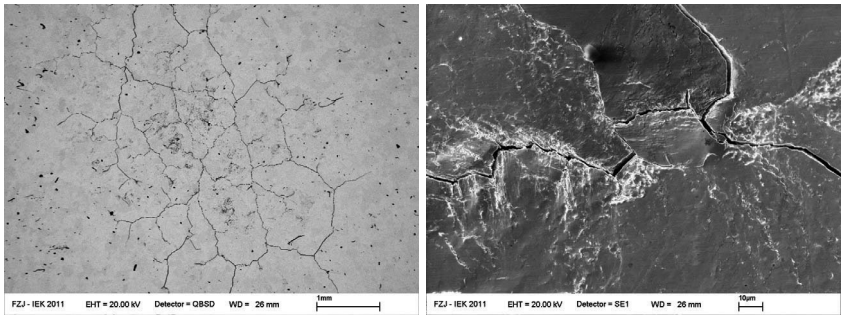

Figure 5.24: SEM images of the sample loaded with 10^5 pulses of $\mathbf{F_{HF} = 9\ MWm^{-2}s^{0.5}}$ at $\mathbf{T_{surf} \approx 200\,°C}$ (091E5). The overview on the left shows a well-marked crack network and a localised roughening typical for the $T_{surf} \approx 200\,°C$ tests. The crack edges are keen, not as eroded as for sample 061E6 (figure above). Increased roughening around the crack edges indicates the beginning fatigue due to friction.

At higher base temperatures the result is a bit different: the increased ductility

led to highly plastically deformed surfaces and (at $T_{surf} \approx 700\,°C$) to an increase in crack width. Although the crack width could not be determined precisely because the edges were not clearly defined any more (fig. 5.22d) an approximate width increase by more than one order of magnitude could be estimated (from an average $\overline{W_{cr}} \approx 2$ µm up to $\overline{W_{cr}} \gtrsim 50$ µm for the samples 091E5 ($T_{surf} \approx 200\,°C$, fig. 5.24) and 09101E5 ($T_{surf} \approx 700\,°C$, similar to fig. 5.22d), respectively).

For the most intense heat loads ($F_{HF} = 9$ MWm^{-2}s$^{0.5}$ and $F_{HF} = 12$ MWm^{-2}s$^{0.5}$) at $T_{surf} \approx 700\,°C$ some melt droplets were observed (fig. 5.22d). These originated from protruding parts which had deteriorating thermal contact, overheated and partially melted. An estimation of the amount of molten material from the SEM pictures resulted in a value of 2 – 3 gm^{-2}.

5.2.4 Recrystallisation & Recovery

Recrystallisation was found in surface near regions (20 – 300 µm depth) and around cracks (fig. 5.25). One sample even showed traces of recrystallisation close to the surface (depth ≈ 20 µm) and near to a crack at $T_{surf} \approx 200\,°C$. Maximum temperatures reached during experiments were $T_{peak} \approx 1400\,°C$, but only for a duration of ≈ 1 ms per pulse (section 5.1). This adds up to 100 seconds for a sample loaded with 10^5 pulses. Temperatures high enough to recrystallise the material are in the order of $> 1300\,°C$ (typical recommendation from the manufacturer: 1350 °C for one hour) [16,57,71,72]. This recrystallisation could have occurred due to locally diminished effective heat conductivity because of the formed cracks that act as thermal barriers. Most probably the necessary temperature is only exceeded for a short time after a transient pulse, meaning the observed phenomena were accumulating during the pulses. Furthermore the induced plastic deformation lowered the recrystallisation temperature.

Lines visible within grains in etched cross section images indicated the appearance of sub-grain boundaries, probably developed by polygonisation. This phenomenon could not be assigned to the influence of the heat load with certainty, because it was also found in the material (although scarce) before the experiment (the material was forged and subsequently stress relieved in the production process). However, the recrystallisation and polygonisation around cracks fit well to the extremely deformed zone in front of the crack tip and around the crack that is typical for fatigue cracks. The recrystallised grains had different sizes. Some appeared to be remainders of the original grain structure, others were in the process of falling apart into smaller ones and still others were completely new grains, already subjected to grain growth (fig. 5.25). The overall picture suggested a highly dynamic process where the local strain-temperature situation determined the amount of recovery, polygonisation, dynamic recrystallisation and even grain growth and melting. In comparison, the same loading conditions at $T_{surf} \approx 200\,°C$ (fig. 5.26) did not show any of these effects.

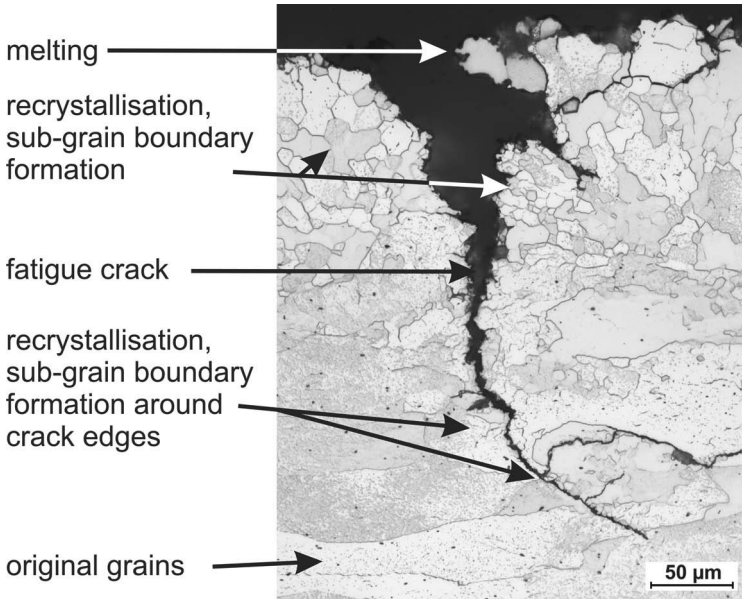

Figure 5.25: Cross section image of sample 09101E5 loaded with 10^5 pulses of $F_{HF} = 9\ MWm^{-2}s^{0.5}$ at $T_{surf} \approx 700\,°C$. Recrystallisation and sub-grain boundary appearance are visible at the top and around the crack. The original grain structure was preserved at higher depths (bottom).

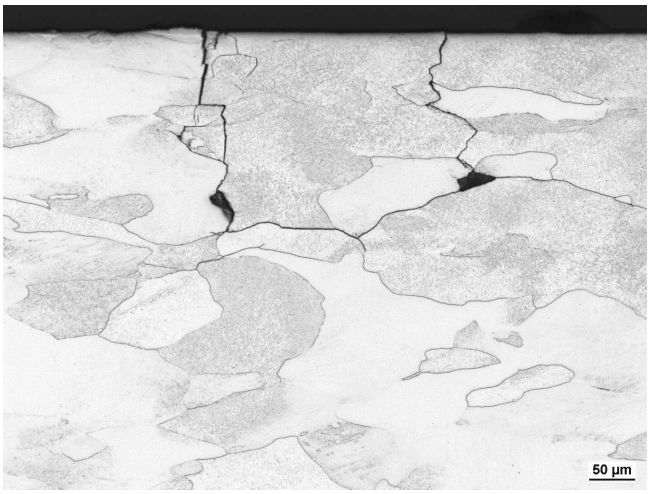

Figure 5.26: Cross section image of sample 091E5 loaded with 10^5 pulses of $F_{HF} = 9\ MWm^{-2}s^{0.5}$ at $T_{surf} \approx 200\,°C$. These conditions are the same as in figure 5.25, just at $T_{surf} \approx 200\,°C$ instead of $T_{surf} \approx 700\,°C$.

5.3 CFC

Experiments with CFC of type NB31 and NB41 showed a much higher damage threshold compared to tungsten. The results are shown in figure 5.27. First exper-

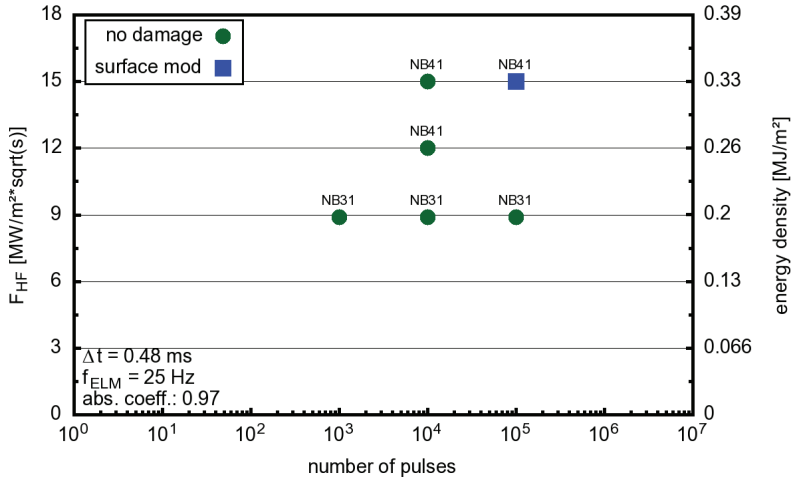

Figure 5.27: Surface condition of CFC samples tested at a surface temperature of ≈ 500 °C (10 MWm^{-2} SSHL). A surface modification has only been observed for the highest energy density and number of cycles.

iments with NB31 where planned for a heat flux factor of 9 $MWm^{-2}s^{0.5}$, because earlier experiments with the plasma facility QSPA-T (using NB31 as well) suggested a PAN fibre erosion of ≈ 0.01 µm/pulse at the corresponding energy density [73]. This would have led to a crater of ≤ 1 mm depth after 100 000 pulses. This value holds true for PAN fibre erosion, however, a shielding by the more resistant pitch fibres could result in a lower erosion depth.

In contrast to this expectation at 10^4 pulses of F_{HF} = 15 $MWm^{-2}s^{0.5}$ still no surface modification (change in reflectivity/colour) was observed. A surface modification (darkened area) at 10^5 pulses was found, but without any significant erosion (fig. 5.28).

At the corresponding energy density of 0.33 MJm^{-2} PAN fibre erosion in the order of the whole sample height was expected for 10^5 pulses, again considering [73]. Particle effects, like physical and chemical sputtering, seem to dominate CFC erosion under these conditions [20]. A threshold value for brittle destruction of 2.5 GWm^{-2} for 2 ms pulses (this corresponds to F_{HF} = 112 $MWm^{-2}s^{0.5}$) is known from electron beam experiments for the same CFC type in JUDITH 1 at low pulse numbers [40]. This means that the remaining erosion mechanisms were negligible and no long term fatigue mechanism as for tungsten occurred in CFC up to F_{HF} = 15 $MWm^{-2}s^{0.5}$.

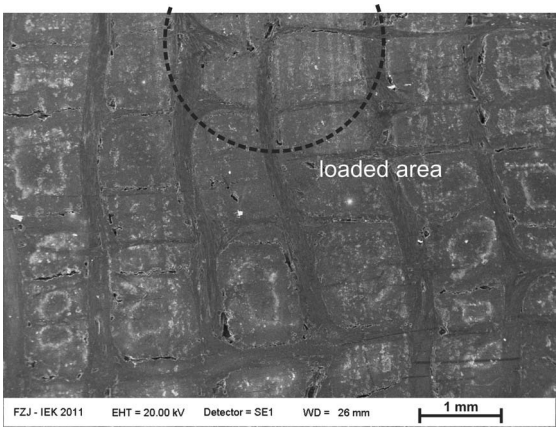

Figure 5.28: Surface image of the CFC sample loaded with 10^5 pulses of $F_{HF} = 15\ MWm^{-2}s^{0.5}$ at $T_{surf} \approx 500$ °C.

6 Conclusions

Based on the calculations, measurements and tests done for and with the electron beam test facility JUDITH 2 it can be concluded that a working test procedure for high pulse number transients could be developed. While the pulse number mainly depends on the time available for testing, the absorbed pulse power density is a more difficult issue. For tungsten up to $L_{abs} = 0.55$ GWm^{-2} was achieved and for carbon based materials or beryllium about twice as high values are possible due to the higher electron absorption. The loaded area is of the size of 3 – 12 mm^2 and would be even smaller for higher power densities. The crucial parameters for the intensity are machine power and beam diameter. A beam diameter measurement campaign done in the course of this work revealed some of the available diameter values (depending on power, acceleration voltage, vacuum quality, etc.). Increasing this database could provide parameter ranges with higher beam power densities. However, a strong increase should not be expected as higher machine power is accompanied by larger beam diameter with overall lower beam power density.

The flexible beam guidance system led to the development of tests loading samples not only with transients but also additionally and quasi simultaneously with a SSHL. This allows, in combination with previous FEM simulations, to adjust the base surface temperature. Material properties are strongly dependent on temperature, hence the response of the material to thermal loads differs with temperature. This was confirmed for the tested tungsten material by the results of this work. A technique to adjust the temperature is therefore of great value, also for application relevant test conditions, because different load intensities (and hence temperatures) are expected for different parts of the divertor in ITER and DEMO.

The observed degradation states of the tested tungsten grade show a development with number of pulses. Clearly every single pulse causes a small change in the material: the loaded area heats up and expands in contrast to the surrounding cooler material. This leads to compressive stresses that, in case of exceeding the yield strength, cause irreversible plastic deformation. This deformation could be observed, as well as its increase at higher temperature, at which the yield strength of tungsten decreases [16,57]. However, at low temperature and with weak transients the yield strength is not necessarily exceeded and cracks occur after a great number of cyclic loads analogous to mechanical fatigue.

In either case deformation/defect concentration is accumulated during cycling

and leads to increasing surface roughness and defect concentration after the cool down phase of a pulse. That finally results in first cracks starting preferentially at mechanically weak intersections of two or three grain boundaries. For samples of the category "small cracks" star-shaped cracks with three branches were often observed, which correspond to a three boundary intersection (fig. 5.20). In the case of low surface temperatures the degradation state "small cracks" was not observed. Most probably this phase is very short because cracks connect to a network faster at low temperatures. This is supported by the crack growth analyses: the cracks form more sudden and/or propagate very fast due to the higher brittleness of tungsten at lower temperatures. The pulse intensity (F_{HF}) roughly determines the final crack depth for a given material (also found for low cycle tests, [74]), while the base temperature determines the crack propagation process: Brittle and fast for low temperatures (approx. 200 °C for the examined material), ductile and slow for higher temperatures. However, cracks occur faster for hotter surfaces because of the higher ductility and hence higher fatigue due to plastic deformation. At high pulse numbers two different additional degradation mechanisms are possible. First (at low temperature) the friction at crack edges can cause erosion. Second (at higher temperatures) high plastic deformation leads to isolated, protruding parts which can melt. Both, melt droplets and dust created by erosion, pose a great risk for a fusion reactor: for the operation due to possible plasma contamination and for safety, for example due to the problems connected with the removal of highly radioactive dust that entered the vacuum pumping systems.

The resistance of CFC against thermal loads is known to be greater than that of tungsten. It was shown that this is also valid for pulse numbers of up to 10^5. The temperatures during the tests where not high enough to introduce sufficient stresses to attain a degradation of the material. It is, however, notable that no long term fatigue mechanism was observed. Despite these findings the influence of neutrons in a reactor is expected to result in a loss of this superior resistance anyway [43]. Recent developments in the decisions for the ITER divertor indicate that CFC will not be used at all.

Regarding the use of tungsten as PFM in the ITER divertor the results show that a high number of transients is not tolerable even if they are mitigated to, for example, half the power density of natural type I ELMs. Either they have to be suppressed completely or the mitigation has to be very strong in order to avoid dust formation or melting. It should be noted that the damage threshold of 0.14 – 0.27 GWm^{-2} for 0.5 ms pulses only gives an upper limit. Although this threshold was valid for all tested base temperatures it is unconfirmed whether this holds true for higher temperatures, especially if they lead to extensive recrystallisation. Additionally, the grains of the material tested in this work were oriented parallel to the surface, meaning the material was comparatively strong in surface plane direction. The ITER reference material has grains oriented perpendicular to the surface to minimise the risk of parallel cracks that act as thermal barriers. It has already been shown that

a perpendicular grain orientation as well as recrystallised material have a lower damage threshold for low pulse numbers [51]. Finally, a decrease of this threshold should also be expected when including the influence of hydrogen (plasma) and neutrons.

Appendices

A FEM simulation script

```
FINISH
/CLEAR

/CONFIG,NRES,100000
/PLOPTS,MINM,0

/TITLE,Test
/PREP7

! all length data in mm

! width = x-direction
! height = y-direction (parallel to e-beam)
! depth = z-direction (tube direction, along the sample)

!_____________________________________________________________________________________________!
!_____________________________________Constants_____________________________________________!
!_____________________________________________________________________________________________!

! 1. Dimensions (in mm)

T_x = 12        !* tile width
T_y = 5         !*  "   height
T_z = 12        !*  "   depth

N_T = 3         !* number of tiles
R_T = 1         !* number of tiles "in a row" (on one "block")

G_z = 1         !* gap depth (gap between tiles)
S_z = 1         !* slit depth (slit between blocks)
S_y = 3.3       !* slit height

P_y = 0.8       !* pool height
D_x = 0.2       !* distance tile - pool border in x-direction
D_z = 0.2       !* distance tile - pool border in z-direction
D_ST = 3        !* distance slit - tube inner radius

B_x = 5         !* border in x-direction
B_z = 5         !* border in z-direction

T_oR = 6        !* cooling tube outer radius
T_iR = 4        !* cooling tube inner radius
CC_x = 10       !* cooling channel width (x-direction)
CC_y = 6        !* cooling channel hight (y-direction)
CC_d = 2        !* cooling channel wall thickness

T_p = 25        !* cooling tube protusion

W_r = 1         !* well radius

PApi_x = 10     !* PAN/pitch layers in one block
PAN_fr = 6      !* fraction of PAN layer (thickness)

R_CT = 0        !* Use rectangular cooling channel, 0 = off (tube)

!_____________________________________________________________________________________________!
! 2. Beam parameters

Hf0 = 273.142       !* heat flux at beam center [W/mm^2] (same as MW/m²)
            !* (HFF3(W): 136,712, HFF6(W): 273.142, HFF9(W): 405.574, HFF12(W): 549.16,
            !*  HFF9(CFC): 412.817, HFF12(CFC): 550.639, HFF15(CFC): 716.465)
sigma = 3.7171      !* Gauss beam sigma [mm]
            !* (HFF3(W): 5.2522, HFF6(W): 3.7171, HFF9(W): 2.9423, HFF12(W): 2.5288,
            !*  HFF9(CFC): 4.0183, HFF12(CFC): 3.4783 , HFF15(CFC): 2.9423)

x_0 = -T_x/2        !* x-coordinate of origin for beam spots from path file
z_0 = T_p+B_z+D_z   !* y-coordinate of origin for beam spots from path file

!_____________________________________________________________________________________________!
! 3. Mesh options
```

```
71
72  _DIV_x = 6      !* divisions in x-direction
73  _DIV_y = 5      !* divisions in y-direction
74  _DIV_z = 6      !* divisions in z-direction
75
76  _SIZE_x = 1     !* element size in x-direction, 0 = use _DIV_x
77  _SIZE_y = 1     !* element size in y-direction, 0 = use _DIV_y
78  _SIZE_z = 1     !* element size in z-direction, 0 = use _DIV_z
79
80  _BMF_x = 1      !* bias in x-direction, 0 = no bias
81  _BMF_y = 1      !* bias in y-direction, 0 = no bias
82  _BMF_z = 1      !* bias in z-direction, 0 = no bias
83
84  !-------------------------------------------------------------------------------------------!
85  ! 4. Solution & general options
86
87  Sym = 1         !* use symmetry (cut sample in z-direction in half), 0 = off
88  fir_T = 1       !* only create the first fir_T tile(s) (faster calc.), 0 = off
89  WC = 2          !* Water cooling method (1 = first, temp. independent, 2 = advanced, temp. dep.)
90  T_M = 35        !* Tile material (e. g. 35 = tungsten, 26 = CFC NB41, 33 = CFC NB31 (2D))
91  CB_M = 80       !* Cooling block material (80 = copper)
92
93  S_P = 0         !* calculate solution, 0 = off
94  S_T = 0         !* solution type, 0 = transient
95  S_HF = 10.0     !* static hf on face_1 [W/mm^2] (same as MW/m^2; for quick static calc.)
96  _IDLE = 3.952e-2    !* idle time in between ELM loads (for transient solution) [s]
97  N_idle = 1      !* number of time steps (divisions of cool down) for idle time (for
98              !* transient solution)
99  _P_T = 4.8e-4       !* time per point (for transient solution) [s]
100 N_Loads = 1     !* number of simultaniously loaded tiles (for transient solution)
101 N_Pts = 1       !* number of coordinates for transient load, will be multiplied by _REP
102             !* (for transient solution)
103 _REP = 1        !* number of repetitions of the N_Pts points to generate one transient
104             !* load (for transient solution)
105 Path_file = 'Path'  !* name of the file containing the coordinates; for simultaneous loads path
106             !* files have to have ascending numbers at the end (e.g. Path1, Path2, ...)
107             !* (for transient solution)
108 N_Cy = 1        !* number of transient/cool-down cycles (for transient solution)
109
110 *DIM,Hf1,,N_Loads
111 *DO,I,1,N_Loads
112     Hf1(I) = 0.0
113 *ENDDO
114 Hf1(1) = 0.0        !* steady state heat flux on face_1 (for additional entries add
115             !* Hf1(2) = ..., Hf1(3) = ..., ect.) [W/mm^2] (same as MW/m^2)
116
117 TREF,100        !* reference temperature [C]
118 TUNIF,100       !* initial temperature [C]
119
120 !-------------------------------------------------------------------------------------------!
121 !-----------------------------------Computed Values-----------------------------------------!
122 !-------------------------------------------------------------------------------------------!
123
124 *IF,T_M,EQ,33,THEN
125     CFC_2D = 1      !* simulate CFC with separate PAN and pitch blocks (different properties)
126 *ELSE
127     CFC_2D = 0
128 *ENDIF
129
130 *IF,MOD(N_T,R_T)/R_T,EQ,0,THEN      !* number of blocks
131     N_B = N_T/R_T
132 *ELSE
133     N_B = (N_T - MOD(N_T,R_T))/R_T + 1
134 *ENDIF
135
136 *IF,fir_T,GT,N_T,OR,fir_T,LE,0,THEN !* set fir_T to the number of tiles that actually will be created
137     fir_T = N_T
138 *ENDIF
139
140 *IF,MOD(fir_T,R_T)/R_T,EQ,0,THEN    !* number of "occupied" blocks
141     N_oB = fir_T/R_T
142 *ELSE
143     N_oB = (fir_T - MOD(fir_T,R_T))/R_T + 1
144 *ENDIF
145
146 Cy_t = _IDLE+N_Pts*_REP*_P_T        !* cycle time
147 T_l = R_T*T_z + (R_T-1)*G_z         !* tiles + gaps on one block
148 B_l = T_l+2*(D_z+B_z)               !* block length
149 C_x = T_x + 2*(D_x + B_x)           !* cooling element width
150 C_y = 2*(T_iR + S_y + D_ST)         !*    "       "    height
151 C_z = N_B*B_l + S_z*(N_B - 1)       !*    "       "    depth
152
153 *IF,Sym,NE,0,THEN
154     Sym = 1
155 *ENDIF
156
157 *IF,CC_x+2*CC_d+2,GT,C_x,OR,CC_y+2*CC_d+2,GT,C_y,THEN
158     *MSG,UI
159 Warning: Cooling channel too big. Process aborted.
160     *GO,:FIN
161 *ENDIF
162
163 *IF,2*T_oR+2,GT,C_x,OR,2*T_oR+2,GT,C_y,THEN
164     *MSG,UI
165 Warning: Cooling tube too big. Process aborted.
166     *GO,:FIN
167 *ENDIF
168
169 *IF,T_iR,GT,T_oR,THEN
170     *MSG,UI
171 Warning: Cooling tube inner radius greater than outer radius. Process aborted.
172     *GO,:FIN
173 *ENDIF
174
175 *IF,N_Loads,GT,N_T,THEN
176     *MSG,UI
177 Warning: Number of loaded surfaces exceeds number of existing surfaces. Process aborted.
178     *GO,:FIN
```

```
*ENDIF

*IF,_DIV_x,GT,4,AND,T_M,EQ,33,THEN
    *MSG,UI
Warning: Mesh size too small.
    *GO,:FIN
*ENDIF

!_____________________________________________________________________________________!
!_____________________________Elements & materials____________________________________!
!_____________________________________________________________________________________!

ET,1,87
ET,2,170
ET,3,174,2
ET,4,152,,,,1,1
ET,5,116,1,1
ET,6,90
ET,7,152,,,,,1
KEYOPT,4,8,3
KEYOPT,7,8,0
KEYOPT,7,9,1
TYPE

!**
!*********************************************************************
!**  CFC SNECMA NB41, Ref. No. 26
!*********************************************************************
!**
!** Pitch direction: Y
!** PAN direction: Z
!** Needling direction: X
!**

MPTEMP
MPTEMP, 1,   20,   200,  400,  600,  800,  1000
MPTEMP, 7, 1200
MPDATA,KXX, 26,  1,   0.0748, 0.0672, 0.0579,  0.049, 0.0438, 0.0394
MPDATA,KXX, 26,  7,   0.0337
MPDATA,KYY, 26,  1,    0.375,  0.317,  0.267,  0.223,  0.197,  0.172
MPDATA,KYY, 26,  7,    0.149
MPDATA,KZZ, 26,  1,   0.0995, 0.0927, 0.0797, 0.0645, 0.0592, 0.0542
MPDATA,KZZ, 26,  7,   0.047
!
MPDATA,C  , 26,  1,   628.78,1143.42,1487.84,1689.36,1807.27,1876.25
MPDATA,C  , 26,  7,  1916.62
!
MPTEMP
MPTEMP, 1,  200,   300,  400,  500,  600,  700
MPTEMP, 7,  800,   900
!
MPDATA,ALPX,26,  1,  1.91E-6,  1.94E-6,   2E-6,  2.15E-6,  2.29E-6,  2.41E-6
MPDATA,ALPX,26,  7,  2.56E-6,  2.82E-6
MPDATA,ALPY,26,  1, -0.35E-6, -0.18E-6,      0,  0.21E-6,  0.43E-6,  0.74E-6
MPDATA,ALPY,26,  7,  1.03E-6,  1.29E-6
MPDATA,ALPZ,26,  1,  0.68E-6,  0.71E-6,0.88E-6,     1E-6,  1.19E-6,  1.35E-6
MPDATA,ALPZ,26,  7,  1.66E-6,  1.88E-6
!
MPTEMP
MPTEMP,          1,      20
MPDATA,EX,26,    1,  0.094E5
MPDATA,EY,26,    1,  1.9E5
MPDATA,EZ,26,    1,  0.221E5
!
MP,NUXY,    26,        0.20
MP,NUXZ,    26,        0.20
MP,NUYZ,    26,        0.10
!
MP,DENS,    26,      1.96E-6


!**
!*********************************************************************
!**  CFC NB31 - pitch (Jeremie), Ref. No. 33
!*********************************************************************
!**
!**     Source: Jeremie
!**
!**                  Values at 3500 DgC are extrapolated
!** Pitch direction: Y
!** PAN direction: Z
!** Needling direction: X
!**

MPTEMP
MPTEMP,          1,       20,   100,   250,   500,   800,  1000
MPTEMP,          7,     1500,  3500
!
MPDATA,C  , 33,  1,      698,   909,  1244,  1587,  1817,  2000
MPDATA,C  , 33,  7,     2150,  2150
!
MPDATA,KXX, 33,  1,    0.1, 0.09, 0.08, 0.067, 0.06, 0.055
MPDATA,KXX, 33,  7,    0.05, 0.043
MPDATA,KYY, 33,  1,    0.447, 0.39, 0.33, 0.29, 0.27, 0.25
MPDATA,KYY, 33,  7,    0.223, 0.21
MPDATA,KZZ, 33,  1,    0.1, 0.09, 0.08, 0.067, 0.06, 0.055
MPDATA,KZZ, 33,  7,    0.05, 0.043
!
MPTEMP
MPTEMP,          1,     800,    1000,    1500
!
MPDATA,ALPX,33,  1,  2.1E-6,  2.7E-6,  3.4E-6
MPDATA,ALPY,33,  1,  0.347E-6,  0.446E-6,  0.562E-6
MPDATA,ALPZ,33,  1,  2.1E-6,  2.7E-6,  3.4E-6
!
MPTEMP
MPTEMP,          1,      20,    1000,    1500
!
```

```
MPDATA,EX,33,    1,  0.12E5,  0.12E5,  0.12E5
MPDATA,EY,33,    1,  1.73E5,  1.73E5,  1.73E5
MPDATA,EZ,33,    1,  0.12E5,  0.12E5,  0.12E5
!
MP,DENS,    33,      1.91E-6
!
MP,EMIS,    33,      0.9


!**
!*****************************************************************
!**  CFC NB31 - PAN (Jeremie), Ref. No. 34
!*****************************************************************
!**
!**     Source: Jeremie
!**
!**                    Values at 3500 DgC are extrapolated
!** Pitch direction: Y
!** PAN direction: Z
!** Needling direction: X
!**

MPTEMP
MPTEMP,          1,       20,   100,   250,   500,   800,  1000
MPTEMP,          7,     1500,  3500
!
MPDATA,C  , 34,  1,      698,   909,  1244,  1587,  1817,  2000
MPDATA,C  , 34,  7,     2150,  2150
!
MPDATA,KXX, 34,  1,    0.1, 0.09, 0.08, 0.067, 0.06, 0.055
MPDATA,KXX, 34,  7,    0.05, 0.043
MPDATA,KYY, 34,  1,    0.1, 0.09, 0.08, 0.067, 0.06, 0.055
MPDATA,KYY, 34,  7,    0.05, 0.043
MPDATA,KZZ, 34,  1,    0.172, 0.15, 0.13, 0.11, 0.1, 0.096
MPDATA,KZZ, 34,  7,    0.086, 0.08
!
MPTEMP
MPTEMP,          1,     800,    1000,    1500
MPDATA,ALPX,34,  1,  2.1E-6,  2.7E-6,  3.4E-6
MPDATA,ALPY,34,  1,  2.1E-6,  2.7E-6,  3.4E-6
MPDATA,ALPZ,34,  1,  0.263E-6,  0.338E-6,  0.426E-6
!
MPTEMP
MPTEMP,          1,      20,    1000,    1500
MPDATA,EX,34,    1,  0.12E5,  0.12E5,  0.12E5
MPDATA,EY,34,    1,  0.12E5,  0.12E5,  0.12E5
MPDATA,EZ,34,    1,  0.28E5,  0.28E5,  0.28E5
!
MP,DENS,    34,      1.91E-6
!
MP,EMIS,    34,      0.9


!**
!*****************************************************************
!**  PURE TUNGSTEN, Ref. No. 35
!*****************************************************************
!**

MPTEMP
MPTEMP, 1,   20,   50,  100,  200,  300,  400
MPTEMP, 7,  500,  600,  700,  800,  900, 1000
MPTEMP,13, 1100, 1200, 1300, 1400, 1500, 1600
MPTEMP,19, 1700, 1800, 1900, 2000, 2100, 2200
MPTEMP,25, 2300, 2400, 2500, 2600, 2700, 2800
MPTEMP,31, 2900, 3000
!
MPDATA,KXX,35,1,.16153,.15938,.15589,.14934,.14331,.13779,
MPDATA,KXX,35,7,.13274,.12814,.12396,.12017,.11676,.11370,
MPDATA,KXX,35,13,.11096,.10851,.10632,.10438,.10266,.10113,
MPDATA,KXX,35,19,.09977,.09854,.09743,.09640,.09544,.09451,
MPDATA,KXX,35,25,.09359,.09266,.09169,.09065,.08951,.08826,
MPDATA,KXX,35,31,.08687,.08530
!
MPDATA,C,35,1,131.45,132.12,133.21,135.32,137.36,139.36,
MPDATA,C,35,7,141.33,143.29,145.28,147.30,149.39,151.56,
MPDATA,C,35,13,153.84,156.25,158.80,161.53,164.46,167.61,
MPDATA,C,35,19,170.99,174.63,178.56,182.80,187.36,192.28,
MPDATA,C,35,25,197.56,203.25,209.34,215.88,222.88,230.36,
MPDATA,C,35,31,238.35,246.86
!
MPDATA,ALPX,35,1,4.22E-6,4.24E-6,4.28E-6,4.35E-6,4.42E-6,4.49E-6,
MPDATA,ALPX,35,7,4.56E-6,4.63E-6,4.70E-6,4.77E-6,4.84E-6,4.91E-6,
MPDATA,ALPX,35,13,4.98E-6,5.05E-6,5.12E-6,5.19E-6,5.26E-6,5.33E-6,
MPDATA,ALPX,35,19,5.39E-6,5.46E-6,5.53E-6,5.60E-6,5.67E-6,5.74E-6,
MPDATA,ALPX,35,25,5.81E-6,5.88E-6,5.95E-6
!
MPDATA,DENS,35,1,19.299E-6,19.298E-6,19.296E-6,19.292E-6,19.288E-6,19.284E-6,
MPDATA,DENS,35,7,19.280E-6,19.276E-6,19.272E-6,19.268E-6,19.265E-6,19.261E-6,
MPDATA,DENS,35,13,19.257E-6,19.253E-6,19.249E-6,19.245E-6,19.241E-6,19.237E-6,
MPDATA,DENS,35,19,19.234E-6,19.230E-6,19.226E-6,19.222E-6,19.218E-6,19.214E-6,
MPDATA,DENS,35,25,19.210E-6,19.206E-6,19.203E-6,19.199E-6,19.195E-6,19.191E-6,
MPDATA,DENS,35,31,19.187E-6,19.183E-6
!
MPDATA,EX,35,1,4.0791E5,4.0656E5,4.0431E5,3.9981E5,3.9531E5,3.9081E5,
MPDATA,EX,35,7,3.8631E5,3.8181E5,3.7731E5,3.7281E5,3.6831E5,3.6381E5,
MPDATA,EX,35,13,3.5931E5,3.5481E5,3.5031E5,3.4581E5,3.4131E5,3.3681E5
MPDATA,EX,35,19,3.3231E5,3.2781E5,3.2331E5,3.1881E5,3.1431E5,3.0981E5,
MPDATA,EX,35,25,3.0531E5,3.0081E5,2.9631E5,2.9181E5,2.8731E5,2.8281E5,
MPDATA,EX,35,31,2.7831E5,2.7381E5
!
MPDATA,NUXY,35,1,0.28,0.28,0.28,0.28,0.28,0.28,
MPDATA,NUXY,35,7,0.29,0.29,0.29,0.29,0.29,0.29,
MPDATA,NUXY,35,13,0.29,0.29,0.30,0.30,0.30,0.30,
MPDATA,NUXY,35,19,0.30,0.30,0.30,0.30,0.31,0.31,
MPDATA,NUXY,35,25,0.31,0.31,0.31,0.31,0.31,0.31,
MPDATA,NUXY,35,31,0.32,0.32

```

```
*IF,U_TE,NE,0,THEN
    MPDATA,EMIS,35,1,0.0104,0.0104,0.0104,0.0104,0.0104,0.0276
    MPDATA,EMIS,35,7,0.0443,0.0607,0.0767,0.0923,0.1075,0.1223
    MPDATA,EMIS,35,13,0.1367,0.1508,0.1644,0.1776,0.1905,0.2030
    MPDATA,EMIS,35,19,0.215,0.2267,0.238,0.2489,0.2594,0.2696
    MPDATA,EMIS,35,25,0.2793,0.2886,0.2976,0.3061,0.3143,0.3221
    MPDATA,EMIS,35,31,0.3295,0.3365
*ELSE
    MP,EMIS,35,Emi
*ENDIF


!**
!*****************************************************************
!**  OFHC COPPER, Ref. No. 80
!*****************************************************************
!**

MPTEMP
MPTEMP,          1,   27.,   327.,   527,  727,  927.
!
MPDATA,DENS, 80, 1, 8.88E-6, 8.78E-6, 8.68E-6, 8.59E-6, 8.46E-6
!
MPDATA, KXX, 80, 1,   0.398,   0.383,   0.371,   0.357,   0.342
!
MPDATA,   C, 80, 1,   386.0,   425.0,   447.0,   471.0,   492.0
!
MPTEMP
MPTEMP,          1,   20.,   100.,   200.,   400.,   500.,   600.
MPTEMP,          7,  800.
MPDATA,  EX, 80, 1, 84.0E+3, 80.0E+3, 75.0E+3, 70.0E+3, 67.0E+3, 63.0E+3
MPDATA,  EX, 80, 7, 60.0E+3
!
MP,    NUXY, 80,    0.33
!
MPTEMP
MPTEMP,      1,   20.0,   200.0,   400.0,   500.0,   600.0,  800.0
MPDATA,ALPX, 80, 1, 15.4E-6, 16.6E-6, 18.3E-6, 19.1E-6, 20.0E-6, 21.6E-6
!***
!***    Stress - strain curves at different temperatures
!***
!***    Data to be used in case of kinematic hardening
!***    bilinear curve: temperature, yield stress,
!***                    slope of the curve in the plastic region
!MPTEMP
!TB, BKIN, 80, 6
!TBTEMP, 100.      $ TBDATA, 1,  43, 1.47E+3
!TBTEMP, 200.      $ TBDATA, 1,  40, 1.47E+3
!TBTEMP, 400.      $ TBDATA, 1,  35, .835E+3
!TBTEMP, 500.      $ TBDATA, 1,  31, .556E+3
!TBTEMP, 600.      $ TBDATA, 1,  19, .227E+3
!TBTEMP, 800.      $ TBDATA, 1,  10, .151E+3
!***
!***    Data to be used in case of isotropic hardening
!***    (preferred option)
!***    multilinear curve: temperature, strain, stress, ...
!***    example: at 200 DgC at a total strain of 4%
!***             the stress is 98 MPa
!***
MPTEMP
TB, MISO, 80, 7
TBTEMP,  20. $TBPT,,5.357E-4, 45 $TBPT,,.04,105 $TBPT,,0.5,250
TBTEMP, 100. $TBPT,,5.375E-4, 43 $TBPT,,.04,101 $TBPT,,0.5,230
TBTEMP, 200. $TBPT,,5.333E-4, 40 $TBPT,,.04, 98 $TBPT,,0.5,200
TBTEMP, 400. $TBPT,,5.000E-4, 35 $TBPT,,.04, 68 $TBPT,,0.5, 90
TBTEMP, 500. $TBPT,,4.627E-4, 31 $TBPT,,.04, 53 $TBPT,,0.5, 60
TBTEMP, 600. $TBPT,,3.016E-4, 19 $TBPT,,.04, 28 $TBPT,,0.5, 30
TBTEMP, 800. $TBPT,,1.667E-4, 10 $TBPT,,.04, 16 $TBPT,,0.5, 20


!**
!**
!*****************************************************************
!**
!**          Heat transfer coefficients, water coolant
!**
!*****************************************************************
!**
!**                                                  Ref. No. 80
!**
!**  Diameter:             8 mm
!**  No twisted tape
!**  Pressure:             3 MPa
!**  Water temperature:  100 °C
!**  Velocity:            33 m/s
!**  Surface roughness:    5 micrometers
!**  Source: EUPITER Code
!**  Heat transfer coefficient vs. surface temperature
!**

MPTEMP
MPTEMP,       1,  100.00,  107.05,  114.01,  120.88,  127.67,  134.39
MPTEMP,       7,  141.06,  147.67,  154.24,  160.77,  167.26,  172.72
MPTEMP,      13,  180.15,  186.55,  192.94,  199.30,  205.64,  211.97
MPTEMP,      19,  218.29,  224.59,  230.88,  237.16,  243.44,  245.95
MPTEMP,      25,  252.22,  258.48,  264.74,  270.99,  277.25,  283.50
MPTEMP,      31,  289.76,  296.01,  302.26,  308.51,  314.77,  321.03
MPTEMP,      37,  327.29
MPDATA,HF,80,  1, 0.16114, 0.16239, 0.16362, 0.16477, 0.16582, 0.16681
MPDATA,HF,80,  7, 0.16773, 0.16858, 0.16938, 0.17013, 0.17084, 0.17149
MPDATA,HF,80, 13, 0.17211, 0.17269, 0.17324, 0.17375, 0.17423, 0.17469
MPDATA,HF,80, 19, 0.17511, 0.17552, 0.17589, 0.17625, 0.17658, 0.17671
MPDATA,HF,80, 25, 0.17709, 0.17770, 0.17870, 0.18026, 0.18253, 0.18566
MPDATA,HF,80, 31, 0.18977, 0.19494, 0.20121, 0.20863, 0.21718, 0.22683
MPDATA,HF,80, 37, 0.23755


*GET,matmax,MAT,,NUM,MAX
```

```
MP,KXX,matmax+1,0.67937e-3
MP,DENS,matmax+1,0.95971e-6
MP,VISC,matmax+1,0.0002825e-6
MP,C,matmax+1,4210

!_____________________________________Gauss shape_____________________________________!
!____________________________________________________________________________________!

*DO,I,1,N_Loads
    _FNCNAME = STRCOMP(STRCAT('Gauss2D',CHRVAL(I)))
    *DIM,%_FNCNAME%_TABLE,7,20,1,,,0
    ! Begin of equation: Hf0*exp(-(((X)-x_0)^2+((Z)-z_0)^2)/2/sigma^2)+Hf1
    *SET,%_FNCNAME%(0,0,1), 0.0, -999
    *SET,%_FNCNAME%(2,0,1), 0.0
    *SET,%_FNCNAME%(3,0,1), Hf0
    *SET,%_FNCNAME%(4,0,1), x_0
    *SET,%_FNCNAME%(5,0,1), z_0
    *SET,%_FNCNAME%(6,0,1), sigma
    *SET,%_FNCNAME%(7,0,1), Hf1(I)
    *SET,%_FNCNAME%(0,1,1), 1.0, -1, 0, 0, 0, 0
    *SET,%_FNCNAME%(0,2,1), 0.0, -2, 0, 1, 0, 0, -1
    *SET,%_FNCNAME%(0,3,1), 0.0, -3, 0, 1, -1, 2, -2
    *SET,%_FNCNAME%(0,4,1), 0.0, -1, 0, 1, 2, 2, 18
    *SET,%_FNCNAME%(0,5,1), 0.0, -2, 0, 2, 0, 0, -1
    *SET,%_FNCNAME%(0,6,1), 0.0, -4, 0, 1, -1, 17, -2
    *SET,%_FNCNAME%(0,7,1), 0.0, -1, 0, 1, 4, 2, 19
    *SET,%_FNCNAME%(0,8,1), 0.0, -2, 0, 2, 0, 0, -1
    *SET,%_FNCNAME%(0,9,1), 0.0, -5, 0, 1, -1, 17, -2
    *SET,%_FNCNAME%(0,10,1), 0.0, -1, 0, 1, -4, 1, -5
    *SET,%_FNCNAME%(0,11,1), 0.0, -2, 0, 1, -3, 3, -1
    *SET,%_FNCNAME%(0,12,1), 0.0, -1, 0, 2, 0, 0, -2
    *SET,%_FNCNAME%(0,13,1), 0.0, -3, 0, 1, -2, 4, -1
    *SET,%_FNCNAME%(0,14,1), 0.0, -1, 0, 2, 0, 0, 20
    *SET,%_FNCNAME%(0,15,1), 0.0, -2, 0, 1, 20, 17, -1
    *SET,%_FNCNAME%(0,16,1), 0.0, -1, 0, 1, -3, 4, -2
    *SET,%_FNCNAME%(0,17,1), 0.0, -1, 7, 1, -1, 0, 0
    *SET,%_FNCNAME%(0,18,1), 0.0, -2, 0, 1, 17, 3, -1
    *SET,%_FNCNAME%(0,19,1), 0.0, -1, 0, 1, -2, 1, 21
    *SET,%_FNCNAME%(0,20,1), 0.0, 99, 0, 1, -1, 0, 0
    ! End of equation: Hf0*exp(-(((X)-x_0)^2+((Z)-z_0)^2)/2/sigma^2)+Hf1
*ENDDO

!_____________________________________Beam spots_____________________________________!
!____________________________________________________________________________________!

*DO,I,N_Loads,1,-1
    _ARRNAME = STRCOMP(STRCAT('Gauss_pts',CHRVAL(I)))
    *DIM,%_ARRNAME%,,N_Pts,2,x_G,y_G,0
    str = STRCOMP(STRCAT(Path_file,CHRVAL(I)))
    *VREAD,%_ARRNAME%,%str%,csv,,jik,2,N_pts
(2F6.3)
    *DO,J,1,N_Pts
        %_ARRNAME%(J,1) = %_ARRNAME%(J,1) + x_0
        %_ARRNAME%(J,2) = %_ARRNAME%(J,2) + z_0
    *ENDDO
*ENDDO

!#####################################################################################
!format: (n_f_s_k_)
!n_: number of columns
!f_: f for float, i for integer etc.
!s_: overall number of digits
!k_: number of decimal places
!example: |    305.23      45.12345     76.12351
!format: (f11.2f14.5)
!#####################################################################################

!_____________________________________Cooling block_____________________________________!
!_______________________________________________________________________________________!

/VIEW,1,0.5,0.5,0.5

!_______________________________________________________________________________________!

/PNUM,DEFA
/PNUM,VOLUME,1
/NUMBER,2

!_______________________________________Cooling block_____________________________________!
!_______________________________________________________________________________________!

BLOCK,-C_x/2,C_x/2,-C_y/2,C_y/2,T_p,C_z+T_p !* create cooling block

*IF,N_B,GT,1,THEN
    *DO,I,1,N_B-1                   !* create slit(s) between blocks
        BLOCK,-C_x/2,C_x/2,C_y/2-S_y,C_y/2,I*B_l+T_p+(I-1)*S_z,I*B_l+T_p+I*S_z
    *ENDDO
*ENDIF

*IF,P_y,GT,0,THEN
    *DO,I,0,N_B-1                   !* create pool(s)
        BL_Z1 = (I+1)*B_z+I*(B_l-B_z+S_z)+T_p
        BL_Z2 = (I+1)*(B_z+T_l+2*D_z)+I*(B_z+S_z)+T_p
        BLOCK,-(T_x/2+D_x),T_x/2+D_x,C_y/2-P_y,C_y/2,BL_Z1,BL_Z2
    *ENDDO
*ENDIF

WPROTA,0,90,0
*DO,I,0,N_B-1
    *DO,J,0,1
        *DO,K,0,1                   !* create rounded edges of pool(s)
            WPAVE,(-1)**K*(T_x+D_x)/2,C_y/2,(I+1)*B_z+I*(B_l-B_z+S_z)+T_p+J*(T_l+2*D_z)
            CYL4,0,0,W_r,,,,P_y
        *ENDDO
    *ENDDO
*ENDDO

*DO,I,N_B-1,0,-1                    !* melt the rounded edges with the pool
    VADD,N_B+I+1,2+N_B+I+4+1,2+N_B+I+4+2,2+N_B+I+4+3,2+N_B+I+4+4
```

```
    *ENDDO

    *DO,I,0,N_B-1                           !* melt the areas of rounded edges and pool
        ASEL,,LOC,Y,T_iR+D_ST+S_y-P_y
        ASEL,R,LOC,Z,(I+1)*B_z+I*(S_z+B_l-B_z)+T_p-W_r,(I+1)*B_z+I*(S_z+B_l-B_z)+T_p+T_l+2*D_z+W_r
        AADD,ALL
        ALLSEL
    *ENDDO
    NUMCMP,VOLU
    NUMCMP,AREA
    WPROTA,0,-90,0
    WPAVE,0
    WPSTYL,,,,,,,,0
*ENDIF

*IF,R_CT,EQ,0,THEN                          !* create the cooling channel hole volume
    CYL4,0,0,T_oR,,,,T_p+C_z
*ELSE
    BLOCK,-CC_x/2-CC_d,CC_x/2+CC_d,-CC_y/2-CC_d,CC_y/2+CC_d,0,T_p+C_z
*ENDIF

*GET,Max_V,VOLU,,NUM,MAXD
VSEL,,VOLU,,2,Max_V,1
CM,Substract,VOLU
ALLSEL
VSBV,1,Substract,,DELETE,KEEP               !* substract slit(s), pool(s) and pipe hole from block
CMDELE,Substract
VDELE,2,Max_V,1,1
NUMCMP,VOLU
NUMCMP,AREA

*IF,R_CT,EQ,0,THEN                          !* create cooling channel wall
    CYL4,0,0,T_oR,,T_iR,,2*T_p+C_z
*ELSE
    BLOCK,-CC_x/2-CC_d,CC_x/2+CC_d,-CC_y/2-CC_d,CC_y/2+CC_d,0,2*T_p+C_z
    BLOCK,-CC_x/2,CC_x/2,-CC_y/2,CC_y/2,0,2*T_p+C_z
    VSBV,2,3,,DELETE,DELETE
*ENDIF

VADD,ALL                                    !* merge cooling pipe and block
NUMCMP,VOLU
NUMCMP,AREA

*IF,Sym,NE,0,THEN                           !* cut in half if symmetry option is on
    BLOCK,0,C_x/2,-C_y/2,C_y/2,0,C_z+2*T_p
    VSBV,1,2,,DELETE,DELETE
    NUMCMP,VOLU
    NUMCMP,AREA
*ENDIF

VATT,CB_M,-1,1,-1                           !* assign material number
SMRTSIZE,6
VMESH,1


TYPE,2
ASEL,,LOC,Y,C_y/2-P_y

ASEL,R,LOC,Z,T_p,T_p+N_oB*B_l+(N_B-1)*S_z

NSLA,,1
ESLN,,0
ESURF                                       !* create contact surface(s) on cooling block
ALLSEL

!_____________________________________________________________________________________________!
!_____________________________Water cooling___________________________________________________!
!_____________________________________________________________________________________________!

*IF,R_CT,NE,0,THEN
    ASEL,,LOC,Y,-CC_y/2,CC_y/2
    ASEL,R,LOC,X,-CC_x/2,CC_x/2
    ASEL,R,LOC,Z,T_p+C_z/2
*ELSE
    ASEL,,LOC,Y,-T_iR,T_iR
    ASEL,R,LOC,X,-T_iR,T_iR
    ASEL,R,LOC,Z,T_p+C_z/2
*ENDIF
NSLA,,1
CM,surf_152,NODE
ALLSEL

CMSEL,,surf_152
*GET,nnum,node,,count
SELTOL,0.75
*DOWHILE,nnum                   !* until nnum <= 0
    nn_ = ndnext(0)             !* get next node in selected set
    N,,0,0,nz(nn_)              !* create node at center of tube with z-coordinate of node nn
    NSEL,U,LOC,Z,nz(nn_)        !* unselect all nodes with the same z-coordinate
    *GET,nnum,node,,count       !* update nnum (currently selected nodes)
*ENDDO
SELTOL
ALLSEL
NSLE,U
R,2,2*T_iR,T_iR**2*ACOS(-1)
REAL,2
TYPE,5
MAT,matmax+1
*GET,nnum,node,,count
n1 = node(0,0,0)
*DO,I,1,nnum-1
    nsel,u,,,n1
    nn = node(nx(n1),ny(n1),nz(n1))
    nsel,a,,,n1
    e,n1,nn
    nsel,u,,,n1
    n1 = nn
*ENDDO
ESEL,,TYPE,,5
```

```
CM,elem_116,ELEM
ALLSEL

R,3
REAL,3
TYPE,4
NDSURF,'surf_152','elem_116',3
ALLSEL

ESEL,,TYPE,,4
*IF,WC,EQ,1,THEN
   SFE,ALL,,CONV,0,0.14   !* (in W/(mm^2))
*ELSEIF,WC,EQ,2
   SFE,ALL,,CONV,0,-1*CB_M
*ELSE
   S_P = 0
   *MSG,UI
   Warning: No valid water cooling enabled! Solution aborted.
*ENDIF
ALLSEL
ESEL,,TYPE,,5
SFE,ALL,,HFLUX,,1.66666667
ALLSEL
D,node(0,0,0),TEMP,100

/PNUM,VOLU,0
/PNUM,MAT,1
/NUMBER,1

x_1 = -T_x/2
x_2 = x_1 + T_x
y_1 = C_y/2 - P_y
y_2 = y_1 + T_y
z_1 = T_p + D_z + B_z
z_2 = z_1 + T_z

SMRTSIZE,OFF
R,1,,,,,,,
RMORE,,,,,,
RMORE,,10000
REAL,1
TYPE,3

*IF,CFC_2D,NE,0,THEN
   *IF,Sym,NE,0,THEN
      J_MAX = PApi_x/2-1+0.5*MOD(PApi_x,2)
   *ELSE
      J_MAX = PApi_x-1
   *ENDIF
   K_MAX = 1
*ELSE
   J_MAX = 0
   K_MAX = 0
   PApi_x = 1
*ENDIF

T_n = 1
*DO,I,0,fir_T-1
   B_n = (I-MOD(I,R_T))/R_T
   z_1 = T_p + D_z + B_z + MOD(I,R_T)*(T_z+G_z) + B_n*(B_l+S_z)
   z_2 = z_1 + T_z
   *DO,J,0,J_MAX
      *DO,K,0,K_MAX
         *IF,CFC_2D,NE,0,THEN                    !* 2D tiles (symmetric and non-symmetric case)
            x_1 = -T_x/2+J*T_x/PApi_x*K*1/PAN_fr*T_x/PApi_x
            x_2 = x_1+(1/PAN_fr+K*(1-2/PAN_fr))*T_x/PApi_x
            *IF,K,EQ,K_MAX,AND,J,EQ,J_MAX,THEN
               x_2 = 0
            *ENDIF
         *ELSEIF,Sym,NE,0                        !* bulk tiles (symmetric case)
            x_2 = x_1 + T_x/2
         *ENDIF

         BLOCK,x_1,x_2,y_1,y_2,z_1,z_2
         T_n = T_n+1                             !* serial number of current tile

         VSEL,,,,T_n

         VATT,T_M+K_MAX-K,-1,6,-1                !* assign material number

         ASLV
         LSLA
         LSEL,R,TAN2,X,1
         LESIZE,ALL,_SIZE_x,,_DIV_x,1/_BMF_x,1,,,0  !* line sizing in x-direction

         VSEL,,,,T_n
         ASLV
         LSLA
         LSEL,R,TAN2,X,-1
         LESIZE,ALL,_SIZE_x,,_DIV_x,_BMF_x,1,,,0    !* line sizing in x-direction

         VSEL,,,,T_n
         ASLV
         LSLA
         LSEL,R,TAN2,Y,1
         LESIZE,ALL,_SIZE_y,,_DIV_y,1/_BMF_y,1,,,0  !* line sizing in y-direction

         VSEL,,,,T_n
         ASLV
         LSLA
         LSEL,R,TAN2,Y,-1
         LESIZE,ALL,_SIZE_y,,_DIV_y,_BMF_y,1,,,0    !* line sizing in y-direction

         VSEL,,,,T_n
```

```
            ASLV
            LSLA
            LSEL,R,LOC,Z,(z_1+z_2)/2
            LESIZE,ALL,_SIZE_z,,_DIV_z,_BMF_z,1,,,0     !* line sizing in z-direction

            ALLSEL
            VMESH,T_n                                   !* mesh volume

            VSEL,,,,T_n
            ASLV
            ASEL,R,LOC,Y,y_1
            NSLA,,1
            ESLN
            TYPE,3
            ESURF                                       !* contact surface (bottom)

            *IF,CFC_2D,NE,0,AND,J+K,LT,J_MAX+K_MAX,THEN !* contact surface (between layers)
                VSEL,,,,T_n
                ASLV
                ASEL,R,LOC,X,x_2
                NSLA,,1
                ESLN
                TYPE,3
                ESURF
            *ENDIF
            *IF,CFC_2D,NE,0,AND,J+K,NE,0,THEN           !* contact surface (between layers)
                VSEL,,,,T_n
                ASLV
                ASEL,R,LOC,X,x_1
                NSLA,,1
                ESLN
                TYPE,2
                ESURF
            *ENDIF
        *ENDDO
    *ENDDO
    VSEL,,,,T_n-CFC_2D*((2-Sym)*PApi_x-1),T_n
    ASLV
    ASEL,R,LOC,Y,y_2
    NSLA,,1
    name = STRCOMP(STRCAT('face_',CHRVAL(I+1)))
    CM,%name%,NODE
    NSEL,R,,,NODE(0,y_2,(z_1+z_2)/2)
    name = STRCOMP(STRCAT('centre_',CHRVAL(I+1)))
    CM,%name%,NODE
*ENDDO

ALLSEL
CNCHECK,AUTO

!__________________________________________________________________________________________________!
!__________________________________________Solution________________________________________________!
!__________________________________________________________________________________________________!

*IF,_STATUS,GT,1,THEN
    S_P = 0
    *MSG,UI
Warnigs and/or errors detected. Solution aborted.
*ENDIF

*IF,S_P,NE,0,THEN
    *ASK,S_P,Start solving? (Type 0 for no),S_P
*ENDIF

*IF,S_P,NE,0,THEN
    /SOLU
    SOLCONTROL,ON

    *IF,S_T,NE,0,THEN
        ANTYPE,STATIC
        AUTOTS,ON
        SF,face_1,HFLUX,S_HF
        SOLVE
        SFDELE,face_1,HFLUX
    *ELSE
        ANTYPE,TRANS
        TIMINT,ON
        AUTOTS,ON
        KBC,1
        NSUBST,1,2,1
        OUTRES,ERASE
        OUTRES,BASIC,ALL
        OUTRES,RSOL,NONE
        OUTRES,ESOL,NONE

        *DO,I,0,N_Cy-1
            *DO,J,1,N_Pts*_REP+N_idle
                *DO,K,1,N_Loads
                    _FNCNAME = STRCOMP(STRCAT('Gauss2D',CHRVAL(K)))
                    _ARRNAME = STRCOMP(STRCAT('Gauss_pts',CHRVAL(K)))
                    _FACE = STRCOMP(STRCAT('face_',CHRVAL(K)))
                    *IF,J,LE,N_Pts*_REP,THEN
                        *SET,%_FNCNAME%(4,0,1),%_ARRNAME%(1+MOD((J-1),N_Pts),1)
                        *SET,%_FNCNAME%(5,0,1),%_ARRNAME%(1+MOD((J-1),N_Pts),2)
                        SFDELE,_FACE,HFLUX
                        _FNCNAME = STRCAT('%',_FNCNAME)
                        _FNCNAME = STRCAT(_FNCNAME,'%')
                        SF,_FACE,HFLUX,_FNCNAME
                        TIME,I*Cy_t+J*_P_T
                    *ELSEIF,J,EQ,N_Pts*_REP+1
                        SFDELE,_FACE,HFLUX
                        *IF,Hf1(K),GT,0,THEN
                            SF,_FACE,HFLUX,Hf1(K)
                        *ENDIF
                        TIME,I*Cy_t+N_Pts*_REP*_P_T+(J-N_Pts*_REP)*_IDLE/N_idle
                    *ELSE
                        TIME,I*Cy_t+N_Pts*_REP*_P_T+(J-N_Pts*_REP)*_IDLE/N_idle
                    *ENDIF
```

```
      *ENDDO
      SOLVE
    *ENDDO
  *ENDDO
*ENDIF
*ENDIF
/GFORMAT,F,,0

:FIN
FINISH
```

B Final mock up design dimensions

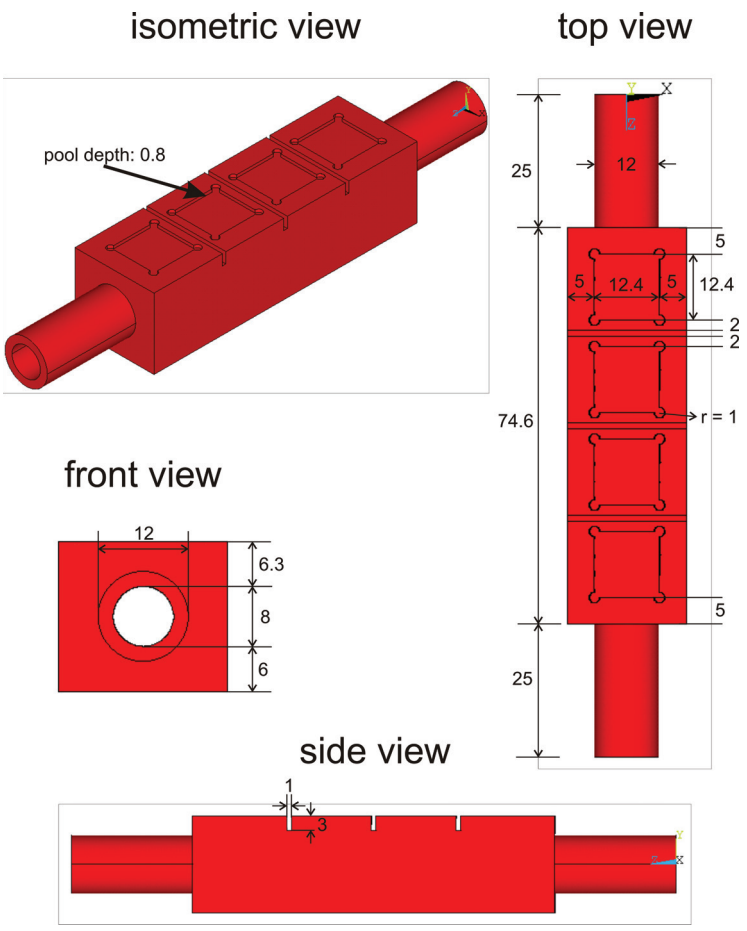

Figure B.1: Schematic drawing of the final mock up geometry. All dimensions are given in millimetres.

C Beam profile measurement results

The results of the beam profile measurements performed with the method described in section 3.5 are listed hereafter. A tungsten wire of 1.6 mm thickness was used during all measurements with acceleration voltage of 50 kV; during 40 kV tests a 0.5 mm thick tungsten wire was used. However, tests with different thicknesses ≤ 1.6 mm did not show significant differences in results. The pressure in the cathode chamber and in the intermediate chamber were kept constant at $p_{cathode} = 4.2 \cdot 10^{-6}$ mbar and $p_{intermediate} = 2.7 \cdot 10^{-5}$ mbar respectively. Magnetic lens current for lens 1 was always at 100 %, as this showed good results with respect to strong focussing (also in [1]) and to reduce parameter space. The measured signal was analysed with the Origin software (Gauss fits). Measurements were repeated at least ten times and an average FWHM was calculated as well as the standard deviation (called Δ_{FWHM} here). The resulting incident power density is also given.

C.1 Results for $p_{chamber} = 3.5 \cdot 10^{-4}$ mbar

Table C.1: Beam measurement results for P = **38 kW** machine power at U_a = **50 kV** and a main chamber pressure of $p_{chamber} = 3.5 \cdot 10^{-4}$ mbar.

L2 (%)	FWHM (mm)	Δ_{FWHM} (mm)	L (MWm^{-2})	ΔL (MWm^{-2})
35	5.21	0.30	1236	144
36	5.03	0.32	1324	167
37	5.37	0.37	1163	162
38	5.42	0.28	1142	119
39	5.45	0.30	1130	123
40	5.57	0.28	1079	109
41	5.86	0.28	978	92
42	5.99	0.18	933	55
43	6.52	0.16	789	40
44	7.09	0.33	668	62

Table C.2: Beam measurement results for P = **40 kW** machine power at U_a = **50 kV** and a main chamber pressure of $p_{chamber} = 3.5 \cdot 10^{-4}$ mbar.

L2 (%)	FWHM (mm)	Δ_{FWHM} (mm)	L (MWm^{-2})	ΔL (MWm^{-2})
36	5.35	0.28	1233	128
37	5.54	0.42	1152	176
38	5.61	0.13	1123	52
39	5.67	0.22	1099	84
40	5.81	0.13	1045	46
41	6.16	0.36	930	109
42	6.61	0.35	808	87

Table C.3: Beam measurement results for P = **43 kW** machine power at U_a = **50 kV** and a main chamber pressure of $p_{chamber} = 3.5 \cdot 10^{-4}$ mbar.

L2 (%)	FWHM (mm)	Δ_{FWHM} (mm)	L (MWm^{-2})	ΔL (MWm^{-2})
33	5.73	0.30	1156	120
34	5.69	0.22	1172	92
35	5.68	0.46	1175	189
36	5.94	0.20	1076	73
37	5.85	0.29	1110	109
38	5.95	0.29	1071	105
39	6.23	0.25	977	78
40	6.52	0.33	893	90
41	6.55	0.26	886	71
42	7.24	0.24	725	48
43	7.72	0.16	636	26
44	8.26	0.40	556	53

Table C.4: Beam measurement results for P = **43 kW** machine power at U_a = **40 kV** and a main chamber pressure of $p_{chamber} = 3.5 \cdot 10^{-4}$ mbar.

L2 (%)	FWHM (mm)	Δ_{FWHM} (mm)	L (MWm^{-2})	ΔL (MWm^{-2})
23	7.39	0.34	694	63
24	7.86	0.40	614	63
25	7.66	0.46	647	78
26	7.55	0.26	666	45
27	7.69	0.18	641	30
28	7.71	0.20	638	33
29	7.43	0.28	688	52
30	7.41	0.28	691	53
31	7.49	0.35	677	63
32	7.64	0.11	651	19
33	7.88	0.17	611	27
34	8.36	0.18	542	24
35	9.05	0.33	463	34
36	9.74	0.38	400	31
37	10.52	0.27	343	18
38	11.11	0.26	308	14
39	11.60	0.33	282	16
40	11.88	0.24	269	11
41	12.21	0.39	255	16

C.2 Results for $\mathbf{p_{chamber}} = 2.1 \cdot 10^{-4}$ mbar

Table C.5: Beam measurement results for P = **38 kW** machine power at U_a = **50 kV** and a main chamber pressure of $p_{chamber} = 2.1 \cdot 10^{-4}$ mbar.

L2 (%)	FWHM (mm)	Δ_{FWHM} (mm)	L (MWm^{-2})	ΔL (MWm^{-2})
35	4.58	0.16	1596	108
36	4.60	0.10	1587	69
37	4.66	0.17	1546	113
38	4.71	0.21	1510	136
39	4.85	0.14	1428	83
40	5.02	0.37	1333	195
41	5.05	0.14	1313	75
42	5.35	0.14	1172	62
43	5.76	0.26	1012	92
44	6.89	0.50	707	104

Table C.6: Beam measurement results for P = **40 kW** machine power at U_a = **50 kV** and a main chamber pressure of $p_{chamber} = 2.1 \cdot 10^{-4}$ mbar.

L2 (%)	FWHM (mm)	Δ_{FWHM} (mm)	L (MWm^{-2})	ΔL (MWm^{-2})
36	5.27	0.51	1273	245
37	5.03	0.17	1395	94
38	4.98	0.17	1421	94
39	5.11	0.12	1354	64
40	5.40	0.28	1212	125
41	5.68	0.23	1093	88
42	6.18	0.31	925	94
43	6.99	0.34	722	71
44	7.99	0.51	553	71

Table C.7: Beam measurement results for P = **43 kW** machine power at U_a = **50 kV** and a main chamber pressure of $p_{chamber} = 2.1 \cdot 10^{-4}$ mbar.

L2 (%)	FWHM (mm)	Δ_{FWHM} (mm)	L (MWm^{-2})	ΔL (MWm^{-2})
34	5.08	0.09	1472	55
35	5.06	0.25	1484	147
36	5.17	0.26	1420	144
37	5.32	0.24	1341	119
38	5.35	0.11	1324	53
39	5.58	0.16	1217	70
40	6.09	0.30	1024	102
41	6.49	0.39	900	108
42	7.23	0.30	727	60

C.3 Results for $\mathbf{p_{chamber}} = 1.3 \cdot 10^{-4}$ mbar

Table C.8: Beam measurement results for P = **38 kW** machine power at U_a = **50 kV** and a main chamber pressure of $p_{chamber} = 1.3 \cdot 10^{-4}$ mbar.

L2 (%)	FWHM (mm)	Δ_{FWHM} (mm)	L (MWm^{-2})	ΔL (MWm^{-2})
35	6.95	0.62	694	124
36	5.97	0.61	942	193
37	5.27	0.60	1207	276
38	4.85	0.49	1424	289
39	4.78	0.57	1470	349
40	4.24	0.62	1863	542
41	4.35	0.81	1772	660
42	4.72	0.33	1507	208
43	5.60	0.21	1071	79
44	6.78	0.62	731	133

Table C.9: Beam measurement results for P = **40 kW** machine power at U_a = **50 kV** and a main chamber pressure of $p_{chamber} = 1.3 \cdot 10^{-4}$ mbar.

L2 (%)	FWHM (mm)	Δ_{FWHM} (mm)	L (MWm^{-2})	ΔL (MWm^{-2})
36	5.48	0.41	1177	177
37	5.05	0.67	1387	369
38	4.60	0.79	1668	571
39	4.27	0.53	1940	479
40	4.39	0.48	1829	404
41	5.30	0.43	1255	201
42	6.10	0.21	948	65

Table C.10: Beam measurement results for P = **43 kW** machine power at U_a = **50 kV** and a main chamber pressure of $p_{chamber} = 1.3 \cdot 10^{-4}$ mbar.

L2 (%)	FWHM (mm)	Δ_{FWHM} (mm)	L (MWm^{-2})	ΔL (MWm^{-2})
34	6.43	0.38	918	109
35	5.39	0.53	1304	257
36	4.30	0.46	2051	435
37	3.93	0.53	2459	669
38	3.71	0.11	2756	162
39	4.96	0.48	1540	301
40	6.00	0.39	1055	138
41	6.96	0.56	782	126
42	7.85	0.47	616	75

Bibliography

[1] S. Keusemann; Feasibility study for the simulation of transient thermal events on plasma facing materials with electron beams; Master's thesis RWTH Aachen (2008) (cited on pages: VI, 14, 17, 24, 26, 28, 37, 38, 50, and 93)

[2] M. P. Fewell; The atomic nuclide with the highest mean binding energy; *American Journal of Physics* 63 (7) 653–658 (1995); doi: 10.1119/1.17828; http://ajp.aapt.org/resource/1/ajpias/v63/i7/p653_s1 (cited on page: 1)

[3] G. R. Caughlan, W. A. Fowler; Thermonuclear reaction rates V; *Atomic Data and Nuclear Data Tables* 40 (2) 283–334 (1988) (cited on page: 2)

[4] F. Ajzenberg-Selove; Energy levels of light nuclei A = 5-10; *Nuclear Physics A* 490 (1) 1–225 (1988) (cited on page: 3)

[5] ITER Organisation (2009); http://www.iter.org (cited on pages: 3, 4, and 5)

[6] EFDA-JET (2009); http://www.jet.efda.org (cited on pages: 3 and 4)

[7] M. Keilhacker, A. Gibson et al.; High fusion performance from deuterium-tritium plasmas in JET; *Nuclear Fusion* 39 (2) 209–234 (1999); doi: 10.1088/0029-5515/39/2/306; http://iopscience.iop.org/0029-5515/39/2/306/ (cited on page: 4)

[8] J. Ongena, G. van Oost; Energy for future centuries; *Fusion Science and Technology* 53 (2T) 3–15 (2008); http://www.carolusmagnus.net/papers/2007/docs/IN1_Ongena_paper.pdf (cited on page: 4)

[9] V. Barabash; Role and contribution of ITER in research of materials and reactor components; *Journal of Nuclear Materials* 329–333, Part A 156–160 (2004); doi: 10.1016/j.jnucmat.2004.04.015; http://www.sciencedirect.com/science/article/pii/S0022311504001461 (cited on pages: 4, 8, and 9)

[10] Y. Shimomura; ITER and plasma surface interaction issues in a fusion reactor; *Journal of Nuclear Materials* 363–365 467–475 (2007); doi: 10.1016/j.jnucmat.2007.01.215; http://www.sciencedirect.com/science/article/pii/S002231150700092X (cited on page: 4)

[11] J. Linke, T. Hirai et al.; Performance of Plasma-Facing Materials under Intense Thermal Loads in Tokamaks and Stellarators; *Fusion Science and Technology* 46 142–151 (2004); http://juwel.fz-juelich.de:8080/dspace/bitstream/2128/2788/1/54707.pdf (cited on pages: 4 and 9)

[12] G. Federici; Plasma wall interactions in ITER; *Physica Scripta* T124 1–8 (2006); doi: 10.1088/0031-8949/2006/T124/001; http://iopscience.iop.org/1402-4896/2006/T124/001/ (cited on pages: 4 and 9)

[13] J. W. Davis et al.; ITER Material Properties Handbook (1997) (cited on pages: 4 and 18)

[14] J. P. Bonal, D. Moulinier; Thermal properties of advanced carbon fiber composites for fusion application; Commis. Energ. At., Paris (1995) (cited on page: 4)

[15] V. Barabash, M. Akiba et al.; Carbon fiber composites application in ITER plasma facing components; *Journal of Nuclear Materials* 258–263 (Part 1) 149–159 (1998); ISSN 0022-3115; doi: 10.1016/S0022-3115(98)00267-0; http://www.sciencedirect.com/science/article/B6TXN-45JC0B6-J/2/e4322ebc147b20c8bd741db60e5beea5 (cited on pages: 4 and 6)

[16] E. Lassner, W.-D. Schubert; Tungsten: Properties, Chemistry, Technology of the Element, Alloys, and Chemical Compounds; Kluwer Academic / Plenum Plublishers, New York (1999); ISBN 978-0-306-45053-2 (cited on pages: 4, 65, 66, 71, and 75)

[17] L. A. Singheiser, T. Hirai et al.; Plasma-facing materials for thermo-nuclear fusion devices; *Transactions of The Indian Institute of Metals* 62 (2) 123–128 (April 2009); doi: 10.1007/s12666-009-0016-y; http://www.springerlink.com/content/0810514777q5p0n6/ (cited on pages: 4, 5, and 9)

[18] T. Pütterich, R. Neu et al.; Calculation and experimental test of the cooling factor of tungsten; *Nuclear Fusion* 50 025012 (2010); doi: 10.1088/0029-5515/50/2/025012; http://iopscience.iop.org/0029-5515/50/2/025012/ (cited on page: 5)

[19] V. Philipps; Tungsten as material for plasma-facing components in fusion devices; *Journal of Nuclear Materials* 415 (1, Supplement) 2–9 (2011); doi: 10.1016/j.jnucmat.2011.01.110; http://www.sciencedirect.com/science/article/pii/S002231151100158; Proceedings of the 19th International Conference on Plasma-Surface Interactions in Controlled Fusion (cited on page: 5)

[20] R. Behrisch, G. Federici et al.; Material erosion at the vessel walls of future fusion devices; *Journal of Nuclear Materials* 313–316 388–392 (2003);

doi: 10.1016/S0022-3115(02)01580-5; http://www.sciencedirect.com/science/article/pii/S0022311502015805 (cited on pages: 5 and 73)

[21] ITER Material Assessment Report; G 74 MA 10 01-07-11 W 2.2 (2001) (cited on page: 6)

[22] G. Janeschitz, L. Boccaccini et al.; Development of fusion technology for DEMO in Forschungszentrum Karlsruhe; *Fusion Engineering and Design* 81 (23–24) 2661–2671 (2006); ISSN 0920-3796; doi: 10.1016/j.fusengdes.2006.07.085; http://www.sciencedirect.com/science/article/pii/S092037960600250X (cited on page: 6)

[23] V. Barabash, G. Federici et al.; Neutron irradiation effects on plasma facing materials; *Journal of Nuclear Materials* 283–287 138–146 (2000); doi: 10.1016/S0022-3115(00)00203-8; http://www.sciencedirect.com/science/article/pii/S0022311500002038 (cited on page: 6)

[24] M. R. Gilbert, J. Sublet; Neutron-induced transmutation effects in W and W-alloys in a fusion environment; *Nuclear Fusion* 51 043005 (2011); doi: 10.1088/0029-5515/51/4/043005; http://iopscience.iop.org/0029-5515/51/4/043005/ (cited on page: 6)

[25] J. Roth, E. Tsitrone et al.; Recent analysis of key plasma wall interactions issues for ITER; *Journal of Nuclear Materials* 390–391 1–9 (2009); doi: 10.1016/j.jnucmat.2009.01.037; http://www.sciencedirect.com/science/article/pii/S0022311509000506; Proceedings of the 18th International Conference on Plasma-Surface Interactions in Controlled Fusion Device (cited on page: 6)

[26] T. Tanabe; Tritium issues to be solved for establishment of a fusion reactor; *Fusion Engineering and Design* (2012); doi: 10.1016/j.fusengdes.2012.02.009; http://www.sciencedirect.com/science/article/pii/S0920379612000646 (cited on page: 6)

[27] J. Paméla, G. F. Matthews et al.; An ITER-like wall for JET; *Journal of Nuclear Materials* 363–365 1–11 (2007); doi: 10.1016/j.jnucmat.2006.12.056; http://www.sciencedirect.com/science/article/pii/S0022311506006283 (cited on page: 7)

[28] F. Romanelli, M. Laxåback et al.; Overview of JET results; *Nuclear Fusion* 51 (9) 094008 (2011); doi: 10.1088/0029-5515/51/9/094008; http://iopscience.iop.org/0029-5515/51/9/094008/ (cited on page: 7)

[29] H. Bolt, V. Barabash et al.; Plasma facing and high heat flux materials - needs for ITER and beyond; *Journal of Nuclear Materials* 307–311 43–52 (2002);

doi: 10.1016/S0022-3115(02)01175-3; http://www.sciencedirect.com/science/article/pii/S0022311502011753 (cited on page: 8)

[30] A. Loarte, G. Saibene et al.; Characteristics of type I ELM energy and particle losses in existing devices and their extrapolation to ITER; *Plasma Physics and Controlled Fusion* 45 1549–1569 (2003); doi: 10.1088/0741-3335/45/9/302; http://iopscience.iop.org/0741-3335/45/9/302/ (cited on pages: 8 and 9)

[31] J. Linke; High heat flux performance of plasma facing components under service conditions in future fusion reactors; *Transactions of Fusion Science and Technology* 49 (2T) 455–464 (2006); http://www.carolusmagnus.net/papers/2005/docs/linke_plasma_facing_materials.pdf (cited on pages: 8 and 9)

[32] M. Merola, D. Loesser et al.; ITER plasma-facing components; *Fusion Engineering and Design* 85 (10-12) 2312–2322 (December 2010); ISSN 0920-3796; doi: 10.1016/j.fusengdes.2010.09.013; http://www.sciencedirect.com/science/article/B6V3C-518F0BP-1/2/69a00c70cdbbf2662f8c8b4ecf7a5734 (cited on pages: 8, 9, and 47)

[33] R. A. Pitts, S. Carpentier et al.; Physics basis and design of the ITER plasma-facing components; *Journal of Nuclear Materials* 415 (1, Supplement) 957–964 (2011); ISSN 0022-3115; doi: 10.1016/j.jnucmat.2011.01.114; http://www.sciencedirect.com/science/article/pii/S0022311511001620 (cited on pages: 8, 9, and 24)

[34] E. J. Doyle, R. J. Groebner et al.; Modifications in turbulence and edge electric fields at the L–H transition in the DIII-D tokamak; *Physics of Fluids B* 3 (8) 2300–2307 (1991); doi: 10.1063/1.859597; http://link.aip.org/link/doi/10.1063/1.859597 (cited on page: 8)

[35] A. W. Leonard, A. Herrmann et al.; The impact of ELMs on the ITER divertor; *Journal of Nuclear Materials* 266–269 109–117 (1999); doi: 10.1016/S0022-3115(98)00522-4; http://www.sciencedirect.com/science/article/pii/S0022311598005224 (cited on page: 8)

[36] A. W. Leonard, T. H. Osborne et al.; Tolerable ELMs at high density in DIII-D; *Journal of Nuclear Materials* 290–293 1097–1101 (2001); doi: 10.1016/S0022-3115(00)00503-1; http://www.sciencedirect.com/science/article/pii/S0022311500005031 (cited on page: 8)

[37] S. Clement, A. Chankin et al.; Power deposition in the JET divertor during ELMs; *Journal of Nuclear Materials* 266–269 285–290 (1999); doi: 10.1016/S0022-3115(98)00530-3; http://www.sciencedirect.com/science/article/pii/S0022311598005303 (cited on page: 8)

[38] A. Loarte, G. Saibene et al.; ELM energy and particle losses and their extrapolation to burning plasma experiments; *Journal of Nuclear Materials* 313–316 962–966 (2003); doi: 10.1016/S0022-3115(02)01398-3; http://www.sciencedirect.com/science/article/pii/S0022311502013983 (cited on page: 8)

[39] M. E. Fenstermacher, T. E. Evans et al.; Effect of island overlap on edge localized mode suppression by resonant magnetic perturbations in DIII-D; *Physics of Plasmas* 15 056122 (2008); doi: 10.1063/1.2901064; http://pop.aip.org/resource/1/phpaen/v15/i5/p056122_s1 (cited on pages: 9 and 13)

[40] J. Linke, F. Escourbiac et al.; High heat flux testing of plasma facing materials and components – Status and perspectives for ITER related activities; *Journal of Nuclear Materials* 367–370 1422–1431 (2007); doi: 10.1016/j.jnucmat.2007.04.028; http://www.sciencedirect.com/science/article/pii/S0022311507006174 (cited on pages: 9 and 73)

[41] B. N. Bazylev, Y. Koza et al.; Energy Threshold of Brittle Destruction for Carbon-Based Materials; *Physica Scripta* T111 213–217 (2004); doi: 10.1238/Physica.Topical.111a00213; http://iopscience.iop.org/1402-4896/2004/T111/036 (cited on page: 11)

[42] G. Federici, A. Zhitlukhin et al.; Effects of ELMs and disruptions on ITER divertor armour materials; *Journal of Nuclear Materials* 337–339 684–690 (2005); doi: 10.1016/j.jnucmat.2004.10.149; http://www.sciencedirect.com/science/article/pii/S0022311504009353 (cited on page: 11)

[43] M. Rödig, W. Kühnlein et al.; Post irradiation testing of samples from the irradiation experiments PARIDE 3 and PARIDE 4; *Journal of Nuclear Materials* 329–333 766–770 (2004); doi: 10.1016/j.jnucmat.2004.04.176; http://www.sciencedirect.com/science/article/pii/S0022311504003162 (cited on pages: 13 and 76)

[44] P. Garin, M. Sugimoto; Main baseline of IFMIF/EVEDA project; *Fusion Engineering and Design* 84 259–264 (2009); doi: 10.1016/j.fusengdes.2008.12.040; http://www.sciencedirect.com/science/article/pii/S092037960800495X; Proceeding of the 25th Symposium on Fusion Technology (SOFT-25) (cited on page: 13)

[45] M. Becoulet, G. Huysmans et al.; Edge localized modes control: experiment and theory; *Journal of Nuclear Materials* 337–339 677–683 (2005); doi: 10.1016/j.jnucmat.2004.09.074; http://www.sciencedirect.com/science/article/pii/S0022311504009705 (cited on page: 13)

[46] T. E. Evans, M. E. Fenstermacher et al.; RMP ELM suppression in DIII-D plasmas with ITER similar shapes and collisionalities; *Nucl. Fusion*

48 024002 (2008); doi: 10.1088/0029-5515/48/2/024002; http://iopscience.iop.org/0029-5515/48/2/024002/pdf/0029-5515_48_2_024002.pdf (cited on page: 13)

[47] M. von Ardenne; Tabellen zur angewandten Physik volume 1; Deutscher Verlag der Wissenschaften 2nd edition (1973) (cited on page: 15)

[48] S. Schiller, U. Heisig et al.; Elektronenstrahltechnologie; Wissenschaftliche Verlagsgesellschaft Stuttgart, Lizenz des Verlag Technik, VEB Berlin (1977); ISBN 9783804705333 (cited on page: 15)

[49] E. Wessel; private communication (2009) (cited on pages: 15 and 47)

[50] S. Flügge; Handbuch der Physik, Band XXI; Springer-Verlag (1956) (cited on page: 15)

[51] M. Wirtz; Thermal shock behaviour of different tungsten grades under varying preconditions; Ph.D. thesis RWTH Aachen (2012) (cited on pages: 15, 68, and 77)

[52] R. Duwe, W. Kühnlein et al.; The new electron beam facility for materials testing in hot cells - design and preliminary experience; *Fusion Technology* p. 355 (1995) (cited on page: 15)

[53] A. Schmidt, A. Bürger et al.; High Heat Flux Testing of components for future fusion devices by means of the facility JUDITH 2; In International Conference on High-Power Electron Beam Technology 2010 (EBEAM 2010) volume 1 p. 571. Curran Associates, Inc. (April 2011); ISBN 9781617823992; Proceedings of a meeting held 24-26 October 2010, Reno, Nevada, USA (cited on page: 17)

[54] P. Majerus, R. Duwe et al.; The new electron beam test facility JUDITH II for high heat flux experiments on plasma facing components; *Fusion Engineering and Design* 75–79 365–369 (2005); doi: 10.1016/j.fusengdes.2005.06.058; http://www.sciencedirect.com/science/article/pii/S0920379605001602 (cited on pages: 17 and 37)

[55] A. Schmidt, T. Hirai et al.; First demonstration of non-destructive tests on tungsten-coated JET divertor CFC tiles in the electron beam facility JUDITH-2; *Physica Scripta* T138 014034 (2009) (cited on pages: 17, 24, and 41)

[56] Z. M. Zhang, B. K. Tsai et al.; Experimental Methods in the Physical Sciences – Radiometric Temperature Measurements: I. Fundamentals; Elsevier Inc. (2010); ISBN 9780123740212 (cited on page: 18)

[57] ITER Material Assessment Report; G 74 MA 10 01-07-11 W 0.2 (2001) (cited on pages: 21, 71, and 75)

[58] G. Ritz; Performance of tungsten-based materials and components under ITER and DEMO relevant steady-state thermal loads; Ph.D. thesis RWTH Aachen (2011); ISBN 9783893367559; http://darwin.bth.rwth-aachen.de/opus/volltexte/2011/3658/ (cited on pages: 22, 50, and 70)

[59] G. Pintsuk, W. Kühnlein et al.; Investigation of tungsten and beryllium behaviour under short transient events; *Fusion Engineering and Design* 82 (15—24) 1720–1729 (2007); ISSN 0920-3796; doi: 10.1016/j.fusengdes.2007.06.030; http://www.sciencedirect.com/science/article/pii/S0920379607003341; Proceedings of the 24th Symposium on Fusion Technology (SOFT-24) (cited on pages: 34 and 70)

[60] T. Hirai, G. Pintsuk; Thermo-mechanical calculations on operation temperature limits of tungsten as plasma facing material; *Fusion Engineering and Design* 82 389–393 (2007); doi: 10.1016/j.fusengdes.2007.03.032; http://www.sciencedirect.com/science/article/pii/S0920379607001287 (cited on page: 34)

[61] A. Schmidt; private communication (2011) (cited on page: 41)

[62] G. Pintsuk, A. Prokhodtseva et al.; Thermal shock characterization of tungsten deformed in two orthogonal directions; *Journal of Nuclear Materials* 417 481–486 (2011); doi: 10.1016/j.jnucmat.2010.12.109; http://www.sciencedirect.com/science/article/pii/S0022311510009311 (cited on pages: 46, 60, 61, and 67)

[63] P. Morgan; Carbon fibers and their composites; CRC Press (2005); ISBN 9780824709839 (cited on page: 47)

[64] J. Linke, S. Amouroux et al.; Brittle destruction of carbon-based materials in transient heat load tests; *Fusion Engineering and Design* 66–68 395–399 (2003); doi: 10.1016/S0920-3796(03)00164-9; http://www.sciencedirect.com/science/article/pii/S0920379603001649 (cited on page: 47)

[65] G. Pintsuk, J. Compan et al.; Mechanical and thermo-physical characterization of the carbon fibre composite NB31; *Physica Scripta* T128 66–71 (2007); doi: 10.1088/0031-8949/2007/T128/013; http://iopscience.iop.org/1402-4896/2007/T128/013 (cited on page: 47)

[66] J. Compan; Analysis of carbon based materials under fusion relevant thermo-mechanical loads; Ph.D. thesis RWTH Aachen (2009); http://darwin.bth.rwth-aachen.de/opus/volltexte/2009/2670/ (cited on pages: 47 and 50)

[67] J. Compan, T. Hirai et al.; Microstructural and thermo-mechanical characterization of carbon/carbon composites; *Journal of Nuclear Materials* 386–388

797–800 (2009); doi: 10.1016/j.jnucmat.2008.12.222; http://www.sciencedirect.com/science/article/pii/S0022311508009872 (cited on page: 47)

[68] M. Merola, V. Barabash et al.; ITER plasma facing component materials database in ANSYS format; *ITER doc. G 17 MD 71 96-11-19 W 0.1* Version 1.3 (2000) (cited on page: 50)

[69] G. Pintsuk, J. Compan et al.; Measurement of thermo-physical and mechanical properties of CFC delivered by SNECMA; Technical report Forschungszentrum Jülich GmbH (2008) (cited on page: 50)

[70] M. Merola, G. Vieider et al.; EUPITER: the European thermohydraulic package for plasma facing components; In Proceedings of the Specialists' Workshop on High Heat Flux Cooling for ITER PFCs. JET Culham (UK) (September 23-25 1996) (cited on page: 50)

[71] S. Schider; Refractory Metals: Powder Metallurgical Materials for High Tech Usage; verlag moderne industrie AG & Co. (1991) (cited on page: 71)

[72] Plansse Group homepage (2012); http://www.plansee.com (cited on page: 71)

[73] N. Klimov, V. Podkovyrov et al.; Experimental study of PFCs erosion and eroded material deposition under ITER-like transient loads at the plasma gun facility QSPA-T; *Journal of Nuclear Materials* 415 (1, Supplement) 59–64 (2011); doi: 10.1016/j.jnucmat.2011.01.013; http://www.sciencedirect.com/science/article/pii/S0022311511000250; Proceedings of the 19th International Conference on Plasma-Surface Interactions in Controlled Fusion (cited on page: 73)

[74] M. Wirtz, J. Linke et al.; Comparison of the thermal shock performance of different tungsten grades and the influence of microstructure on the damage behaviour; *Physica Scripta* T145 014058 (2011); doi: 10.1088/0031-8949/2011/T145/014058; http://iopscience.iop.org/1402-4896/2011/T145/014058/ (cited on page: 76)

Danksagung

Als Erstem möchte ich Prof. Dr. L. Singheiser danken, der mich schon bei meinem Vorstellungstermin sehr herzlich begrüßte und mir die Möglichkeit gegeben hat an seinem Institut zu promovieren. Sein Engagement für seine Mitarbeiter und seine Freundlichkeit sind für mich vorbildlich.

Prof. Dr. D. Bosbach hat sich bereit erklärt das Korreferat zu übernehmen. Dafür danke ich ihm sehr herzlich und hoffe der Einblick in die Fusionsforschung hat ihm gefallen.

Dr. J. Linke danke ich für die Aufnahme in seine Arbeitsgruppe. Durch sein immenses Wissen um die gesamte Fusionsthematik, seine kreativen Ideen und seine ansteckende Begeisterung hat er mich hervorragend betreut. Seine ungezwungene und offene Art trägt außerdem zum Wichtigsten bei, was eine Arbeitsstelle bieten soll: eine angenehme Arbeitsatmosphäre.

Den Postdocs unserer Gruppe danke ich für ihre Unterstützung und Betreuung: ganz besonders Dr. G. Pintsuk, der einen mit pragmatischen Ansätzen voranbringt und seine langjährige Erfahrung, insbesondere mit Wolfram, stets zur Verfügung stellt; Dr. C. Thomser und Dr. J. Du, deren ungewöhnliche Sichtweisen für neue Impulse sorgen.

G. Knauf und G. Böling danke ich für ihre Hilfe bei allen technischen Fragen, sowie bei der Planung und Fertigung von Proben.

Dem gesamten Team des HML möchte ich für die Unterstützung bei der Durchführung der Experimente danken, insbesondere: Dr. M. Rödig und Dr. A. Schmidt für die wissenschaftliche Betreuung, A. Bürger für die Hilfe bei der praktischen Umsetzung, K. Dominiczak und M. Lowis für die Durchführung an JUDITH 2.

Mein Dank gilt ebenso den Mitarbeitern im IEK-2, im Besonderen: Dr. E. Wessel für seine Hilfe bei den REM und EBSD Aufnahmen, V. Gutzeit und J. Bartsch für die Betreuung in der Materialografie, M. Felden für prompte Poster- und sonstige Drucke, sowie exzellente Fotografien der Testkomponenten, und P. Joecken für seine

Hilfe bei Netzwerk- und Computerproblemen aller Art.

Ich möchte auch Th. Koppitz dafür danken, dass er seine Erfahrung und sein Wissen bezüglich des Lötens der Komponenten mit mir geteilt hat und das Löten derselben stets zügig und sehr zuverlässig durchführte.

Meinen Kollegen und Freunden C. Asensio Jiménez, G. Ritz und M. Wirtz danke ich für die tolle Arbeitsatmosphäre im Büro und die schönen Zeiten bei Treffen nach der Arbeit. Außerdem gebührt mein Dank auch all meinen Freunden außerhalb des Forschungszentrums und meiner Familie, die Menschen die mich immer unterstützen.

Band / Volume 160
Ice Crystal Measurements with the New Particle Spectrometer NIXE-CAPS
J. Meyer (2013), ii, 132 pp
ISBN: 978-3-89336-840-2

Band / Volume 161
Thermal Shock Behaviour of Different Tungsten Grades under Varying Conditions
O. M. Wirtz (2013), XIV, 130 pp
ISBN: 978-3-89336-842-6

Band / Volume 162
Effects of ^{137}Cs and ^{90}Sr on structure and functional aspects of the microflora in agricultural used soils
B. Niedrée (2013), XII, 92 pp
ISBN: 978-3-89336-843-3

Band / Volume 163
Lidar observations of natural and volcanic-ash-induced cirrus clouds
C. Rolf (2013), IX, 124 pp
ISBN: 978-3-89336-847-1

Band / Volume 164
CO2-Abscheidung, -Speicherung und -Nutzung:
Technische, wirtschaftliche, umweltseitige und gesellschaftliche Perspektive
Advances in Systems Analysis 2
W. Kuckshinrichs; J.-F. Hake (Eds.) (2012), iv, 354 pp
ISBN: 978-3-89336-850-1

Band / Volume 165
Interest Mediation and Policy Formulation in the European Union
Influence of Transnational Technology-Oriented Agreements on European Policy in the Field of Carbon Capture and Storage
Advances in Systems Analysis 3
O. Schenk (2013), XIII, 253 pp
ISBN: 978-3-89336-852-5

Band / Volume 166
Versagensverhalten plasmagespritzter Mg-Al-Spinell-Schichten unter Thermozyklierung
S. M. Ebert (2013), X, 173 pp
ISBN: 978-3-89336-853-2

Band / Volume 167
Coupled modeling of water, vapor and heat in unsaturated soils - Field applications and numerical studies
C. Steenpaß (2013), X, 123 pp
ISBN: 978-3-89336-854-9

Band / Volume 168
An analysis of the global atmospheric methane budget under different climates
A. Basu (2013), v, 110 pp
ISBN: 978-3-89336-859-4

Band / Volume 169
Experimental determination of the partitioning coefficient of nopinone as a marker substance in organic aerosol
B. Steitz (2013), 132 pp
ISBN: 978-3-89336-862-4

Band / Volume 170
Ion Beam Treatment of Functional Layers in Thin-Film Silicon Solar Cells
W. Zhang (2013), xi, 191 pp
ISBN: 978-3-89336-864-8

Band / Volume 171
Pulvermetallurgische Herstellung von porösem Titan und von NiTi-Legierungen für biomedizinische Anwendungen
M. Bram (2013), X, 238 pp
ISBN: 978-3-89336-866-2

Band / Volume 172
IEK-3 Report 2013. Langlebige Elektrochemische Verfahrenstechnik
(2013), ca. 185 pp
ISBN: 978-3-89336-868-6

Band / Volume 173
Combined Steady State and High Cycle Transient Heat Load Simulation with the Electron Beam Facility JUDITH 2
Th. Loewenhoff (2013), XVI, 108 pp
ISBN: 978-3-89336-869-3

Energie & Umwelt / Energy & Environment
Band / Volume 173
ISBN 978-3-89336-869-3

JÜLICH
FORSCHUNGSZENTRUM